New Technologies for Mechanism Elucidation and High Throughput Screening of Endosome Disruption by Carriers Designed for Intracellular Biologic Drug Delivery

By

Kameron V. Kilchrist

Dissertation

Submitted to the Faculty of the

Graduate School of Vanderbilt University

in partial fulfillment of the requirements

for the degree of

DOCTOR OF PHILOSOPHY

in

Biomedical Engineering

August 9, 2019

Nashville, Tennessee

Approved:
Craig L. Duvall, Ph.D.
Colleen M. Brophy, M.D.
W. David Merryman, Ph.D.
Cynthia Reinhart-King, Ph.D.
John T. Wilson, Ph.D.

For patients awaiting smarter medicines

ACKNOWLEDGEMENTS

I gratefully acknowledge funding—especially my funding from the National Science Foundation Graduate Research Fellowship. Specific acknowledgements of all funding and scientific consultation are mentioned in the acknowledgements for each chapter

I am thankful to all of the friends, mentors, and advisors I have had over the years, who have nurtured my interest in science and math and allowed it to flourish. From teachers in high school who went far beyond their duties: Mr. Dwayne Edwards, Mr. Robert DeMay, Ms. Michelle Landry, and others; personal and professional mentors in college: Ms. Melissa Crawford, Dr. Zakiya Wilson, Dr. Isiah Warner, Dr. Daniel Hayes, Dr. Marybeth Lima, Dr. Todd Monroe, Dr. Boldor, and Dr. Les Butler. I am also thankful to Lorraine Fei, Nick Mai, Tony Tzeng, Daniel Comeaux, Dr. Bruce Parker, Tucker Barry, Les Cruse, Ritu Roy, and many others who played important roles in shaping me. I am also particularly thankful to Brooke Morris, whose chance dinner conversation led me to change my major from computer to biological engineering, triggering a cascade of events which led to this dissertation.

I am thankful for several internal and external scientific collaborations. Dr. Colleen Brophy and Dr. Joyce Cheung-Flynn, collaborating with you improves our work immensely. Dr. Nick Mignemi, thank you for the opportunity to work on an interesting computational project entirely unrelated to this dissertation. Dr. Ashwath Jayagopal and Roche pRED and NORD, thank you for the opportunity to work in an industry setting on such an interesting project within such a dynamic group.

I am constantly thankful for my advisor, Dr. Craig Duvall, for his support and mentorship, and for the lab he has assembled—10 years of the ATL! The lab's collective impact on my

scientific training cannot be understated, and I owe them enormous gratitude. To those I met as graduate students (Dr. Chris Nelson, Dr. Brian Evans, Dr. Kristin O'Grady, Dr. Kelsey Mayo, Dr. John Martin, Martina Miteva, Dr. Samantha Sarett, Dr. Thomas Werfel, Dr. Meredith Jackson, Taylor Kavanaugh, Sean Bedingfield, Bryan Dollinger, Isom Kelly, Prarthana Patil, Ella Hoogenboezem, Brock Fletcher, Shrusti Patel, Carli DeJulius, and William Tierney) and those I met as postdocs and scientists of the group (Dr. Mukesh Gupta, Dr. Kellye Kirkbride, Dr. Fang Yu, and Dr. Eric Dailing): I am glad to have worked alongside you and look forward to watching your careers progress. I am particularly thankful to Dr. Brian Evans and Dr. Eric Dailing for close scientific collaborations and to Sean Bedingfield for perspective shifting conversations. I am also grateful to Somtochukwu Dimobi, whose contributions were invaluable to Aim 2 and whose perspective is wise beyond her years.

Finally, I thank my parents, siblings, Robert Toups III, Tyler DiStefano, Steven Adair, Blake Brockway, Chris Hawk, Josh Upchurch, and Todd Walker. Explaining why would exceed the length of this document, and they know why anyway.

TABLE OF CONTENTS

Page

LIST OF TABLES

LIST OF FIGURES

Figure **Page**

CHAPTER 1

INTRODUCTION

Since the first FDA approval of a recombinant protein drug, insulin, in 1982,[1] pharma companies have turned to biologic molecules for therapies. No longer was the search for medicines like panning for gold in a riverbed, testing thousands of compounds at random in hopes of success, but rather more akin to alchemy—turning the very building blocks of life into medicines.

Biologic drugs are bioactive proteins, peptides, nucleic acids, and/or polysaccharides that have therapeutic uses.[2] These drugs have revolutionized many fields of medicine and make up a substantial fraction of pre-clinical drug development activity today. These medicines are attractive because their discovery and development process is straightforward compared to small molecules, although there are unique challenges in their production scale-up.[3] With eight notable exceptions, all biomacromolecular molecule drugs in clinical use are proteins or peptides that act outside the cell—either to inhibit or mimic receptor-agonist or receptor-antagonist interactions, as in antibodies and receptor decoy proteins, or to replace or supplement a naturally occurring signaling molecule or enzyme found in the blood. Because biologic drugs are highly water soluble, they are unable to diffuse across the lipid bilayer membranes of cells in the same way that small molecules do. Because of these delivery barriers, the clinical application of intracellular-acting biologics has been limited.

Throughout this dissertation, I focus on studying two critical barriers that impede the development of intracellular-acting biologic drugs: first, endocytosis: entry of biologics into the cell, and second, endosomal escape: the process by which drug carriers disrupt endosomal

membranes to deliver biologic drugs to the cell cytosol. These are universal barriers that the development of intracellular large molecule biologic drugs face.

1.1 Specific Aims

Aim 1: Elucidate the mechanism of enhanced cellular uptake and cytosolic retention of MK2 inhibitory peptide nano-polyplexes (MK2i-NP)

A lack of mechanistic understanding of nanoscale drug carrier interactions with cellular mechanisms of endocytosis impedes generalized drug carrier development. Using a promising preclinical nanoscale drug carrier formulation, MK2i-NP, I measure nanoparticle uptake under the influence of selective inhibitors of endocytosis to elucidate the endocytic pathways by which MK2i-NPs enter cells. Studies with scanning electron microscopy investigate polymer-induced changes to the external plasma membrane, while transmission electron microscopy studies reveal the extent and timing of cellular uptake and endosomal disruption. Finally, a novel assay based on Galectin-8 YFP is presented, which allows the real-time kinetic monitoring of endosomal disruption in live cells with confocal microscopy. These studies provide novel mechanistic insights into MK2i-NP interaction with cell and endosomal membranes, which we show triggers macropinocytosis. Finally, Gal8-YFP assays reveal unexpectedly rapid endosomal disruption within 30 minutes of MK2i-NP application to cells.

Aim 2: Validate Gal8 visualization of endosome disruption as predictive of carrier-mediated biologic drug intracellular bioavailability

Despite the centrality of endosomal escape to drug carrier development for intracellular biologic delivery, few drug carrier development efforts directly measure endosomal disruption

because these assays are cumbersome and prone to artefacts. Using the Gal8-YFP system introduced in Aim 1 and a family of PEG-b-(DMAEMA-co-BMA) polymers previously known to be endosome disrupting, we examine measurements of endosomal disruption by several techniques, including lysotracker colocalization and transmission electron microscopy, and correlate these measures to cytosolic siRNA delivery and bioactivity as measured by knockdown of the model gene firefly luciferase. We show Gal8-YFP recruitment to be the assay with the highest correlation to siRNA delivery of those studied, and further uncover that increased 50B molecular weight increases endosomal disruption and intracellular siRNA delivery. Finally, we show that Gal8-YFP tracking can be used *in vivo* to assess endosomal disruption in an orthotopic breast cancer model.

Aim 3: Develop novel high throughput endosome disruption reporter assays

Despite advances made towards a high throughput assay to assess endosomal disruption in Aim 2, the Gal8-YFP assay has two significant limitations. One, it requires long imaging times on a high throughput microscope (1-2 hours), and two, deployment *in vivo* is limited due the inherent difficulties of high resolution intravital microscopy, leading to unacceptable data variance, even within the same tumor. Using split firefly luciferase as a system to measure transient protein-protein interactions, I develop two new genetically encoded split luciferase assay systems to measure endosomal disruption in live cells, reducing the time to image one plate from 1-2 hours to a single 60 second, whole-plate luminescent reading. I provide insights into key parameters in the generation of these stable cell lines by generating ten different cell lines and conduct a sensitivity analysis of transfection efficiency on the ultimate luminescence response. Finally, I compare these assays to Gal8-YFP recruitment and show that they detect

endosomal disruption for even lower doses of endosome disrupting polymer and propose they may circumvent *in vivo* limitations of Gal8-YFP.

The remainder of this introduction will explain several paradigms in drug development and provide context for two important topics. First, I present a short overview of a generalized drug discovery process. Next, I briefly introduce several classes of biologic drugs with a focus on intracellular mechanisms of action. I then discuss all eight US FDA approved biologic drugs with intracellular mechanisms of action, and attempt to assess commonalities between them to guide future thinking into biologic drug development. Finally, I provide a short insight into the two drug delivery polymers I use as tool compounds in this dissertation to study cellular processes of endocytosis and endosomal disruption and to develop new assays to measure these processes.

This dissertation seeks to address: (1) an inadequate mechanistic understanding of the physicochemical parameters that drive intracellular, nanoscale drug delivery, and (2) inadequate assays to assess the rate limiting step of intracellular drug delivery: endosomal disruption. In Chapter 2, I present a mechanistic understanding of one promising drug carrier developed by our group, and uncover a novel technology to assess the kinetics of endosomal disruption by using temporal tracking of Galectin8-YFP. In Chapter 3, I extend and validate this measurement technique as an endpoint assay with the paired use of automated confocal microscopy and automated image analysis, providing robust and rapid measurement of endosomal disruption across tens of thousands of cells in a couple hours, and, in the process, uncover new structure-function relationships between drug carrier polymer molecular weight and intracellular endosomal disruption. Finally, in Chapter 4, I develop two new genetically encoded split firefly luciferase systems to measure intracellular protein-protein interactions as a proxy for endosomal

disruption in live cells even more quickly. Finally, in Chapter 5, I present a summary of this work and discuss its anticipated impact.

1.2 The Drug Discovery and Development Process

The discovery and development process of each drug is unique, with many drugs being discovered through serendipity.[4] However, many other drugs are discovered through a rather standardized process.[5,6] First, a biological 'target' is identified—a particular protein, cellular process, or phenotype is identified or hypothesized to be associated with disease.[7] Notably, a target need not be validated as causative in human disease; this level of validation is only achieved upon FDA approval of a medicine with this mechanism of action. Next, one or more high throughput screening assays are developed which seek to recapitulate this phenomenon as cleanly as possible in an *in vitro* assay in multi-well plates, which may take the form of biochemical or cell-based assays. These assays are of tantamount importance—and have several constraints. First, they must fit into the existing physical and operational structure for a given drug discovery group (*e.g.*, plates must be compatible with liquid handling robots, the assay must be compatible with atmospheric, temperature, and solvent constraints, *inter al*.). Second, they must be robust, reproducible, and have a large signal separation between positive and negative control samples. Third, they must be scalable and automatable.

Once a high throughput screening assay for a particular target is developed and validated, the 'hit identification campaign' can begin. In this phase of the process, the high throughput screen is scaled up with the use of robots and automated processes to enable the screening of dozens, hundreds, thousands, or even millions of compounds, which are dispensed automatically into the wells of each multi-well plate by robots. The plates may be further manipulated without

human intervention—incubated, shaken, washed, and analyzed by measurement of absorbance, fluorescence, luminescence, microscopy, or other types of optical or physical measurements. Optical measurements are generally preferred as these are rapid, contactless, and noninvasive.

Once the experiment has been completed, the data analysis can begin. The measurements are analyzed and compared against positive controls, negative control, and tool compounds with known activities to identify a particular set of compounds which have promising activity. At this point, positive hits may be compared against orthogonal positive (other activity assays) or negative (toxicity) screening assays. Once a large library of compounds or biologics has been down selected to a small number, the 'hits' become 'leads.' At this point, the large library of molecules is downselected to a manageable subset for closer investigation with lower throughput assays, or carried forward into targeted development by structural evolution or rational medicinal chemistry efforts illuminated by crystal structure or mechanistic studies. At this stage, the molecule may begin targeted development including counter screens, and PK/PD/toxicology studies *in vivo*. Nontoxic molecules validated as efficacious in small and large animal models of disease then become drug candidates and move into human testing.

1.3 Types of Biologic Drugs

Biologic drugs are made of the same building blocks (amino acids, nucleotides, and carbohydrates) that make up naturally occurring biomacromolecules (proteins, DNA, and RNA). The most developed classes of biologic drug are blocking monoclonal antibodies[8] and similar receptor decoy molecules,[9] and enzyme/protein replacement or supplementation therapies. A second, more recently developed class of drugs modulate gene expression and RNA expression through complementary base-pairing to the intracellular oligonucleotide sequence of interest.

These drugs exploit one of several pathways to modulate gene expression, such as mRNA splice modulation in the spliceosome (*e.g.*, eteplirsen and nusinersen), mRNA degradation *via* nuclear RNAse H (*e.g.*, fomivirsen, mipomersen, and inotersen), RNA interference using the cytosolic RNA-induced silencing complex with siRNA (*e.g.*, patisiran), or gene delivery in the form of genomic or plasmid DNA (*e.g.*, vortigene neparvovec-ryzl and onasemnogene abeparvovec-xioi). Each of these modalities has at least one clinically approved medicine in its class. Finally, several tantalizing approaches have not yet been realized to clinically approved medicines although much work is done towards them,[10] including mRNA delivery for protein replacement and vaccines,[11,12] as well as gene editing technologies which require delivery of DNA-cutting proteins (such as Cas9, zinc finger nucleases, or transcription activator-like effector nucleases) as well as potentially a DNA "donor" sequence which corrects or edits the gene via homology directed repair.[13–15] Cas9 in particular additionally requires a large guide RNA (approximately 100 nt) to enable cutting. All modalities based on nucleic acids require that these medicines reach the cytosol or nucleus of a cell.[13]

1.4 FDA Approved Intracellular Biologic Drugs

At present, there are eight large molecule biologic medicines that have achieved clinical approval by the U.S. F.D.A. with intracellular mechanisms of action. This list excludes vaccines, which could be considered biomacromolecular drugs with intracellular mechanisms of action but are beyond the scope of this dissertation. To date, these have all targeted rare diseases or emergent diseases, although we may soon see an approved siRNA therapeutic to reduce levels of low-density lipoprotein C (LDL-C) to reduce cardiovascular risk in inclisiran, which has now accumulated over 3,000 patient-years of remarkable safety and efficacy data. These eight drugs

target only four organ systems: the eye, the central nervous system, the liver, and muscle, and each has unique properties that set it apart from the others. Six of these medicines are fully synthetic and extensively modified oligonucleotides or oligonucleotide mimetics; for a review of these chemical modifications see a review by Y. Sanghvi,[16] while the other two medicines are adenovirus-associated virus based gene therapy platforms generated in mammalian cell culture.

1.4.1 Fomivirsen (1998)

Fomivirsen, developed by Isis Pharmaceuticals (now Ionis) and marketed as VITRAVENE™ was approved by the FDA on August 26, 1998 for the local treatment of cytomegalovirus (hCMV) retinitis in patients with acquired immunodeficiency syndrome (AIDS).[17] Vitravene is a 21 nucleotide long antisense oligonucleotide with a molecular weight of 7122 g/mol. Its only modification from naturally occurring oligonucleotide is a fully phosphorothioated backbone. It was administered as an intravitreal injection of 1.625 mg oligonucleotide in buffer. It works by complementary base pairing to the major immediate early region 2 (IE2) of the hCMV mRNA which contains several genes involved in viral replication. The drug was withdrawn from the US market in 2006, due to dwindling numbers of affected AIDS patients as improved antiretroviral therapies effectively halted the progression of HIV to AIDS in the late 1990s and early 2000s for patients with access to advanced medical care. Vitravene remains notable as the first FDA approved medicine to target a gene directly and the first medicine based on an oligonucleotide.[18]

1.4.2 Mipomersen (2013)

Mipomersen, developed by Isis Pharmaceuticals (now Ionis) and Genzyme and marketed as KYNAMRO® was approved by the FDA on January 29, 2013 as an adjunct therapy in the treatment of homozygous familial hypercholesterolemia.[19] Kynamro is a 20 nucleotide long antisense oligonucleotide with molecular weight of 7595 Da and is modified with a fully phosphorothioated backbone, ten 2′-O-(2-methoxyethyl), and ten 5′ cytosine or 5′ uracyl methylations. Patients with homozygous familial hypercholesterolemia have extremely elevated levels of low-density lipoprotein (LDL). Kynamro inhibits liver biosynthesis of apoB, the major protein component of LDL, to reduce circulating levels of LDL. Kynamro is injected as a 200 mg subcutaneous injection once weekly. Kynamro's prescribing information notably includes a so-called "black box warning" that warned patients of hepatotoxicity, elevated alanine aminotransferase, elevated alkaline phosphatase, increases in hepatic fat, and increased risk of progressive liver diseases including steatohepatitis and cirrhosis. Kynamro is notable as the first subcutaneously injected antisesene oligonucleotide and the first to target the liver.

1.4.3 Eteplirsen (2016)

Eteplirsen, developed by Sarepta Pharmaceuticals and marketed as EXONDYS 51® was approved by the FDA on September 19, 2016 as a therapy in the treatment of Duchene muscular dystrophy in pediatric patients with confirmed mutations in the DMD gene which are amenable to exon 51 skipping.[20] Exondys 51 is an antisense morpholino oligonucleotide of 30 repeats with molecular weight of 10305 Da. Exondys 51 functions to induce exon 51 removal to restore the correct translational frame in the DMD mRNA transcript to increase production of a truncated dystrophin protein. Exondys 51 is adminstered as a 30 mg per kg bodyweight infusion over 35 to

60 minutes once weekly. In clinical trials, Exondys 51 resulted in a median increase from 0.16% to 0.44% of normal levels for DMD protein, however the average increase was only 0.1%. Patients treated with Exondys 51 failed to perform better than placebo in a 6-minute walk test in clinical trials. Exondys 51 is notable as receiving a controversial FDA approval despite an independent expert panel recommending rejection.[21] Sarepta's FDA approved packaging includes a warning stating that "a clinical benefit … has not been established." [20] Exondys 51 is the first medicine based on morpholino oligonucleotides and the first oligonucleotide to target muscle.

1.4.4 Nusinersen (2016)

Nusinersen, developed by Isis Pharmaceuticals (now Ionis) in partnership with Biogen and marketed as SPINRAZA® was approved by the FDA in December 23, 2016 as a therapy in the treatment of spinal muscular atrophy in pediatric and adult patients.[22] Spinraza is an 18 nucleotide long splice modifying oligonucleotide with molecular weight of 7501 Da and is modified with a fully phosphorothioated backbone, fully 2′-O-(2-methoxyethyl) modified, and ten 5′ cytosine or 5′ uracyl methylations. Spinraza targets exon 7 of the SMN2 gene transcript to inhibit premature halt of mRNA translation by frame shift mutations to increase levels of SMN2 protein. Spinraza is injected 12 mg (5 mL) at a time for 3 loading doses at 2-week intervals, a fourth loading dose 30 days later, and maintenance doses every 4 months indefinitely. Administration is given as intrathecal injection into the spine following withdrawal of 5 mL cerebrospinal fluid. In clinical trials, 21 of 52 patients (40%) hit key motor function development milestones when treated with Spinraza, compared to 0/30 in the placebo arm. Spinraza is notable

as the first intrathecally administered antisesene oligonucleotide, and the first treatment of any kind for spinal muscular atrophy.[23]

1.4.5 Voretigene Neparvovec-rzyl (2017)

Voretigene neparvovec-rzyl, developed by Spark Therapeutics and marketed as LUXTURNA® was approved by the FDA on October 5, 2018.[24] Luxturna is a live serotype 2 adenovirus-associated-virus based gene therapy to deliver a copy of the RPE65 gene to patients with confirmed bi-allelic mutation associated retinal dystrophy and viable retinal cells. Luxturna is administered as 1.5×10^{11} vector genomes by subretinal injection to each eye. Luxturna is manufactured in HEK 293-T cells. RPE65 is a 65 kDa human retinal pigment epithelial protein which is a critical component of the retinoid cycle. In clinical trials, Luxturna treatment improved the vision function score by a median of 2 points on a six-point scale, compared to 0 points for the control ($p = 0.001$), and these improvements were stable for the 2 year study duration. Luxturna is notable as the first FDA approved viral gene therapy for use in humans and the first treatment for RPE65-mediated retinal dystrophy. Luxturna is also notable as the most expensive medicine at the time of its release, at an estimated $850,000 per patient.[25]

1.4.6 Patisiran (2018)

Patisiran lipid complex, developed by Alnylam Pharmaceuticals and marketed as ONPATTRO® was approved by the FDA on August 10, 2018 as a therapy in the treatment of hereditary transthyretin-mediated amyloidosis (hATTR) in adult patients.[26] Onpattro is formulated as a 10 mg / 5 mL mixture of siRNA and lipids. The Onpattro siRNA is a double stranded RNA duplex of a central 19-mer double stranded region with two dT overhangs on each

side. The siRNA has a molecular weight of 14304 Da and is formulated into a nanoscale lipid complex mixture including the ionizable lipid DLin-MCe-DMA and a 2000 Da molecular weight PEG corona. Onpattro targets a genetically conserved sequence in the 3' untranslated region of mutant and wild type transthyretin (TTR) mRNA to induce silencing of this gene in liver hepatocytes. Onpattro is injected at a 30 mg dose in patients weighing 100 kg or more and 0.3 mg / kg bodyweight for patients weighing less than 100 kg once every 3 weeks. Administration is given as intravenous infusion over 80 minutes following the administration of an intravenous corticosteroid, oral acetaminophen, and intravenous H1 and H2 histamine blockers. Onpattro must be filtered before administration. In clinical trials, patients treated with Onpattro improved on several measures of neuronal function (e.g., -6.0 versus +28.0 on the mNIS+7 score over 18 months; higher scores indicate increased impairment). Onpattro lipid complex is notable for several reasons: it was the first clinically approved therapy for hATTR, the first siRNA medicine, and the first oligonucleotide medicine delivered using a nanoscale drug carrier. Further, it is the only non-viral oligonucleotide therapy to include an active endosomal escape mechanism.[27]

1.4.7 Inotersen (2018)

Inotersen, developed by Ionis Pharmaceuticals and marketed as TEGSEDI® was approved by the FDA on October 5, 2018.[28] Like Onpattro, Tegsedi is approved for the treatment of hereditary transthyretin-mediated amyloidosis (hATTR) in adult patients. Tegsedi is administered as a 284 mg weekly subcutaneous injection. The Tegsedi antisense oligonucleotide is a 20-mer with a molecular weight of 7183 Da. Tegsedi targets both mutant and wild type transthyretin mRNA to induce silencing of this gene in liver hepatocytes. In clinical trials,

patients treated with Tegsedi experienced disease stabilization (i.e., +1.0 versus +12.7 on the mNIS+7 score at 70 weeks; higher scores indicate increased impairment). Like the similar Kynamro, Tegsedi too bears a "black box warning." The FDA warns Tegsedi can cause thrombocytopenia and glomerulonephritis, which are emerging as potential platform risks for phosphorothioated antisense oligonucleotides.

1.4.8 Onasemnogene Abeparvovec-xioi (2019)

Onasemnogene abeparvovec-xioi, developed by AveXis, a Novartis company, and marketed as ZOLGENSMA® was approved by the FDA on May 24, 2019.[29] Zolgensma is a live serotype 9 adenovirus-associated-virus based gene therapy to deliver a copy of the SMN1 gene to pediatric patients of less than 2 years of age. Zolgensma is administered as 1.1×10^{14} vector genomes per kg bodyweight by intravenous infusion. In clinical trials, Zolgensma treatment supported improved motor neuron development compared to the natural progression of the disease. At the study cutoff date, 19/21 patients were alive while 1 died and 1 withdrew from the study, but natural history studies predicted this population to have only 25% survival (5.25/21) at this timepoint. Further, 10/21 patients were able to sit without support—0 patients would be expected to do so based on natural history studies. Zolgensma contains a black box warning of potential for acute serious liver injury. Zolgensma is notable as the most expensive medicine created to date, with an estimated price tag of $2.1 Mn for its single application.[25]

1.4.9 Excluded Therapeutics

Two FDA approved therapeutics are often called 'gene therapies,' but are, however, excluded from this section because they are not biologic drugs with intracellular mechanisms of

action. Axicabtagene ciloleucel (YESCARTA®) and tisagenlecleucel (KYMRIAH®) are both chimeric antigen T cell products (CAR-T) approved by the FDA in late 2017 which are manufactured from a patient's own blood cells. Both of these products use a patient's own cells to manufacture a population of cells that express a chimeric antigen receptor, which is introduced using viral gene transfer—in the case of KYMRIAH®, a lentivirus derived from HIV is used to stably integrate a transgene into the cell genome, while YESCARTA® uses a γ-retroviral vector. However, these gene transfer steps happen *ex vivo* before the cells are reintroduced, and thus, the drug product (the engineered cells) cannot be said to have intracellular mechanisms of action.

1.4.10 Summary

These exciting medicines represent recent paradigm shifts and may be the start of a wave of new medicines to treat rare diseases which previously had been ignored due to the high risk of traditional drug development. Notably, however, all of these therapies seem quite opportunistic—seemingly perfect diseases to match the technologies that had been developed. For instance, it is well known that both nanoparticles (i.e., Onpattro) and phosphorothioated antisense oligonucleotides (Kynamro and Tegsedi) naturally accumulate within the liver when these drugs reach systemic circulation—so it is no coincidence that these medicines target proteins made in the liver. Likewise, several of these medicines target cell types within enclosed pharmacological compartments separate from systemic circulation, e.g., the retina (Vitravene and Luxturna) and the central nervous system (Spinraza). Of all these medicines, three have active carrier systems—Onpattro is formulated into a lipid nanoparticle, while Luxturna and Zolgensma are viral formulations whose protein coats confer tissue selectivity and endosomal escape. Formulation of a therapeutic with a lipid nanoparticle or viral coat enables specific tissue type

uptake and intracellular endosomal release. Of the other molecules, there may be a clear upper limit to the molecular weight for carrier free drug delivery: Vitravene, Kynamro, Exondys 51, Spinraza, and Tegsedi are all formulated without delivery systems, and have molecular weights of 7122, 7595, 10305, 7501, and 7183 g/mol respectively. Given the outstanding questions surrounding the clinical efficacy of Exondys 51, it is notable that the other approved medicines' molecular weights fall within a quite narrow range between 7000 and 8000 g/mol. Finally, a clear trend emerges regarding clinical pharmacokinetics—medicines directly injected into confined pharmacologic compartments (*i.e.*, the eye or the intrathecal space) require drastically lower doses for Vitravene (1.625 mg per administration) and Spinraza (12 mg per administration) than systemically administered drugs that act in the liver. Of the systemically administered drugs (Kynamro, Exondys 51, and Tegsedi), the two which target the liver have much lower dosing (Kynamro, 10.4 g/year; Tegsedi, 14.8 g/year) than Exondys 51, which targets muscle (78 g per year for a 50 kg patient). Future development should closely examine diseases which affect the CNS, eye, and liver for opportunities in antisense oligonucleotides, and apply the insights from the development of this class of therapeutic.

Two particular advancements, which I alluded to at the start of this chapter, are particularly interesting and worth mentioning due to their shared chemistry. Givosiran, invented and developed by Alnylam, targets aminolevulinic acid synthase 1 in the liver, the inhibition of which prevents acute porphyria attacks in patients with acute hepatic porphyria as shown in recent successful Phase 3 clinical trial results.[30] Inclisiran, invented by Alnylam and developed by The Medicines Company, is an siRNA-based drug currently undergoing Phase III clinical trials to reduce the levels of LDL-C by reducing liver expression of the PCSK9 receptor.[31] Both of these molecules represent Alnylam's latest siRNA chemistry and GalNAc targeting platform,

which uses a trivalent sugar moiety to target the siRNA to hepatocytes *via* receptor mediated endocytosis through the asialoglycoprotein receptor.[32,33] Critically, their optimized design allows extremely infrequent subcutaneous dosing (once per month for givosiran; twice annually for inclisiran) which provide sustained and persistent reduction their target genes. Inclisiran will mark the first intracellular biologic designed for a non-rare disease indication—cardiovascular disease. Thousands of patients have been enrolled in the ORION series of trials for inclisrian to date, and topline results for the three pivotal trial are expected in Q3 2019.

While the future impact of this class of medicines remains to be seen, these drugs have already given patients with rare diseases the gift of sight, improved their ability to walk, sit up, and breathe without assistance, and live longer, more fulfilling lives. This promising class of medicines deserve more attention in development, and may benefit from nanoscale drug delivery systems, especially given potential immunogenicity of viral carriers and potential side effects of off-target systemic delivery.

1.5 Enabling Intracellular Delivery of Biologic Drugs

Our group has developed several classes of drug delivery polymers for the intracellular delivery of biomacromolecular drugs. These polymers electrostatically complex with biomacromolecular drug cargo to increase intracellular accumulation. Further, these polymers are generally designed to exhibit pK_a in the range of early to late endosomes, which induces endosomal membrane disruption and biologic drug cargo release to the cytosol. Throughout this dissertation, I use two dissimilar polymer families to study mechanisms of cellular endocytosis and intracellular endosomal disruption: one anionic homopolymer, poly(propylacrylic acid), which our group has explored for the delivery of cationic cargoes such as cell penetrating

peptides, and one cationic diblock copolymer, PEG-b-(DMAEMA-co-BMA), which we have used for anionic cargoes such as nucleic acids.

1.5.1 Poly(propylacrylic acid)

Poly(propylacrylic acid) (PPAA) is an anionic, pH-responsive homopolymer of propylacrylic acid. In a pair of papers by Evans *et al.*,[34,35] we recently showed that PPAA was useful as a delivery reagent for the intracellular delivery of cationic peptide inhibitors of protein kinases, which are notoriously difficult to address through conventional small molecules due to their high homology within and across families and their disparate effects in different tissues. This polymer had been designed to encapsulate the cationic peptide MK2i into MK2i-NPs with an overall net negative charge, which unexpectedly drives higher cellular uptake than the positively charged peptide alone. These findings motivated exploration in Chapter 2 into how the physicochemical properties of PPAA-based MK2i-NPs affect uptake, cellular processing, and intracellular trafficking of the therapeutic MK2i payload. Understanding the cellular mechanisms underlying the enhanced cellular uptake and altered cellular trafficking of MK2i-NPs may provide insights generalizable to intracellular delivery of peptides and other biomacromolecular drugs. Further, this polymer system is used in Chapter 4 to validate new assays for endosomal disruption as it exhibits relevant levels of endosomal disruption even without carrying any drug.

1.5.2 PEG-b-(DMAEMA-co-BMA)

Polymers based on poly[(ethylene glycol)-b-[(2-(dimethylamino)ethyl methacrylate)-co-(butyl methacrylate)]] [PEG-(DMAEMA-co-BMA)] have been widely explored within our group for use as a delivery vehicle for siRNAs,[36] plasmid DNAs,[37] and locked nucleic acids,[38]

and can be formulated to enhance the delivery of peptide nucleic acids when co-formulated with nanoscale mesoporous silicon particles.[39] PEG-(DMAEMA-co-BMA) polymers have tunable pH responsivity based on the overall molecular weight and molar ratio of cationic DMAEMA to hydrophobic BMA. Early optimization studies by Nelson *et al*.[36,37] on this polymer family showed that a balanced ratio of DMAEMA to BMA of approximately 50:50 mol% (50B) had optimal properties for pH triggered endosomal disruption and siRNA release. The 50B polymer forms stable nanoparticles encapsulating siRNA which exhibit pH-dependent membrane disruption at a pH range ideally tuned for intracellular delivery of siRNA by endosome disruption. Further, 50B particles are stable in serum and show potency as *in vivo* carriers for siRNA delivery. In Chapter 3, we use this polymer family to further explore the physicochemical parameter space that underlies intracellular endosomal disruption using a novel assay developed in Chapter 2.

1.6 References

(1) Human Insulin Receives FDA Approval. *FDA Drug Bull.* **1982**, *12* (3), 18–19.

(2) Valeur, E.; Guéret, S. M.; Adihou, H.; Gopalakrishnan, R.; Lemurell, M.; Waldmann, H.; Grossmann, T. N.; Plowright, A. T. New Modalities for Challenging Targets in Drug Discovery. *Angewandte Chemie - International Edition*. 2017.

(3) Shukla, A. A.; Wolfe, L. S.; Mostafa, S. S.; Norman, C. Evolving Trends in MAb Production Processes. *Bioeng. Transl. Med.* **2017**.

(4) Ban, T. A. The Role of Serendipity in Drug Discovery. *Dialogues Clin. Neurosci.* **2006**.

(5) Wildey, M. J.; Haunso, A.; Tudor, M.; Webb, M.; Connick, J. H. High-Throughput Screening. In *Annual Reports in Medicinal Chemistry*; 2017.

(6) Bleicher, K. H.; Böhm, H.-J.; Müller, K.; Alanine, A. I. Hit and Lead Generation: Beyond High-Throughput Screening. *Nat. Rev. Drug Discov.* **2003**.

(7) Hughes, J. P.; Rees, S. S.; Kalindjian, S. B.; Philpott, K. L. Principles of Early Drug Discovery. *British Journal of Pharmacology*. 2011.

(8) Singh, S.; Kumar, N. K.; Dwiwedi, P.; Charan, J.; Kaur, R.; Sidhu, P.; Chugh, V. K. Monoclonal Antibodies: A Review. *Curr. Clin. Pharmacol.* **2018**, *13* (2), 85–99.

(9) Pugsley, M. K. Etanercept Immunex. *Curr. Opin. Investig. Drugs* **2001**, *2* (12).

(10) Yin, H.; Kanasty, R. L.; Eltoukhy, A. A.; Vegas, A. J.; Dorkin, J. R.; Anderson, D. G. Non-Viral Vectors for Gene-Based Therapy. *Nat. Rev. Genet.* **2014**, *15* (8), 541–555.

(11) Kaczmarek, J. C.; Patel, A. K.; Kauffman, K. J.; Fenton, O. S.; Webber, M. J.; Heartlein, M. W.; DeRosa, F.; Anderson, D. G. Polymer–Lipid Nanoparticles for Systemic Delivery of MRNA to the Lungs. *Angew. Chemie - Int. Ed.* **2016**.

(12) Guan, S.; Rosenecker, J. Nanotechnologies in Delivery of MRNA Therapeutics Using

Nonviral Vector-Based Delivery Systems. *Gene Ther.* **2017**.

(13) Patel, S.; Ashwanikumar, N.; Robinson, E.; Duross, A.; Sun, C.; Murphy-Benenato, K. E.; Mihai, C.; Almarsson, Ö.; Sahay, G. Boosting Intracellular Delivery of Lipid Nanoparticle-Encapsulated MRNA. *Nano Lett.* **2017**.

(14) Yin, H.; Song, C. Q.; Dorkin, J. R.; Zhu, L. J.; Li, Y.; Wu, Q.; Park, A.; Yang, J.; Suresh, S.; Bizhanova, A.; Gupta, A.; Bolukbasi, M. F.; Walsh, S.; Bogorad, R. L.; Gao, G.; Weng, Z.; Dong, Y.; Koteliansky, V.; Wolfe, S. A.; et al. Therapeutic Genome Editing by Combined Viral and Non-Viral Delivery of CRISPR System Components in Vivo. *Nat. Biotechnol.* **2016**.

(15) Miller, J. B.; Zhang, S.; Kos, P.; Xiong, H.; Zhou, K.; Perelman, S. S.; Zhu, H.; Siegwart, D. J. Non-Viral CRISPR/Cas Gene Editing In Vitro and In Vivo Enabled by Synthetic Nanoparticle Co-Delivery of Cas9 MRNA and SgRNA. *Angew. Chemie - Int. Ed.* **2017**.

(16) Sanghvi, Y. S. CHAPTER 19: Large-Scale Automated Synthesis of Therapeutic Oligonucleotides: A Status Update. In *RSC Drug Discovery Series*; 2019.

(17) FDA. Package Insert - VITRAVENE https://www.accessdata.fda.gov/drugsatfda_docs/nda/98/20961_Vitravene_prntlbl.pdf (accessed Jul 4, 2019).

(18) Marwick, C. First “antisense” Drug Will Treat CMV Retinitis. *Journal of the American Medical Association*. American Medical Association September 9, 1998, p 871.

(19) FDA. Package Insert - KYNAMRO https://www.accessdata.fda.gov/drugsatfda_docs/nda/2013/203568Orig1s000Lbl.pdf (accessed Jul 4, 2019).

(20) FDA. Package Insert - EXONDYS 51 www.fda.gov/medwatch. (accessed Jul 4, 2019).

(21) Tavernise, S. F.D.A. Approves Muscular Dystrophy Drug That Patients Lobbied For - The New York Times https://www.nytimes.com/2016/09/20/business/fda-approves-muscular-dystrophy-drug-that-patients-lobbied-for.html (accessed Jul 4, 2019).

(22) FDA. Package Insert - SPINRAZA https://www.accessdata.fda.gov/drugsatfda_docs/label/2016/209531lbl.pdf (accessed Jul 4, 2019).

(23) 2016. Costly Drug for Fatal Muscular Disease Wins F.D.A. Approval - The New York Times https://www.nytimes.com/2016/12/30/business/spinraza-price.html (accessed Jul 4, 2019).

(24) FDA. Package Insert - LUXTURNA https://www.fda.gov/media/109906/download (accessed Jul 4, 2019).

(25) Thomas, K. This New Treatment Could Save the Lives of Babies. But It Costs $2.1 Million. - The New York Times https://www.nytimes.com/2019/05/24/health/zolgensma-gene-therapy-drug.html (accessed Jul 4, 2019).

(26) FDA. Package Insert - ONPATTRO https://www.accessdata.fda.gov/drugsatfda_docs/nda/2018/210922Orig1s000lbl.pdf (accessed Jul 4, 2019).

(27) Alnylam Pharmaceuticals. Alnylam Announces First-Ever FDA Approval of an RNAi Therapeutic, ONPATTRO™ (patisiran) for the Treatment of the Polyneuropathy of Hereditary Transthyretin-Mediated Amyloidosis in Adults | Alnylam Pharmaceuticals, Inc. http://investors.alnylam.com/news-releases/news-release-details/alnylam-announces-first-ever-fda-approval-rnai-therapeutic (accessed Jul 4, 2019).

(28) FDA. Package Insert - TEGSEDI

https://www.accessdata.fda.gov/drugsatfda_docs/nda/2018/211172Orig1s000LBL.pdf (accessed Jul 4, 2019).

(29) FDA. Package Insert - ZOLGENSMA https://www.fda.gov/media/126109/download (accessed Jul 4, 2019).

(30) Balwani, M.; Gouya, L.; Rees, D.; Stein, P.; Stölzel, U.; Aguilera, P.; Bissell, D. M.; Bonkovsky, H.; Keel, S.; Parker, C.; Phillips, J.; Silver, S.; Windyga, J.; D'avola, D.; Ross, G.; Stewart, P.; Ritchie, B.; Oh, J.; Harper, P.; et al. GS-14-ENVISION, a Phase 3 Study to Evaluate Efficacy and Safety of Givosiran, an Investigational RNAi Therapeutic Targeting Aminolevulinic Acid Synthase 1, in Acute Hepatic Porphyria Patients. *J. Hepatol.* **2019**.

(31) Fitzgerald, K.; White, S.; Borodovsky, A.; Bettencourt, B. R.; Strahs, A.; Clausen, V.; Wijngaard, P.; Horton, J. D.; Taubel, J.; Brooks, A.; Fernando, C.; Kauffman, R. S.; Kallend, D.; Vaishnaw, A.; Simon, A. A Highly Durable RNAi Therapeutic Inhibitor of PCSK9. *N. Engl. J. Med.* **2016**.

(32) Nair, J. K.; Willoughby, J. L. S.; Chan, A.; Charisse, K.; Alam, M. R.; Wang, Q.; Hoekstra, M.; Kandasamy, P.; Kel'in, A. V.; Milstein, S.; Taneja, N.; O'Shea, J.; Shaikh, S.; Zhang, L.; van der Sluis, R. J.; Jung, M. E.; Akinc, A.; Hutabarat, R.; Kuchimanchi, S.; et al. Multivalent N-Acetylgalactosamine-Conjugated SiRNA Localizes in Hepatocytes and Elicits Robust RNAi-Mediated Gene Silencing upon Subcutaneous Administration. *J. Am. Chem. Soc.* **2014**, *136* (49), 16958–16961.

(33) Rajeev, K. G.; Nair, J. K.; Jayaraman, M.; Charisse, K.; Taneja, N.; O'Shea, J.; Willoughby, J. L. S.; Yucius, K.; Nguyen, T.; Shulga-Morskaya, S.; Milstein, S.; Liebow, A.; Querbes, W.; Borodovsky, A.; Fitzgerald, K.; Maier, M. A.; Manoharan, M.

Hepatocyte-Specific Delivery of SiRNAs Conjugated to Novel Non-Nucleosidic Trivalent N-Acetylgalactosamine Elicits Robust Gene Silencing in Vivo. *ChemBioChem* **2015**.

(34) Evans, B. C.; Hocking, K. M.; Osgood, M. J.; Voskresensky, I.; Dmowska, J.; Kilchrist, K. V.; Brophy, C. M.; Duvall, C. L. MK2 Inhibitory Peptide Delivered in Nanopolyplexes Prevents Vascular Graft Intimal Hyperplasia. *Sci. Transl. Med.* **2015**, *7* (291), 291ra95.

(35) Evans, B. C.; Hocking, K. M.; Kilchrist, K. V.; Wise, E. S.; Brophy, C. M.; Duvall, C. L. Endosomolytic Nano-Polyplex Platform Technology for Cytosolic Peptide Delivery To Inhibit Pathological Vasoconstriction. *ACS Nano* **2015**, *9* (6), 5893–5907.

(36) Nelson, C. E.; Kintzing, J. R.; Hanna, A.; Shannon, J. M.; Gupta, M. K.; Duvall, C. L. Balancing Cationic and Hydrophobic Content of PEGylated SiRNA Polyplexes Enhances Endosome Escape, Stability, Blood Circulation Time, and Bioactivity in Vivo. *ACS Nano* **2013**, *7* (10), 8870–8880.

(37) Adolph, E. J.; Nelson, C. E.; Werfel, T. A.; Guo, R.; Davidson, J. M.; Guelcher, S. A.; Duvall, C. L. Enhanced Performance of Plasmid DNA Polyplexes Stabilized by a Combination of Core Hydrophobicity and Surface PEGylation. *J. Mater. Chem. B* **2014**.

(38) Werfel, T. A.; Hocking, K. M.; Kilchrist, K. V; Brophy, C. M.; Duvall, C. L. Abstract 12: Nanotechnology-Enabled Anti-Mir-320 Therapy for Inhibiting Pathological Vasoconstriction. In *Arteriosclerosis, Thrombosis, and Vascular Biology*; American Heart Association, 2016; Vol. 36, pp A12–A12.

(39) Beavers, K. R.; Werfel, T. A.; Shen, T.; Kavanaugh, T. E.; Kilchrist, K. V.; Mares, J. W.; Fain, J. S.; Wiese, C. B.; Vickers, K. C.; Weiss, S. M.; Duvall, C. L. Porous Silicon and Polymer Nanocomposites for Delivery of Peptide Nucleic Acids as Anti-MicroRNA Therapies. *Adv. Mater.* **2016**, *28* (36), 7984–7992.

CHAPTER 2

MECHANISM OF ENHANCED CELLULAR UPTAKE AND CYTOSOLIC RETENTION OF MK2 INHIBITORY PEPTIDE NANO-POLYPLEXES

Adapted from

"Mechanism of Enhanced Cellular Uptake and Cytosolic Retention of MK2 Inhibitory Peptide Nano-polyplexes,"

published in *Cellular and Molecular Bioengineering* September 2016

by

Kameron V. Kilchrist, Brian C. Evans, Colleen M. Brophy, and Craig L. Duvall.

doi.org/10.1007/s12195-016-0446-7

In this chapter, I seek to address the first significant cellular barrier that nanoscale drug delivery faces—the cellular membrane. This work was primarily motivated to understand the molecular mechanisms that underpin the success of our most developed and exciting nanoscale drug delivery system, MK2i-NP, which was designed to enable intracellular delivery of an MK2 inhibitory peptide in venous coronary artery bypass grafts to prevent intimal hyperplasia. MK2i-NP was designed to increase endosomal escape, although it also causes enhanced cellular uptake and intracellular retention. The work below uncovered an interesting mechanism of cellular uptake, which subsequently informed a successful resubmission of an R01 grant to the NIH NHLBI (HL122347), and which led to a systematic investigation of polymer interactions with cell membranes for the enhancement of peptide delivery, which we describe in an upcoming

paper by first author Dr. Eric Dailing. The work in this chapter reveals that polymers that interact with cell membranes without toxicity may enable cytosolic delivery of polycations more broadly. Indeed, our subsequent work by first author Dr. Brian Evans confirms this is a generalizable delivery platform to enhance cellular uptake and bioactivity of a wide variety of cationic cargos, including other polycationic peptides, cationic nanoparticles, and cationized proteins. Mechanistic investigations of cellular uptake and endosomal disruption such as these are required to better understand the physicochemical parameters underpinning nanoscale drug delivery formulations.

2.1 Abstract

Electrostatic complexation of a cationic MAPKAP kinase 2 inhibitory (MK2i) peptide with the anionic, pH-responsive polymer poly(propylacrylic acid) (PPAA) yields MK2i nano-polyplexes (MK2i-NPs) that significantly increase peptide uptake and intracellular retention. This study focused on elucidating the mechanism of MK2i-NP cellular uptake and intracellular trafficking in vascular smooth muscle cells. Small molecule inhibition of various endocytic pathways showed that MK2i-NP cellular uptake involves both macropinocytosis and clathrin mediated endocytosis, whereas the free peptide exclusively utilizes clathrin mediated endocytosis for cell entry. Scanning electron microscopy studies revealed that MK2i-NPs, but not free MK2i peptide, induce cellular membrane ruffling consistent with macropinocytosis. TEM confirmed that MK2i-NPs induce macropinosome formation and achieve MK2i endo-lysosomal escape and cytosolic delivery. Finally, a novel technique based on recruitment of Galectin-8-YFP was utilized to demonstrate that MK2i-NPs cause endosomal disruption within 30 min of uptake. These new insights on the relationship between NP physicochemical properties

and cellular uptake and trafficking can potentially be applied to further optimize the MK2i-NP system and more broadly toward the rational engineering of nano-scale constructs for the intracellular delivery of biologic drugs.

2.2 Introduction

Intracellular-acting peptides have the potential to be applied as powerful research tools to modulate kinase activity, alter protein-protein interactions, and elucidate specific protein functions[6,28,32,45]. Peptides can modulate targets not druggable by conventional small molecules and can be rationally designed to have more predictable and specific activity. However, clinical use of peptides is limited due to lack of intracellular bioavailability. This lack of bioavailability arises because peptides are too large and hydrophilic to diffuse across cell membranes. To overcome this barrier, the majority of peptides used in research are modified with cationic cell penetrating peptides (CPPs) to facilitate plasma membrane transduction. Initial reports suggested that some CPPs may directly translocate the cell membrane, but later studies[39] showed this effect to be an artefact of microscopy. Upon endocytosis, CPPs typically traffic through early and late endosomes before ultimately becoming entrapped in lysosomes[22,27], sequestering a large portion of the drug away from its intracellular binding target. Many research groups have used polymeric nano-carriers to enable endo-lysosomal escape of biologic drugs like nucleic acids and peptides[12,17]. Although debated, the 'proton sponge' mechanism of endosomal escape has been extensively described for nucleic acid delivery systems like polyethyleneimine[2,7]; however, the effects of endosomal escape on the subsequent trafficking of the drug cargo remain unclear[44]. Anionic, pH-responsive carriers like the one described herein have been shown to reduce trafficking into acidifying compartments following CD22-dependent receptor mediated uptake[3].

While the pharmacodynamics of anionic, polymer-based nano-polyplexes (NPs) used for the delivery of both an intracellular acting MAPKAP kinase 2 inhibitory (MK2i) peptide and a peptide mimetic of phosphorylated heat shock protein 20 (p-HSP20) have been thoroughly investigated [18,19], the mechanisms and kinetics of NP uptake and trafficking have not been rigorously studied.

The current studies focus on the comprehensive analysis of an established MK2i-NP formulation, which our group previously developed for the cytosolic delivery of MK2i to vascular smooth muscle cells to prevent intimal hyperplasia and vasospasm[18,19]. A previous study on a therapeutic peptide fused to a CPP by Flynn et al. found that the AZX100 peptide, which comprises the same CPP sequence as MK2i and p-HSP20, was internalized rapidly *via* a lipid raft dependent, caveolae mediated uptake process that was not significantly influenced by actin or dynamin inhibition. This work demonstrated that the majority of internalized peptide was sequestered within the endo-lysosomal system, preventing the peptide from efficiently binding to its target intracellular[22]. Upon phosphorylation, MK2 is translocates from the nucleus to the cytosol, where it phosphorylates downstream mediators in the p38/MAPK signaling axis[30,35]; MK2i binds to and blocks the active site used by MK2 to phosphorylate these downstream mediators[25,33]. MK2i-NPs[18,19], formed by the simple mixing of the cationic MK2i peptide with the anionic, endosomolytic polymer poly(propylacrylic acid) (PPAA) at pH 8, are electrostatically complexed nano-sized structures with a negative zeta potential ($\zeta\sim$ -12 mV). In contrast to the traditional dogma within the biomacromolecular drug delivery field that cationic charge should be utilized to enhance intracellular delivery of CPPs[26], polymeric micelles[13,15], and lipoplexes[21], formulation into negatively charged NPs significantly enhances the cellular uptake of CPP-based peptides (e.g., both MK2i and p-HSP20)[19],. MK2i-NPs demonstrate a longer

duration of intracellular retention relative to free MK2i and demonstrated equivalent bioactivity at an order of magnitude lower dose than the free peptide or control, non-endosomolytic nano-polyplexes formed with poly(acrylic acid) (PAA)[18,19]. Both PPAA and PAA contain pH-responsive carboxylate moieties that drive electrostatic complexation with cationic MK2i peptide, however, due to the α-alkyl substitution of a pendant propyl chain, the carboxylate of PPAA has an effective acid dissociation constant (pK_a) of ~6.8 (whereas the pK_a of the pendant carboxylate of PAA is ~4.3). This difference results in PPAA, but not PAA, demonstrating pH-dependent membrane disruptive activity at pH values encountered during endo-lysosomal trafficking (i.e., pH 4.5 – pH 7.4)[41]. Although formulation with either polymer at an optimized charge ratio formed NPs with statistically equivalent size and surface charge, control NPs formulated with non-endosomolytic PAA did not enhance cellular uptake or bioactivity. These findings motivated exploration into how the physicochemical properties of PPAA-based MK2i-NPs affect uptake, cellular processing, and intracellular trafficking of the therapeutic MK2i payload. Understanding the cellular mechanisms underlying the enhanced cellular uptake and altered cellular trafficking of MK2i-NPs may provide insights generalizable to intracellular delivery of peptides and other biomacromolecular drugs.

2.3 Materials and Methods

2.3.1 Materials

Poly(propylacrylic acid) and MK2i were synthesized as previously reported[18,19]. MK2i-NPs were formulated (**Figure 2.1a**) and characterized as previously described[18]. Endocytic inhibitors were obtained from Sigma-Aldrich. MK2i peptide was labeled with Alexa 488-NHS or Alexa 568-NHS (ThermoFisher Scientific) according to manufacturer instructions and purified

with a desalting column (PD10 Miditrap, GE). Conjugation efficiency and conjugate purity were verified by UV-VIS spectroscopy. Fluorescently labeled MK2i peptide was used to formulate fluorescently labeled MK2i-NPs. To formulate gold labeled MK2i-NPs (Au-MK2i-NPs), a solution of 10 nm gold nanoparticles stabilized in PBS (Sigma-Aldrich 752584) was first added to PPAA, to which MK2i was subsequently added. Au loading into MK2i-NPs was confirmed by the complete disappearance of the 10 nm gold peak in DLS measurements.

2.3.2 Cell Culture

Cell culture reagents were purchased from Gibco/Thermo Fisher Scientific (Waltham, MA, USA) unless otherwise specified. Human coronary artery vascular smooth muscle cells were obtained from Lonza and grown in ATCC Vascular Cell Basal Medium supplemented with ATCC Vascular Smooth Muscle Cell Growth Kit (ATCC, Manassas, VA, USA), 1% Penicillin-Streptomycin, and Plasmocin prophylactic (Invivogen, San Diego, CA USA). All cultures were maintained in 75cm^2 polystyrene tissue culture flasks in a sterile, 37 °C incubator with a humidified atmosphere supplemented to 5% CO_2 and passaged 1:3 when they reached 75-90% confluence, with media otherwise replaced every other day. Primary cells were used at passages less than 9. The embryonic rat aortic smooth muscle cell line A7r5 was also used for TEM and confocal studies. A7r5, HEK 239T, and their stable derivatives were grown in DMEM supplemented with 10% FBS, 1% penicillin-streptomycin, and 1x ciprofloxacin (GenHunter, Nashville, TN, USA), and supplemented as noted with selection antibiotics to select cells expressing transgenes.

2.3.3 Flow Cytometry Quantification of Peptide Uptake Inhibition

Flow cytometry was performed as previously reported[19], except that before treatment with MK2i-NPs or MK2i peptide, HCAVSMCs were pre-treated with endocytic inhibitors for 30 minutes, before being co-treated with inhibitor and mk2i-NP or peptide treatment. Doses for these inhibitors were verified to be above the published IC_{50} literature values, consistent with other published inhibition studies, and to be in a range that did not cause significant toxicity in our hands in HCAVSMC pilot studies. Briefly, cells were seeded in triplicate in a 24 well plate at 30,000 cells *per* well and allowed to adhere overnight. Cell culture media was replaced with OptiMEM supplemented with 1% FBS, 1% penn-strep, and appropriate doses of each small molecule inhibitor: dynamin, 50 or 100 nM; Nystatin, 50 μg/mL; methyl-β-cyclodextrin, 5 mM; cytochalasin D, 5 μM; 5-(N-ethyl-N-isopropyl)amiloride (EIPA), 50 μM; wortmannin, 10, 50, and 100 nM; amiloride, 50 μM; polyinosinic acid, 50 μg/mL; and dextran sulfate, 100 μg/mL. Fluorescently labeled MK2i-NPs (10 μM) or free MK2i peptide (10 μM) were added to co-treat the cells for 30 minutes. Cells were then washed twice with PBS -/-, trypsinized, and resuspended in 0.1% Trypan blue in PBS (to quench extracellular fluorescence) for analysis on a FACSCalibur flow cytometer equipped with BD CellQuest Pro software (v 5.2). Data was exported and analyzed with FlowJo software (V 7.6.4). Mean fluorescence intensity (MFI) was calculated by gating the cell population *via* forward and side scatter and subtracting the baseline MFI of untreated cells. Relative uptake was calculated by the following equation where $MFI_{Inhibition}$ and $MFI_{No\ Inhibitor}$ are the mean fluorescence intensities calculated for cells pre-treated with inhibitors and solely treated with MK2i-NPs or MK2i peptide, respectively:

$$\text{Relative Uptake} = \left(\frac{MFI_{Inhibition}}{MFI_{No\ Inhibitor}}\right) \quad \text{Eq. 1}$$

2.3.4 Confocal Microscopy

Cells were plated at low confluence (4,000-10,000 cells/well) on an 8-well Nunc Lab-Tek chambered coverslip for confocal microscopy studies. For time course experiments, cells were maintained in a heated chamber with a humidified atmosphere and supplemented with 25 mM HEPES to provide physiologic pH buffering. Confocal image analysis was performed using the Nikon C1si+ system on a Nikon Eclipse Ti-0E inverted microscopy base, Plan Apo VC 20x differential interference contrast N2 objective, 0.75NA, Galvano scanner, and 408/488/543 dichroic mirror. The PMT HV gain, laser power, and display settings were set for maximal SNR based on control biological samples such that negative control samples lacking label had no background fluorescence and positive control samples had no saturated pixels. To ensure no crosstalk between fluorophores, images were acquired sequentially line by line (i.e., line 1 was imaged first with 405 ex / 450 em, then with 488 ex / 515 em before proceeding to line 2). Lack of crosstalk was verified with fluorescence-minus-one controls for all fluorescence channels. Nikon Perfect Focus System was used to ensure image focus. Image acquisition and analysis were performing using Nikon NIS-Elements AR version 4.30.01.

2.3.5 Scanning Electron Microscopy Imaging of Cellular Membrane Morphology

Samples were fixed in 2.5% gluteraldehyde in 0.1M cacodylate buffer (pH 7.4) at 37ºC for 1 hour and then transferred to 4ºC overnight. The samples were washed in 0.1M cacodylate buffer, incubated for 1 hour in 1% osmium tetraoxide at room temperature (RT), and then washed with 0.1M cacodylate buffer. Subsequently, the samples were dehydrated through a graded ethanol series followed by 3 exchanges of 100% ethanol. Samples were then critical point dried on a Tousimis samdri-PVT-3D critical point dryer and mounted on carbon adhesive

attached to aluminum stubs. Samples were then sputter coated with gold/palladium for 90 seconds. Images were taken on FEI Quanta Q250 SEM.

2.3.6 Transmission Electron Microscopy Imaging of Cellular Uptake and Trafficking

Samples were fixed in 2.5% gluteraldehyde in 0.1M cacodylate buffer, pH7.4 at 37ºC for 1 hour then transferred to 4ºC, overnight. The samples were washed in 0.1M cacodylate buffer, then incubated 1 hour in 1% osmium tetraoxide at RT then washed with 0.1M cacodylate buffer. Subsequently, the samples were dehydrated through a graded ethanol series, followed by 3 exchanges of 100% ethanol and 2 exchanges of pure propylene oxide (PO). Dehydrated samples infiltrated with 25% Epon 812 resin and 75% PO for 30 minutes at RT, followed by infiltration with Epon 812 resin and PO [1:1] for 1 hour at RT and subsequent infiltration with fresh Epon 812 resin and PO [1:1] overnight at RT. The samples were subsequently infiltrated with resin for 48 hours and then allowed to polymerize at 60°C for 48 hours. Samples were cut to 500 - 1000 nm thick sections using a Leica Ultracut microtome. Thick sections were contrast stained with 1% toluidine blue and imaged with a Nikon AZ100 microscope to locate cells. 70-80 nm ultra-thin sections were cut and collected on 300-mesh copper grids and then post-stained with 2% uranyl acetate followed by Reynold's lead citrate. Thin samples were imaged on a Philips/FEI Tecnai T12 electron microscope.

2.3.7 Generation of Stably Transfected Cell Lines

Retroviral transfer plasmids encoding galectin/yellow fluorescent protein fusion proteins were kindly gifted by Felix Randow[43]. The retroviral packaging and pseudotyping vectors pUMVC and pCMV-VSV-G (Addgene.com Plasmid #8449 and #8454, respectively) were kind

gifts of Bob Weinberg[42]. Galectin-YPF, pUMVC, and pCMV-VSV-G (9:8:1 mass ratio) were transfected into HEK 239T cells at 50% confluence in T-75 plates using Fugene 6 according to the manufacturer's instructions to produce pseudotyped MMLV retroviral particles. Cell culture media was changed after 24 hours; viral supernatant collected between hours 24-48 and 48-72 hours post-transfection were syringe filtered and frozen at -20 °C until use. A7r5 cells were transduced overnight with 1:10 (v/v) viral supernatant:media and allowed to incubate for 24 hours, at which point cells were transferred into selection media containing Blasticidin (10 μg/ml). After 2 weeks, cells were plated by limiting dilution for single clonal selection and expansion to ensure homogenous expression levels for downstream assays. Successful selection was validated by fluorescence microscopy using non-transfected cells as a control.

2.3.8 Time Lapse Galectin 8 Microscopy

Single cell clonal populations were plated at 5,000 cells/well in chambered coverslips as described for confocal microscopy. Cells were monitored for 3-5 minutes to establish baseline Galectin 8 fluorescence. Cells were then treated for 30 minutes, after which the media was replaced. Live imaging was continued post-wash for at least 3 hours. Images were processed using the "spot detection" algorithm within Nikon NIS-Elements AR version 4.30.01 (Build 1021) and exported to Prism GraphPad and normalized to pre-treatment baseline fluorescence.

2.3.9 Statistics

Statistical analysis was performed *via* one-way ANOVA followed by Tukey's post-hoc test to compare experimental groups. Analyses were done with Microsoft Excel or Graphpad Prism 6 software. Statistical significance was accepted within a 95% confidence limit with a

significance level of $\alpha = 0.05$. Results are presented as arithmetic mean ± SEM graphically. For time-lapse galectin 8 recruitment data, statistical significance was defined by non-overlapping 95% confidence intervals.

2.4 Results

2.4.1 Characterization of Cellular Uptake Mechanisms

To confirm that the A7r5 rat aortic smooth muscle cell line recapitulates the uptake behavior of human coronary artery smooth muscle cells as previously reported[18,19], A7r5 cells were treated with 10 μM fluorescently labeled MK2i-NPs or MK2i peptide. MK2i-NP and MK2i treated cells both show higher mean fluorescence intensity relative to no treatment cells, and MK2i-NP treated A7r5 cells show a 49-fold increase in MFI compared to cells treated with free MK2i peptide (**Figure 2.1b**). These data recapitulate our previous results and validate that formulation of therapeutic CPPs into NPs increases peptide uptake by over an order of magnitude in vascular smooth muscle cells. To confirm these differences qualitatively, we visualized cell peptide uptake by fluorescence confocal microscopy (**Figure 2.1c** and 1.**1d**).

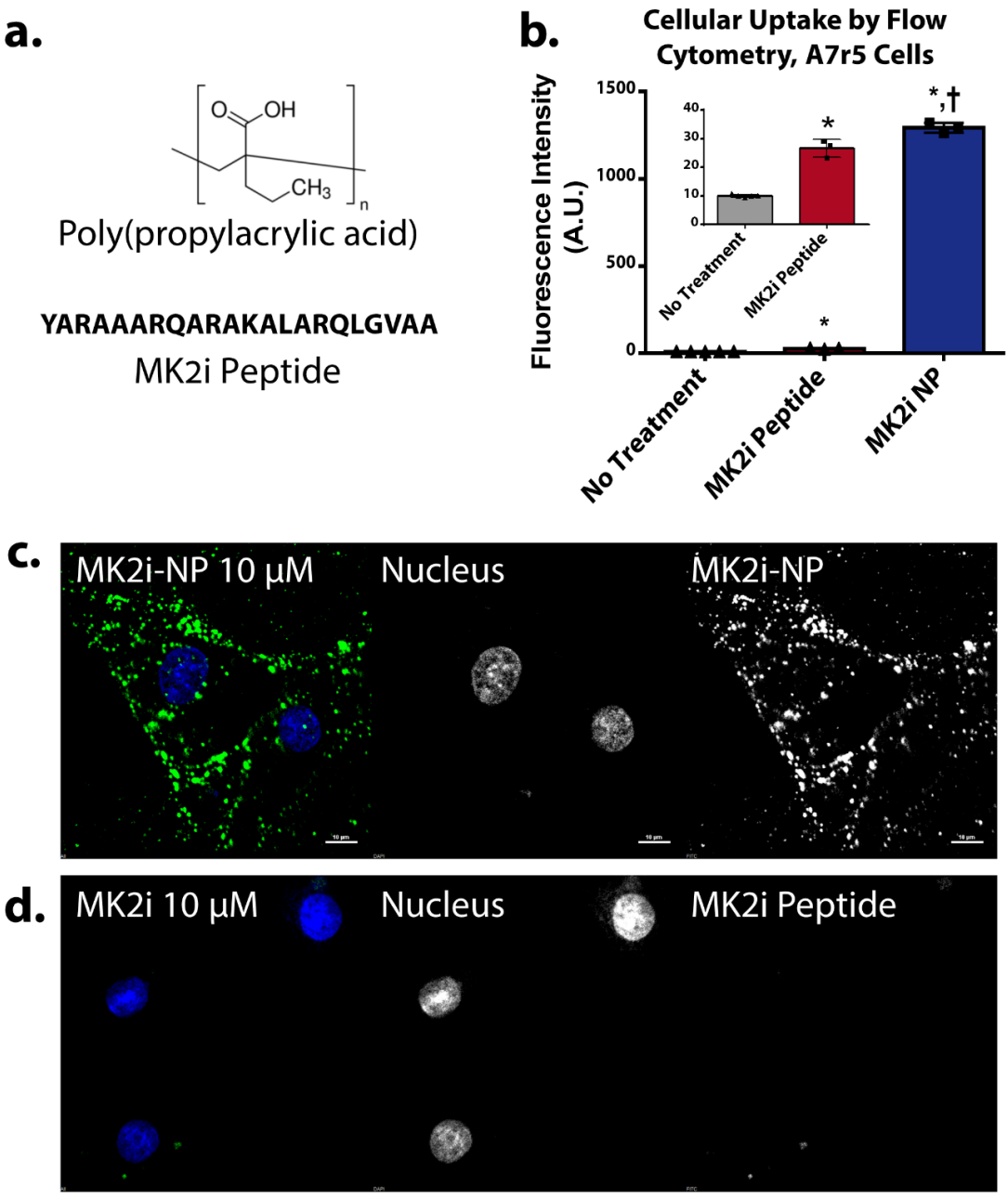

MK2i-NP and MK2i are displayed with equal display settings.

Figure 2.1. NP formulation of MK2i peptide significant enhances cell internalization in A7r5 VSMCs. *(a) Chemical structure of poly(propylacrylic acid) and sequence of MK2i peptide. (b) Flow cytometric mean fluorescence intensity of cells treated with fluorophore-labeled 10 µM MK2i peptide either as free peptide or formulated into MK2i-NPs. (c, d). Fluorescence microscopy images of A7r5 cells after 30 minutes of treatment with 10 µM MK2i-NP or MK2i peptide; scale bar is 10 µm; blue is nuclei, green is labeled MK2i peptide*

To further understand the effects of NP formulation on MK2i uptake, a library of small molecule inhibitors of different endocytic pathways was used (see inhibitor descriptions in **Table 1.1**). Specifically, we sought to investigate: macropinocytosis, which has been implicated in CPP and nanoparticle internalization[26] and can be upregulated by cell surface receptor crosslinking[20,38]; clathrin- and caveolin mediated endocytosis, which has been implicated in MK2i internalization[10,22]; lipid raft mediated endocytosis[10], which has been implicated in MK2i internalization in some cell types; and scavenger receptor mediated uptake, which is known to be highly utilized in smooth muscle cells for uptake of negatively charged, hydrophobic particles like low-density lipoprotein that have similar physicochemical properties to PPAA-based MK2i-NPs[9,11,31].

Table 1.1: Selected inhibitors of endocytosis

Inhibitor	Pathway Inhibited	Mechanism
Wortmannin[20]	Macropinocytosis, phagocytosis	an inhibitor of phosphatidylinositol-4,5-bisphosphate 3-kinase [PI3K], which is required for closure of macropinosomes
Cytochalasin D[37]	Macropinocytosis, phagocytosis	an inhibitor of actin polymerization, which is required for membrane ruffling and macropinosome formation
5-(N-Ethyl-N-isopropyl)amiloride (EIPA) [29]	Macropinocytosis	inhibitor of Rac1/Cdc42 signaling that is required for macropinocytosis
Dynasore[34,46]	Clathrin mediated endocytosis, caveolin mediated endocytosis	an inhibitor of dynamin, a GTPase responsible for clathrin mediated endocytosis, caveolin mediated endocytosis, and the related lipid raft mediated endocytosis
Nystatin[48]	Lipid raft mediated endocytosis	a molecule that binds to and sequesters membrane cholesterol thereby inhibiting lipid raft mediated endocytosis
Methyl-β-cyclodextrin[48]	Lipid-raft mediated endocytosis	Chelates plasma membrane cholesterol, thereby inhibiting lipid-raft mediated endocytosis
Polyinosinic acid[9]	Scavenger receptor mediated endocytosis	Depletes cell surface of scavenger receptors by saturating binding and causing receptor internalization; competitive agonist
Dextran Sulfate ($DxSO_4$) [9]	Scavenger receptor mediated endocytosis	Depletes cell surface of scavenger receptors by saturating binding and causing receptor internalization; competitive agonist

Both MK2i-NP and MK2i peptide uptake were significantly inhibited by dynasore, indicating that clathrin and/or caveolae mediated endocytosis plays a key role in their uptake, consistent with the results previously reported by Brugnano and colleagues for MK2i peptide uptake (which they denote "YARA")[10]. Uptake of MK2i-NPs, but not MK2i, was significantly inhibited by all inhibitors implicated in macropinocytosis (i.e., wortmannin, cytochalasin D, and EIPA). We initially hypothesized that scavenger receptors may play a role in MK2i-NP and/or MK2i uptake due to their negative and positive charge, respectively[5,9,11,31]. However, treatment with the scavenger receptor inhibitors polyinosinic acid or dextran sulfate ($DxSO_4$) had no significant effects on MK2i-NP or MK2i uptake. Furthermore, inhibition of lipid-raft systems *via* nystatin or methyl-β-cyclodextrin pretreatment also showed no significant effects on MK2i-NP or MK2i uptake. Collectively, these data suggest that MK2i-NPs are internalized through macropinocytic mechanisms in addition to the clathrin- and or caveolae mediated endocytic mechanisms responsible for uptake of the free MK2i peptide. The modest (and not statistically significant) increases in internalization of MK2i peptide with wortmannin, cytochalasin D, EIPA, and nystatin treatment are likely due to compensatory uptake mechanisms as previously shown by Brugnano et al.[10]

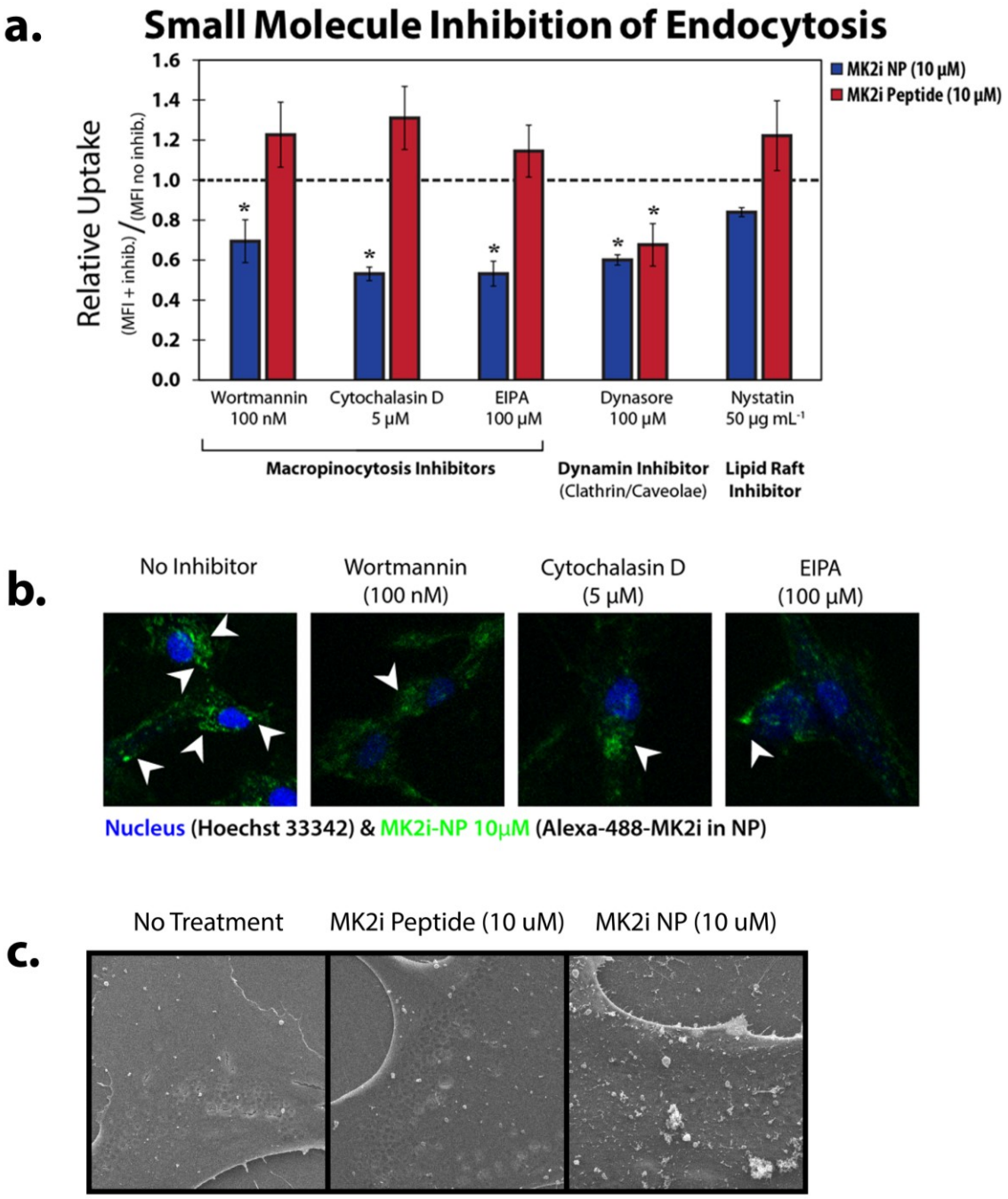

Figure 2.2. MK2i-NPs enter cells through macropinocytosis while free MK2i exclusively utilizes clathrin mediated endocytosis.
(a) Uptake inhibition of macropinocytosis, dynamin, and lipid rafts as measured by flow cytometry. Data is presented as mean fluorescence intensity relative to no treatment control. (b) Confocal micrographs of cells treated with MK2i-NP 10 µM and macropinocytosis inhibitors (c) scanning electron micrographs showing induction of cell surface ruffling indication macropinocytosis of MK2i-NPs

To confirm these results, live cells were treated with macropinocytosis inhibitors and visualized through confocal microscopy imaging (**Figure 2.2b**). Cells treated with any of the macropinocytosis inhibitors showed a marked decrease in the amount of large / macropinosome-like vesicles positive for MK2i-NP fluorescence (white arrows in **Figure 2.2b**). Because macropinocytosis is a process that involves re-organization of the actin cytoskeleton to form membrane protrusions (i.e., pseudopodia and membrane ruffling / blebbing) (**Figure 2.3**) that engulf extracellular fluid, we sought to visualize this mechanism by SEM as previously

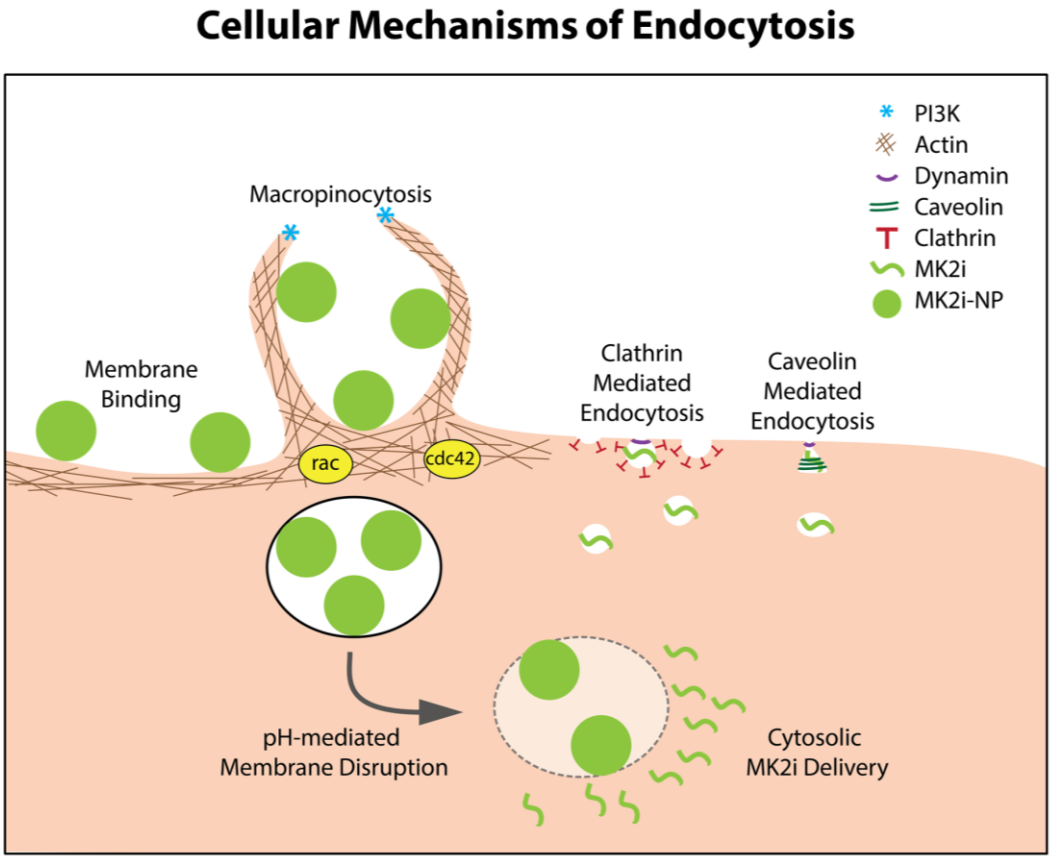

Figure 2.3. Hypothesized MK2i-NP mechanism of endocytosis.
Macropinocytosis is a process of nonspecific internalization of large amounts of extracellular fluid characterized by actin-rich protrusions from the cell surface which close in a phosphoinositide 3-kinase (PI3K) dependent step and rely on Rac/Cdc42 signaling. Clathrin mediated endocytosis and caveolin mediated endocytosis rely on a dynamin dependent closure step for internalization. MK2i-NP is proposed to enhance uptake by binding to external plasma membrane and internalize via macropinocytosis

reported[36]. Cells were treated with 10 μM MK2i-NPs, MK2i, or PBS. As expected, MK2i-NPs, but not MK2i or PBS, induced a high degree of visible membrane ruffling (**Figure 2.2c**).

2.4.2 Transmission Electron Microscopy

TEM imaging was utilized for high resolution visualization of cellular ultrastructure during uptake and intracellular trafficking of gold-labeled MK2i-NPs (Au-MK2i-NPs). Au-MK2i-NP size equivalence with MK2i-NPs and gold loading (~98%) were confirmed by dynamic light scattering (DLS, **Figure 2.S2**). Gold-labeled MK2i peptide was excluded from TEM studies because of concerns that 10 nm gold would significantly affect trafficking of the individual peptide molecules, which are very small relative to the gold (i.e., 2 nm compared to 10 nm diameters for the peptide and gold, respectively). Furthermore, irreversible aggregation and precipitation were apparent upon mixing of the gold label with free MK2i peptide. Therefore, free gold was used as a control. Samples were treated for 30 minutes and thoroughly washed 1x with media and 5x with PBS. Samples were then either immediately fixed or incubated in fresh media for an additional 24 hours prior to fixation and processing.

TEM imaging shows that Au-MK2i-NPs are visibly clustered at the plasma membrane during uptake in cells fixed immediately after 30 minutes of treatment (**Figure 2.4.a.i. & 2.4.a.ii.**). TEM images evinced structures consistent with macropinocytosis (**Figure 2.4.a.iii & 2.4.a.iv.**), which were not found in untreated or gold only samples (**Figure 2.4.d.i. & 2.4.d.iii.**). Au-MK2i-NPs are also found both contained within vesicular structures (**Figure 2.4.b.**, black arrows) and in the cytosol at 30 minutes (**Figure 2.4.b.ii. & 2.4.b.iv.**, white arrows). At 24 hr. post-treatment, Au-MK2i-NPs are found within the cell both inside vesicular structures consistent with the endo-lysosomal system (**Figure 2.4.c.i.-iii.**, black arrows) and outside

membrane bound vesicles (**Figure 2.4.c.ii-iv.**, white arrows), suggesting endosomal escape and cytosolic MK2i delivery. Although some Au-MK2i-NPs were found to reside within vesicles with clearly visible and intact membranes (**Figure 2.4.c.i.**, black arrows), they were also commonly associated with vesicles with disrupted membranes [i.e., only partial membranes (**Figure 2.4.c.ii.**, black arrows) or fragmented membranes (**Figure 2.4.c.iii.**, all particles)]. These damaged and swollen vesicles found in Au-MK2i-NP treated cells are in clear contrast to untreated or gold only treated control cells (**Figure 2.4.d.i-iv.**). These are the first high-resolution electron micrographs, to our knowledge, that enable visualization of the endosomal disruption activity of the highly-utilized endosomolytic polymer PPAA.

Figure 4a. NP binds to cell membrane, inducing macropinosome formation at t = 30 min.

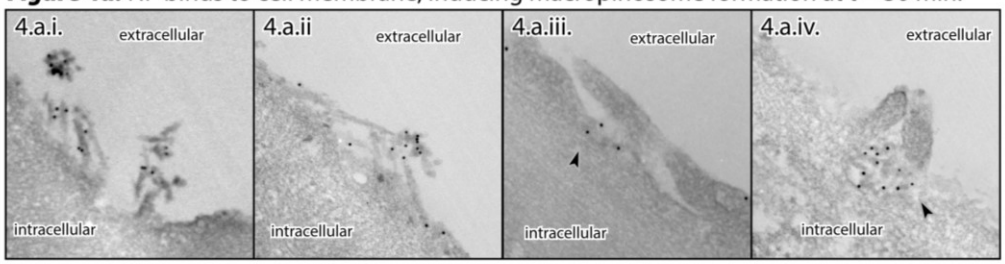

Cells treated 30 minutes with 10 uM Au-MK2i-NP and immediately fixed. **500 nm**

Figure 4b. NP found both inside vesicles and in cytosol near vesicles at t = 30 min.

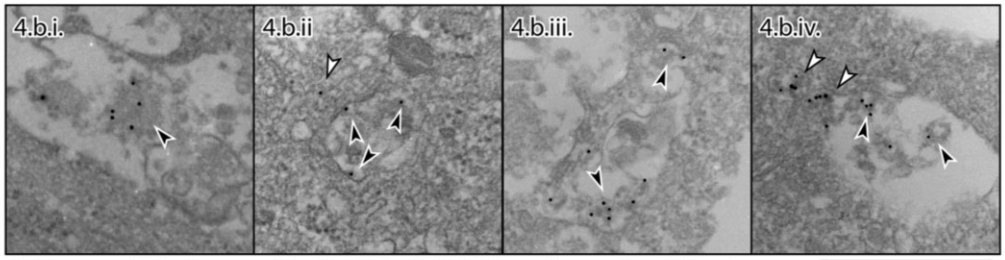

Cells treated 30 minutes with 10 uM Au-MK2i-NP and immediately fixed. **500 nm**

Figure 4c. NP found inside vesicles and in cytosol at t = 24 hr.

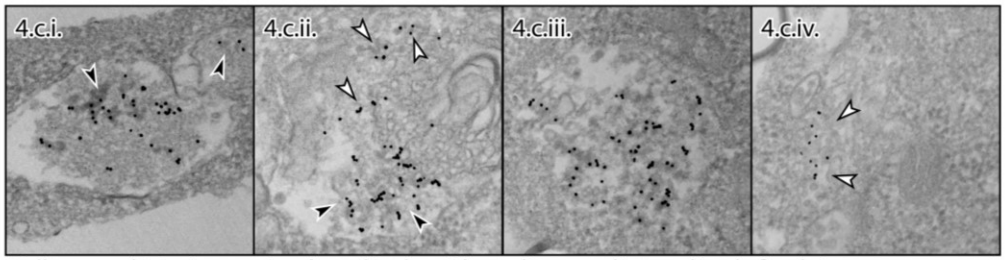

Cells treated 30 minutes, incubated 24 hr with medium, and immediately fixed. **500 nm**

Figure 4d. Untreated control cells or gold only control as marked.

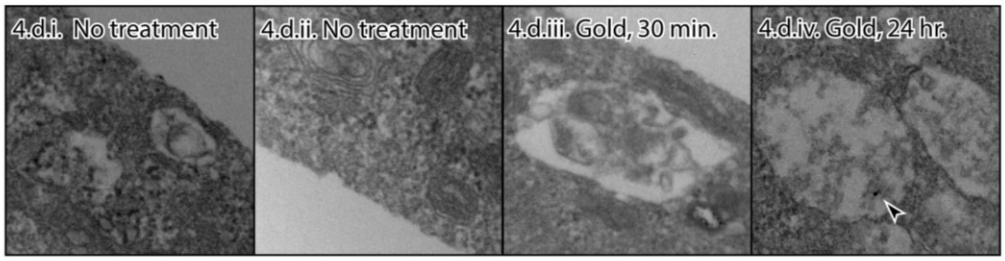

Cells were treated with PBS or dose-matched gold as controls. **500 nm**

Key:
Vesicular
Cytosolic

Figure 2.4. TEM analysis supports MK2i-NP uptake by macropinocytosis and escape from endo-lysosomal vesicles.
(a) Au-MK2i-NP binds to cell membrane, inducing macropinosome formation. (b) Au-MK2i-NP is apparent both inside vesicles and in cytosol near vesicles at t=30 minutes. (c) Au-MK2i-NP are also visualized inside of vesicles and in the cytosol at t=24 hours. (d) Untreated cells and Au-alone treated cells showing lack of membrane binding and low intracellular accumulation.

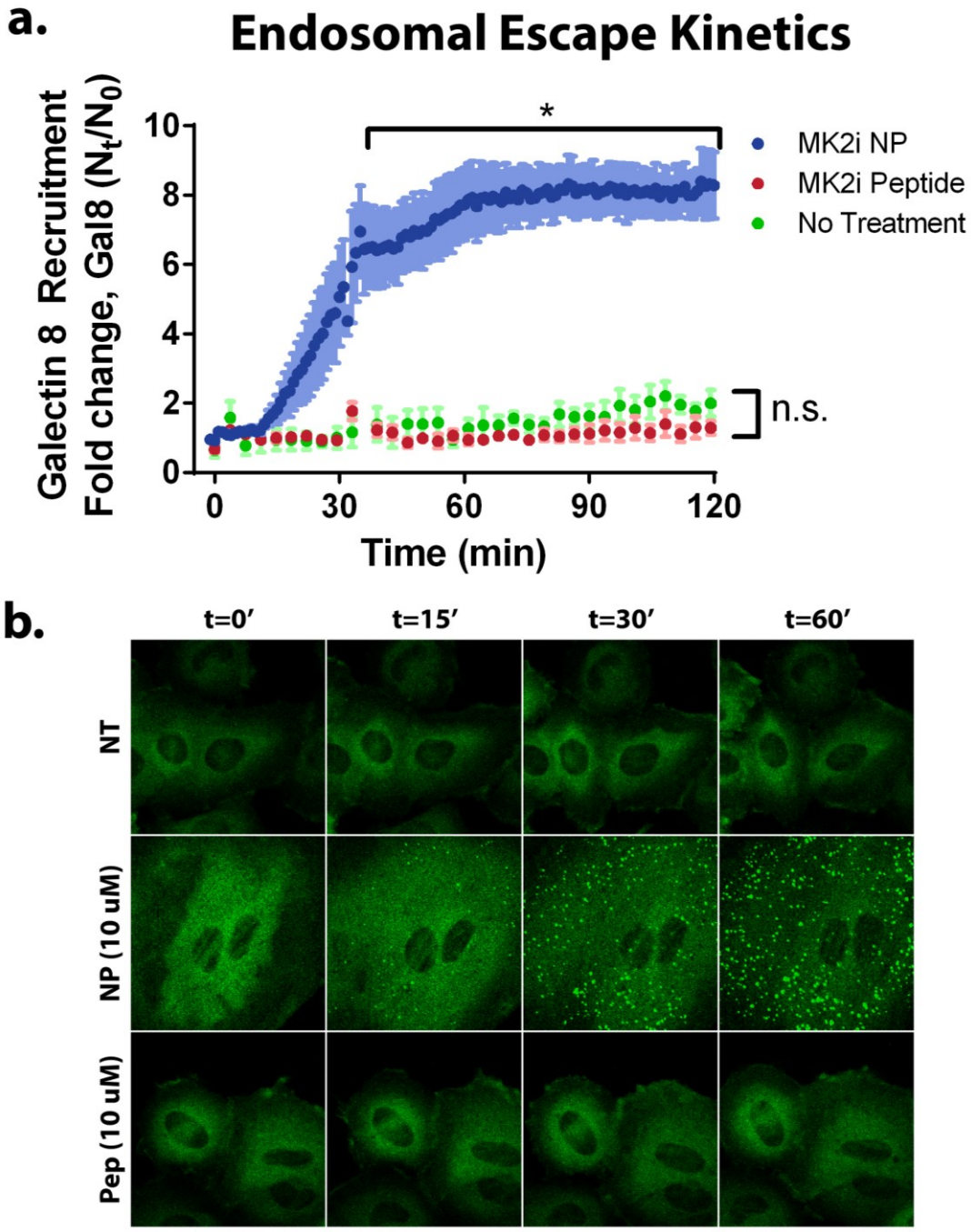

Figure 2.5. MK2i-NP treatment rapidly triggers endosomal disruption as visualized with Galectin 8 recruitment.
(a) Endosomal disruption kinetics are plotted as fold change in gal8 punctation. From top to bottom, blue circles represent 10 μM MK2i-NP, green circles represent no treatment, and red circles indicate 10 μM MK2i. Treatments were removed at t = 30 minutes and replaced with fresh medium. Asterisk (*) indicates $p < 0.05$ for MK2i-NP vs MK2i and NT. (b) Representative images are shown for no treatment, MK2i-NP 10 μM, and MK2i peptide 10 μM at t = 0, 15, 30, and 60 minutes.

2.4.3 Real-time Monitoring of Endosomal Escape

To determine the temporal kinetics of endosomal escape revealed by TEM, a novel live-cell fluorescent imaging methodology based on intracellular localization of galectin-8 (Gal8) was performed to assess endosomal membrane damage during MK2i-NP treatment. Gal8 is a β-galactoside-binding lectin of the galectin family, and is normally localized diffusely throughout the cytosol and secreted, binding to glycans in the extracellular space to influence cell behavior[1]. They also serve as part of the innate immune to sense exposed intracellular glycans[43], which is relevant to the current application in that glycans are naturally located on the external plasma membrane or enclosed within vesicles (e.g., on the luminal surfaces of endosomes, macropinosomes, etc.). When endosomes are disrupted by pathogens (e.g., bacteria)[43] or transfection reagents (e.g., Lipofectamine)[47], Gal8 binds to glycans on the exposed luminal surface of the endosomal membrane and induces macroautophagy (i.e., sequestration in a *de novo* generated double-membraned autophagosome[8] that fuses with lysosomes to facilitate degradation of the autophagosomal contents). In 2015, Wittrup et al.[47] showed that Lipofectamine lipoplexes induce endosomal damage at the Rab 5 to Rab 7 conversion step, at which point, nucleic acids are released into the cytosol. These studies also showed that the transient leakiness of damaged endosomes results in detectible recruitment of galectin-8 due to accessibility to glycans within the endosomal lumen. Based on this method, A7r5 cells were generated that stably express Gal-8-YFP, enabling real time monitoring and quantification of

endosomal disruption in vascular smooth muscle cells **(Figure 2.5a).** Treatment with MK2i-NPs, but not free MK2i peptide, rapidly induced recruitment of Gal8 to intracellular vesicles (bright punctate staining in **Figure 2.5b**), whereas treatment with free MK2i peptide showed no appreciable changes over time. We also located, in MK2i-NP-treated cells, double membrane structures consistent with autophagosomes merging with electron dense vesicles consistent with lysosomes 30 minutes after treatment (**Figure 2.6**).

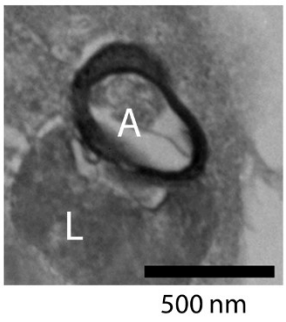

Figure 2.6. TEM shows autophagosome merging with a lysosome.
Time = 30 minutes. L marks electron dense structure consistent with lysosome, A marks a double membrane structure consistent with a damaged vesicle sealed inside an autophagosome μM MK2i peptide.

2.5 Discussion

This work focused on investigating the cellular uptake and intracellular trafficking mechanisms of a novel nano-polyplex formulation for the intracellular delivery of a therapeutic, anti-inflammatory MK2 inhibitory peptide. This MK2i-NP formulation was initially developed to circumvent peptide endo-lysosomal sequestration and degradation to increase the intracellular bioavailability of MK2i in vascular smooth muscle cells, thereby increasing potency and longevity of action as a prophylactic approach to improving the patency of vascular bypass grafts. Serendipitously, formulation into NPs was found to significantly increase MK2i peptide uptake in addition to enabling endosomal escape and increasing intracellular half-life. The clinical translatability of the MK2i-NP formulation was then validated in a pre-clinical animal model of bypass grafting, where treatment with MK2i-NPs was found to significantly enhance

the ability of the MK2i peptide to prevent intimal hyperplasia in vein transplants *in vivo*[18]. Thus, the studies herein were designed to gain mechanistic insight into how NP formulation influences the cellular uptake and intracellular trafficking of the MK2i peptide to realize a more effective peptide-based therapy. By elucidating the mechanism of MK2i-NP uptake and trafficking, we can potentially efficacy so that they can be more broadly applied to improve the intracellular delivery of peptides and other biomacromolecular therapeutics.

Flow-cytometry-based analysis of MK2i-NP uptake verified that NP formulation significantly increased MK2i uptake in A7r5 rat aortic smooth muscle cells 49-fold (**Figure 2.1b**), recapitulating the uptake effects found in primary human coronary artery vascular smooth muscle cells. Confocal microscopy imaging revealed that MK2i-NPs strongly associated with the cellular membrane (**Supplemental Figure 2.S3**), likely due to interactions of the hydrophobic/lipophilic propyl moiety of the PPAA polymer with the hydrophobic tails of phospholipids in the cellular membrane. To understand if this enhanced membrane association influences the mechanism of cellular internalization, uptake studies were performed in conjunction with a library of small molecule inhibitors of various endocytic pathways. Although the MK2i peptide is positively charged, MK2i-NPs have a negative ζ-potential (i.e., surface charge) due to the relative excess of anionic PPAA polymer (charge ratio of the optimized NP formulation is one positively charged peptidic primary amine on the MK2i peptide to 3 negatively charged polymeric carboxylate groups on PPAA). Considering that scavenger receptors are implicated in the uptake of negatively charged, oxidized low-density lipoprotein particles in vascular smooth muscle cells[5,31], we initially hypothesized that scavenger receptors may be responsible for the observed increase in peptide uptake. However, two separate scavenger receptor inhibitors, polyinosinic acid and dextran sulfate, were found to have no

influence on MK2i-NP uptake. In agreement with previous studies[10,22], uptake of the MK2i peptide appeared to be dependent on clathrin- and/or caveolae mediated endocytosis and independent of macropinocytosis. In contrast, MK2i-NP uptake was found to be dependent on both macropinocytosis and clathrin- and/or caveolae mediated endocytosis.

Electron microscopy studies confirmed that macropinocytosis as an underlying mechanism of enhanced uptake of MK2i-NPs. SEM analysis of MK2i-NP treated cells confirm the induction of macropinocytosis as evinced by appearance of membrane ruffling, blebbing, and protrusions that were not present in untreated cells or cells treated with the free MK2i peptide (**Figure 2.2c**). TEM analysis further supported macropinocytosis as a differential mechanism of MK2i-NP uptake. Gold-labeled Au-MK2i-NPs were found to strongly associate with areas of the cell membrane that displayed membrane ruffling, membrane blebbing, and pseudopodia. Furthermore, Au-MK2i-NPs were found within large diameter (i.e., ~500 nm) vesicular compartments consistent with morphology of macropinosomes **(Figure 2.4.b.i-iv., 2.4.c.i-iii.).**

Macropinosomes have been reported to be inherently more leaky than endosomes[27], so we aimed to determine the trafficking and ultimate fate of MK2i-NPs following cellular internalization. Previous studies demonstrated that MK2i-NPs display pH-dependent red blood cell membrane disruption ideally tuned for escape from acidified endo-lysosomal compartments. TEM analysis of Au-MK2i-NP uptake further support that NP formulation enables peptide endosomal escape and cytosolic delivery: TEM images clearly demonstrate Au-MK2i-NPs associated with disrupted intracellular membranes and also show Au-MK2i-NPs in the cytosol of treated cells (i.e., not bound by a plasma membrane) **(Figure 2.4.b.ii, iv; Figure 2.4.c.ii-iv) .** This endosomal escape and cytosolic delivery can be attributed to both the pH-dependent membrane disruptive properties of PPAA and the leakiness of macropinosomes. To further

investigate membrane disruption as the mechanism of cytosolic MK2i delivery, a novel assay utilizing A7r5 smooth muscle cells transfected with a stably integrated, fluorescent Galectin 8 reporter was utilized. In contrast to untreated control cells and cells treated with free MK2i peptide, MK2i-NP cell treatment triggered significant recruitment of Galectin 8 to intracellular vesicles, indicating active membrane disruption. Interestingly, TEM images evinced double membrane autophagosomal structures (**Figure 2.5c**) in Au-MK2i-NP treated cells that were not found in control cells consistent with damaged endosomes' altered trafficking to lysosomes. This result is in agreement with Wittrup et al.'s observations[47] that Lipofectamine lipoplexes traffic to autophagosomes following Gal8 recruitment. In turn, Gal8 recruits NDP52 and LC3 proteins that are responsible for the formation of a secondary containment membrane around the damaged endosome[43,47], which is then rapidly trafficked to terminal lysosomes[4,8,23,40]. Our data further supports the importance of identifying the role autophagosomal encapsulation of damaged endosomes plays in the delivery of biomacromolecular therapeutics and may help to explain the discrepancy between the 49-fold enhancement in uptake paired with the approximately 10-fold enhancement in bioactivity. Autophagosomal escape may represent a viable pathway for further enhancement of intracellular bioavailability of biomacromolecules delivered *via* endosomolytic carriers.

In conclusion, our data demonstrate that formulation of a therapeutic MK2i peptide into a slightly hydrophobic, pH-responsive NPs enhances uptake through enhanced cellular membrane association and macropinocytosis. This enhanced membrane association is hypothesized to be a result of the hydrophobic nature of the PPAA polymer causing interactions with lipids in the cell membrane. Furthermore, the pH-responsive behavior of the PPAA polymer results in pH-triggered endo-lysosomal disruption following cellular internalization, observed by TEM as both

escape and disruption of membrane morphology. The endosomal disruption of MK2i-NP was further supported by Gal8 recruitment and subsequent trafficking into autophagosomes. Therefore, these studies suggest that formulation of MK2i into NPs significantly increases peptide uptake and facilitates endosomal escape by influencing both the mechanism of cellular uptake and intracellular trafficking. Endosomal escape not only prevents endo-lysosomal degradation and/or exocytosis *via* recycling endosomes, but also increases intracellular bioavailability. These studies suggest that macropinocytosis may be a very efficient route of entry for biologic drugs and that macropinosomes can be escaped by endosomolytic carriers. Further, Gal8 recruitment may be a useful assay for identifying critical structure-function relationships between nano-scale drug delivery carriers and bioactivity, and may prove useful in screening the endosomolytic properties of nanoscale drug carriers. We show that endosomolytic carriers still suffer from partial lysosomal entrapment due to autophagosomal encapsulation of damaged endosomes followed by lysosomal trafficking. This result suggests that autophagosomal trafficking and sequestration may be another critical barrier in the delivery of cytosolic therapeutics; inhibiting this process may represent a high potential target for further enhancements to intracellular bioavailability of cytosolic-acting biologic therapeutics.

Finally, further research into the structure-function relationships of peptide nano-polyplexes is warranted. PPAA has been shown to be applicable to multiple peptides[19], though it is unknown whether PPAA alters intracellular trafficking for all biomacromolecular cargo in similar manner. Efficient delivery of protein and peptide drugs to cytosolic targets remains a critical barrier in the clinical translation of cytosol acting peptide drugs. Even the strongest endosomolytic agents are only partially efficient at cytosolic delivery and endosomal escape and may be limited in their delivery efficiency by autophagosome sequestration mechanisms.

2.6 References

1. Barondes, S.H., D.N. Cooper, M.A. Gitt, and H. Leffler. Galectins. Structure and function of a large family of animal lectins. *J. Biol. Chem.* 269:20807–20810, 1994.

2. Behr, J.P. The proton sponge: a trick to enter cells the viruses did not exploit. *CHIMIA International Journal for Chemistry* 51:34–36, 1997.

3. Berguig, G.Y. *et al.* Intracellular delivery and trafficking dynamics of a lymphoma-targeting antibody-polymer conjugate. *Mol. Pharm.* American Chemical Society, 9:3506–3514, 2012.

4. Bernard, A., and D.J. Klionsky. Toward an understanding of autophagosome-lysosome fusion: The unsuspected role of ATG14. *Autophagy* 11:583–584, 2015.

5. Bickel, P.E., and M.W. Freeman. Rabbit aortic smooth muscle cells express inducible macrophage scavenger receptor messenger RNA that is absent from endothelial cells. *J. Clin. Invest.* American Society for Clinical Investigation, 90:1450–1457, 1992.

6. Borsello, T. *et al.* A peptide inhibitor of c-Jun N-terminal kinase protects against excitotoxicity and cerebral ischemia. *Nature Medicine* Nature Publishing Group, 9:1180–1186, 2003.

7. Boussif, O. *et al.* A versatile vector for gene and oligonucleotide transfer into cells in culture and in vivo: polyethylenimine. *PNAS* National Acad Sciences, 92:7297–7301, 1995.

8. Boyle, K.B., and F. Randow. The role of "eat-me" signals and autophagy cargo receptors in innate immunity. *Curr. Opin. Microbiol.* 16:339–348, 2013.

9. Brown, M.S., S.K. Basu, J.R. Falck, Y.K. Ho, and J.L. Goldstein. The scavenger cell pathway for lipoprotein degradation: Specificity of the binding site that mediates the uptake of negatively-charged LDL by macrophages. *Journal of Supramolecular Structure* Alan R.

Liss, Inc, 13:67–81, 1980.

10. Brugnano, J., J. McMasters, and A. Panitch. Characterization of endocytic uptake of MK2-inhibitor peptides. *J. Pept. Sci.* 19:629–638, 2013.

11. Canton, J., D. Neculai, and S. Grinstein. Scavenger receptors in homeostasis and immunity. *Nat Rev Immunol* 13:621–634, 2013.

12. Convertine, A.J., D.S.W. Benoit, C.L. Duvall, A.S. Hoffman, and P.S. Stayton. Development of a novel endosomolytic diblock copolymer for siRNA delivery. *Journal of Controlled Release* 133:221–229, 2009.

13. Convertine, A.J., D.S.W. Benoit, C.L. Duvall, A.S. Hoffman, and P.S. Stayton. Development of a novel endosomolytic diblock copolymer for siRNA delivery. *J Control Release* 133:221–229, 2009.

14. Copolovici, D.M., K. Langel, E. Eriste, and Ü. Langel. Cell-penetrating peptides: design, synthesis, and applications. *ACS Nano* 8:1972–1994, 2014.

15. De Smedt, S.C., J. Demeester, and W.E. Hennink. Cationic Polymer Based Gene Delivery Systems - Springer. *Pharmaceutical Research* 17:113–126, 2000.

16. Deshayes, S., M.C. Morris, G. Divita, and F. Heitz. Cell-penetrating peptides: tools for intracellular delivery of therapeutics. *CMLS, Cell. Mol. Life Sci.* Birkhäuser-Verlag, 62:1839–1849, 2005.

17. Duvall, C.L., A.J. Convertine, D.S.W. Benoit, A.S. Hoffman, and P.S. Stayton. Intracellular delivery of a proapoptotic peptide *via* conjugation to a RAFT synthesized endosomolytic polymer. *Mol. Pharm.* American Chemical Society, 7:468–476, 2010.

18. Evans, B.C. *et al.* MK2 inhibitory peptide delivered in nanopolyplexes prevents vascular graft intimal hyperplasia. *Sci Transl Med* 7:291ra95, 2015.

19. Evans, B.C., K.M. Hocking, K.V. Kilchrist, E.S. Wise, C.M. Brophy, and C.L. Duvall. Endosomolytic Nano-Polyplex Platform Technology for Cytosolic Peptide Delivery To Inhibit Pathological Vasoconstriction. *ACS Nano* 9:5893–5907, 2015.

20. Falcone, S., E. Cocucci, P. Podini, T. Kirchhausen, E. Clementi, and J. Meldolesi. Macropinocytosis: regulated coordination of endocytic and exocytic membrane traffic events. *J Cell Sci* The Company of Biologists Ltd, 119:4758–4769, 2006.

21. Felgner, J.H. *et al.* Enhanced gene delivery and mechanism studies with a novel series of cationic lipid formulations. *J. Biol. Chem.* American Society for Biochemistry and Molecular Biology, 269:2550–2561, 1994.

22. Flynn, C.R. *et al.* Internalization and intracellular trafficking of a PTD-conjugated anti-fibrotic peptide, AZX100, in human dermal keloid fibroblasts. *J Pharm Sci* 99:3100–3121, 2010.

23. Furuta, N., and A. Amano. SNARE mediates autophagosome–lysosome fusion. *Journal of Oral Biosciences* 54:83–85, 2012.

24. Gump, J.M., and S.F. Dowdy. TAT transduction: the molecular mechanism and therapeutic prospects. *Trends in Molecular Medicine* Elsevier, 13:443–448, 2007.

25. Hayess, K., and R. Benndorf. Effect of protein kinase inhibitors on activity of mammalian small heat-shock protein (HSP25) kinase. *Biochemical Pharmacology* 53:1239–1247, 1997.

26. Kaplan, I.M., J.S. Wadia, and S.F. Dowdy. Cationic TAT peptide transduction domain enters cells by macropinocytosis. *Journal of Controlled Release* 102:247–253, 2005.

27. Khalil, I.A., K. Kogure, H. Akita, and H. Harashima. Uptake pathways and subsequent intracellular trafficking in nonviral gene delivery. *Pharmacol Rev* American Society for

Pharmacology and Experimental Therapeutics, 58:32–45, 2006.

28. Knighton, D.R., J.H. Zheng, L.F. Ten Eyck, N.H. Xuong, S.S. Taylor, and J.M. Sowadski. Structure of a peptide inhibitor bound to the catalytic subunit of cyclic adenosine monophosphate-dependent protein kinase. *Science* American Association for the Advancement of Science, 253:414–420, 1991.

29. Koivusalo, M. *et al.* Amiloride inhibits macropinocytosis by lowering submembranous pH and preventing Rac1 and Cdc42 signaling. *J Cell Biol* Rockefeller Univ Press, 188:547–563, 2010.

30. Kotlyarov, A. *et al.* Distinct Cellular Functions of MK2. *Molecular and Cellular Biology* American Society for Microbiology (ASM), 22:4827–4835, 2002.

31. Li, H., M. Freeman, and P. Libby. Regulation of smooth muscle cell scavenger receptor expression in vivo by atherogenic diets and in vitro by cytokines. *Journal of Clinical Investigation*, 1995. Available from: http://www.ncbi.nlm.nih.gov/pmc/articles/PMC295387/.

32. Lopes, L.B. *et al.* Cell Permeant Peptide Analogues of the Small Heat Shock Protein, HSP20, Reduce TGF-β1-Induced CTGF Expression in Keloid Fibroblasts. *Journal of Investigative Dermatology* 129:590–598, 2008. Available from: http://www.nature.com/doifinder/10.1038/jid.2008.264.

33. Lopes, L.B., C. Flynn, P. Komalavilas, A. Panitch, C.M. Brophy, and B.L. Seal. Inhibition of HSP27 phosphorylation by a cell-permeant MAPKAP Kinase 2 inhibitor. *Biochemical and Biophysical Research Communications* 382:535–539, 2009.

34. Macia, E., M. Ehrlich, R. Massol, E. Boucrot, C. Brunner, and T. Kirchhausen. Dynasore, a cell-permeable inhibitor of dynamin. *Dev. Cell* 10:839–850, 2006.

35. Meng, W. *et al.* Structure of Mitogen-activated Protein Kinase-activated Protein (MAPKAP) Kinase 2 Suggests a Bifunctional Switch That Couples Kinase Activation with Nuclear Export. *J. Biol. Chem.* American Society for Biochemistry and Molecular Biology, 277:37401–37405, 2002.

36. Mercer, J., and A. Helenius. Virus entry by macropinocytosis. *Nat. Cell Biol.* 11:510–520, 2009.

37. Nakase, I. *et al.* Cellular uptake of arginine-rich peptides: roles for macropinocytosis and actin rearrangement. *Mol. Ther.* 10:1011–1022, 2004.

38. Nakase, I., N.B. Kobayashi, T. Takatani-Nakase, and T. Yoshida. Active macropinocytosis induction by stimulation of epidermal growth factor receptor and oncogenic Ras expression potentiates cellular uptake efficacy of exosomes. *Scientific Reports* Nature Publishing Group, 5:10300, 2015.

39. Richard, J.P. *et al.* Cell-penetrating peptides. A reevaluation of the mechanism of cellular uptake. *J. Biol. Chem.* American Society for Biochemistry and Molecular Biology, 278:585–590, 2003.

40. Shibutani, S.T., and T. Yoshimori. Autophagosome formation in response to intracellular bacterial invasion. *Cell. Microbiol.* 16:1619–1626, 2014.

41. Sorkin, A., and M. von Zastrow. Signal transduction and endocytosis: close encounters of many kinds. *Nat Rev Mol Cell Biol* 3:600–614, 2002.

42. Stewart, S.A. *et al.* Lentivirus-delivered stable gene silencing by RNAi in primary cells. *RNA* 9:493–501, 2003.

43. Thurston, T.L.M., M.P. Wandel, N. von Muhlinen, A. Foeglein, and F. Randow. Galectin 8 targets damaged vesicles for autophagy to defend cells against bacterial invasion. *Nature*

482:414–418, 2012.

44. Varkouhi, A.K., M. Scholte, G. Storm, and H.J. Haisma. Endosomal escape pathways for delivery of biologicals. *J Control Release* 151:220–228, 2011.

45. Verdine, G.L., and G.J. Hilinski. Stapled Peptides for Intracellular Drug Targets. In: Protein Engineering for Therapeutics, Part B Elsevier, 2012, pp. 3–33.

46. Verma, P., A.G. Ostermeyer-Fay, and D.A. Brown. Caveolin-1 induces formation of membrane tubules that sense actomyosin tension and are inhibited by polymerase I and transcript release factor/cavin-1. *Mol. Biol. Cell* 21:2226–2240, 2010.

47. Wittrup, A. *et al.* Visualizing lipid-formulated siRNA release from endosomes and target gene knockdown. *Nat. Biotechnol.* 33:870–876, 2015.

48. Yamaguchi, H., Y. Takeo, S. Yoshida, Z. Kouchi, Y. Nakamura, and K. Fukami. Lipid rafts and caveolin-1 are required for invadopodia formation and extracellular matrix degradation by human breast cancer cells. *Cancer Res.* American Association for Cancer Research, 69:8594–8602, 2009.

CHAPTER 3

GAL8 VISUALIZATION OF ENDOSOME DISRUPTION PREDICTS CARRIER-MEDIATED BIOLOGIC DRUG INTRACELLULAR BIOAVAILABILITY

Adapted from

"Gal8 Visualization of Endosome Disruption Predicts Carrier-Mediated Biologic Drug Intracellular Bioavailability,"

published in ACS Nano 10 January 2019

by

Kameron V. Kilchrist, Somtochukwu C. Dimobi, Meredith A. Jackson, Brian C. Evans, Thomas A. Werfel, Eric A. Dailing, Sean K. Bedingfield, Isom B. Kelly, and Craig L. Duvall.

doi.org/10.1021/acsnano.8b05482

Graphical Abstract:

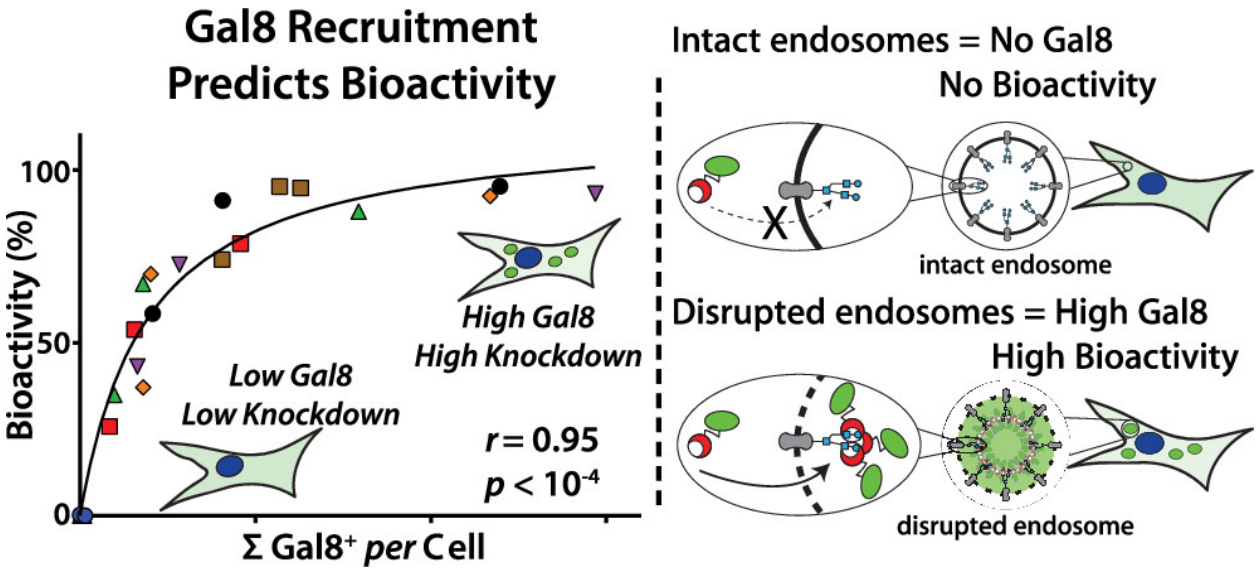

As the previous chapter was prepared for publication, we recognized the untapped potential of the Gal8-YFP reporter for use as a high throughput screening assay to develop polymers and lipids for endosome disrupting drug delivery systems. Several groups had begun using high throughput chemistry and formulation efforts to develop novel ionizable lipids and polymers, which invariably were designed for use as plasmid DNA, siRNA, ASO, or mRNA delivery vehicles, as these all have facile high throughput bioactivity readouts using either luciferase / GFP delivery (plasmid and mRNA delivery) or luciferase / GFP knockdown (siRNA and ASO). However, directly assessing the bioactivity of other cargoes, like peptides and proteins, is less easy to measure directly in a high throughput paradigm and was a significant frustration in the development of successors to MK2i-NP. We recognized the potential for Gal8-YFP tracking as an endpoint assay that measures a proxy of bioactivity to rationally down-select large formulation libraries, and thus set out to validate it as predictive of intracellular bioactivity. As a test case, we synthesized a library of polymers which were rationally designed to have a variety of bioactivities. We show that Gal8-YFP tracking is superior to other methods of predicting successful polymers to deliver siRNA, with Gal8 recruitment having the highest correlation to gene knockdown of any technique tested.

3.1 Abstract

Endo-lysosome entrapment is one of the key barriers to therapeutic use of biologic drugs that act intracellularly. Screening of prospective nanoscale endosome-disrupting delivery technologies is currently limited by methods that are indirect and cumbersome. Here we statistically validate Galectin 8 (Gal8) intracellular tracking as a superior approach that is direct, quantitative, and predictive of therapeutic cargo intracellular bioactivity *in vitro* high throughput

screening and *in vivo* validation. Gal8 is a cytosolically-dispersed protein that, when endosomes are disrupted, redistributes by binding to glycosylation moieties selectively located on the inner face of endosomal membranes. The quantitative redistribution of a Gal8 fluorescent fusion protein from the cytosol into endosomes is demonstrated as a real-time, live cell assessment of endosomal integrity that does not require labeling or modification of either the carrier or biologic drug and that allows quantitative distinction between closely-related, endosome-disruptive drug carriers. Through screening two families of siRNA polymeric carrier compositions at varying dosages, we show that Gal8 endosomal recruitment correlates strongly ($r = 0.95$, $p < 10^{-4}$) with intracellular siRNA bioactivity. Through this screen, we gathered insights into how composition and molecular weight affect endosome disruption activity of poly[(ethylene glycol)-b-[(2-(dimethylamino)ethyl methacrylate)-co-(butyl methacrylate)]] [PEG-(DMAEMA-co-BMA)] siRNA delivery systems. Additional studies showed that Gal8 recruitment predicts intracellular bioactivity better than current standard methods such as Lysotracker colocalization ($r = 0.35$, not significant), pH dependent hemolysis (not significant), or cellular uptake ($r = 0.73$, $p < 10^{-3}$). Importantly, Gal8 recruitment method is also amenable to fully objective high throughput screening using automated image acquisition and quantitative image analysis, with a robust estimated Z' of 0.6 (whereas assays with $Z' > 0$ have high throughput screening utility). Finally, we also provide measurements of *in vivo* endosomal disruption based on Gal8 visualization ($p < 0.03$) of a nanocarrier formulation confirmed to produce significant cytosolic delivery and bioactivity of siRNA within tumors ($p < 0.02$). In sum, this report establishes the utility of Gal8 subcellular tracking for rapid optimization and high throughput screening of endosome disruption potency of intracellular delivery technologies.

3.2 Introduction

Intracellular delivery of biomacromolecules—proteins, peptides, and nucleic acids like mRNA, antisense oligodeoxynucleotides (ASO/ODN), miRNA, and siRNA—has high but relatively unrealized therapeutic potential. With the exception of vaccines, there have been only six U.S. FDA approved biomacromolecular drugs with intracellular mechanisms of action to date—five antisense or splice modifying ODNs[1,2] and one siRNA lipid nanoparticle formulation[3]. Beyond the systemic pharmacokinetic barriers facing biomacromolecular drugs,[4] the primary barrier to intracellular bioavailability is endo-lysosomal sequestration and degradation following endocytosis.[5,6] Thus, efficient endosome-disrupting drug carrier formulations, often leveraging the progressive acidification that occurs as endosomes mature, are highly sought as research tools and for enabling clinically-successful intracellular-acting biomacromolecular therapeutics.[7] Most work in this field leverages lipids, polymers, viruses, cell penetrating peptides, or photothermal energy to achieve endosome disruption through pH sensitive conformation/solubility changes, counterion induced osmotic swelling, thermally induced endosomal disruption, or pH-triggered unmasking of hydrophobic elements that disrupt endosomal lipid bilayer membranes.[8–13]

Despite numerous papers optimizing carrier mediated drug delivery, methods to directly measure endosomal disruption are elusive. Quantitative Gal8 tracking in live cells overcomes multiple shortcomings of alternate experimental methods. This work quantitatively compares the measurement of Gal8 recruitment to other commonly used assays and establishes that it is sensitive and high throughput. Combinatorial polymer and lipid chemistry is commonly used to create large libraries, and this assay is amenable to adoption as a component of the high throughput screening pipeline for parallel measurement of the endosome disruptive potency of

candidate formulations.

Although endosomal escape efficiency is a key characteristic of intracellular carriers, it is a relatively rare event[14,15] that is difficult to directly measure, especially in a high throughput capacity. The most commonly used approaches do not measure endosomal membrane integrity, instead relying on tracking pH-sensitive fluorophores attached to the biologic cargo or imaging colocalization of fluorescently labeled cargo with acidotropic dyes (*e.g.*, Lysotracker) that accumulate in endo-lysosomal compartments.[16–20] One limitation of these approaches is that sensitivity limitations of microscopy often require supra-therapeutic dosing for robust colocalization imaging analyses.[21] However, dependency on fluorophores (often bulky, hydrophobic organic dyes) is, in general, not ideal because they can alter cellular uptake and intracellular trafficking of the cargo,[22] are subject to photo-bleaching, can be quenched when densely packed into a carrier system,[23] and are susceptible to pH- and solvation-dependent fluctuations in quantum efficiency.[22,24] Furthermore, many pH-responsive, endosomolytic carriers purposefully incorporate basic moieties that buffer pH in the endo-lysosomal environments.[18,25,26] With these "proton sponge" formulations, carrier-mediated pH buffering can potentially alter signal from pH-sensitive and acidotropic fluorophores independent of whether the endosome has been physically disrupted. The use of a fluid-phase tracer (*e.g.*, fluorescent dextrans) can also be used to track endosomal disruption, however, endocytosis and trafficking of these tracer macromolecules may not match the biologic drug in question; for instance, it has been noted that there are differences between cytosolic release of calcein, a small fluid phase tracer and fluorescent oligonucleotides loaded into polyplexes which traffic to the nucleus.[15] Rather than measuring lack of colocalization with endosomes, another relevant approach for some classes of cargo is to measure colocalization with the ultimately targeted intracellular

compartment, for example the nucleus for plasmids or ODNs[27]. Further, these trafficking studies are ideally performed on live cells, because fixation artefacts for biologic drugs like peptides and nucleic acids can be misleading.[28] Additionally, fluorescent microscopists are often biased towards choosing exposure and other image settings that detect the brightest areas of a cell (endosomes) which may obscure low-level cytosolic fluorescence. A pivotal study by Gilleron *et al.* showed that as little as 2% of siRNA cargo escaping endosomes can cause maximal gene silencing—therefore functionally significant escape may be associated with cytosolic concentrations of molecules below the lower limit of typical fluorescent microscopic detection, especially under settings optimized for visualization of cargo-packed endo-lysosomal vesicles.[14]

The two methods that provide robust confirmation of endosomal disruption are transmission electron microscopy (TEM) and cellular fractionation, but these methods are not amenable to rapid, high-throughput analysis. TEM facilitated by electron dense labels (*e.g.*, gold) provides a robust way to assess endosomal membrane integrity and escape, but TEM samples preparation is extremely time consuming, cannot be obtained on live cells, provides only a very small field of view *per* imaging field, and can be difficult to interpret for non-experts.[14,29] Cell fractionation can be performed in two formats. In a semi-permeabilization method, carefully timed weak detergents are applied to lyse the plasma membrane but not endo-lysosomal membranes. Cytosolic components are extracted, and the cytosolic drug is compared to the organelle-bound drug.[30,31] In the mechanical separation method, cells are mechanically homogenized and separated by gradient ultracentrifugation, and the drug is quantified in each fraction.[32,33] Both types of cell fractionation require experimental validation to identify and assess purity of extracted fractions, typically by Western blot, and require modification of the drug with radiolabels or fluorophores for quantification purposes. Both TEM and cellular

fractionation can provide robust readouts but are labor intensive and low throughput.[29,30]

To develop a live-cell, high-throughput-amenable endosomal escape screening assay that does not require chemical modification of the carrier or cargo, we sought to develop and validate Galectin-8 (Gal8) recruitment for direct visualization of endosomal disruption by drug carriers. Gal8 is a β-galactoside carbohydrate-binding protein described by Hadari *et al.* and expressed in a variety of tissues.[34] Thurston *et al.* subsequently discovered the role of Gal8 in innate immunity, where it functions to detect disrupted endosomes due to high affinity binding with glycans selectively found on the inner leaflet of endosomal membranes.[35] More recently, groups have used Galectin reporters and high speed microscopy to track adenoviral entry into cells, showing that viral entry to cytosol is preceded by Galectin-3 redistribution.[36] Wittrup *et al.* reported that the appearance of Gal8 positive spots temporally coincides with the cytosolic delivery of fluorescently labeled siRNA from lipid nanoparticles,[37] and we reported the use of Gal8 recruitment to quantitatively assess kinetics of polymer-mediated endosome disruption for intracellular peptide delivery.[29]

Here, we focused on establishing quantitative correlations between carrier-mediated Gal8 recruitment levels and intracellular biologic cargo bioavailability and activity. Establishing the range and nature of this correlation is vital for verifying whether Gal8 recruitment imaging can be utilized to predict intracellular bioavailability of carrier formulations. Similar high-throughput and automated microscopy methods are already used in high throughput screening of compounds, genes, RNAi, and CRISPR mediated gene knockouts.[38–42] Establishing a suitable assay for assessing endosome disruption could become a powerful component of the pipeline for screening and understanding the structure-function properties among combinatorial chemistry-derived libraries of endosome-disrupting polymers and lipids, a highly popular carrier

optimization approach.[43–46] Herein we screen level of Gal8 recruitment for two series of siRNA formulations (a composition series and a molecular weight [MW] series) of rationally designed polymers applied at different doses. This small library contains varied formulations with a range from negligible to very powerful pH-dependent endosome disruptive activity. This study design allows us to both validate the correlation between Gal8 imaging and intracellular cargo bioavailability (based on a luciferase knockdown readout) and also provides insights on how composition and molecular weight (MW) impact endosome disruption for our library. We also seek to compare the predictive power of the Gal8 recruitment imaging as a measure of intracellular bioavailability to other standard methods such as pH-dependent hemolysis profiling, Lysotracker colocalization analysis, and measurements of total cellular internalization. Finally, we also provide a proof of concept study for application of Gal8 recruitment imaging to visualize carrier-mediated endosome escape *in vivo* in an orthotopic breast tumor model. Collectively, these experiments and statistical analysis are designed to validate the use of Gal8 recruitment as a platform to rapidly screen and optimize intracellular drug delivery systems.

3.3 Results and Discussion

3.3.1 Polymer Library Synthesis and Chemical Characterization

To validate Gal8 recruitment as a predictor of intracellular bioavailability, we synthesized two series of polymers of varied composition and molecular weight to develop a library with widely varied endosome disruption potency. Reversible addition-fragmentation chain transfer (RAFT) was used to polymerize two series of diblock poly[(ethylene glycol)-b-[(2-(dimethylamino)ethyl methacrylate)-co-(butyl methacrylate)]] [PEG-(DMAEMA-co-BMA)] polymers (**Figure 3.S1**). These polymers (general structure shown in **Figure 3.1A**) are

comprised of a constant 5000 g/mol PEG nanopolyplex (NP) corona-forming block and second NP core-forming block of copolymerized DMAEMA (siRNA complexing, pH-responsive, and cationic) and BMA (core-stabilizing, hydrophobic, membrane interactive). This series of polymers extends recent work looking at siRNA NPs (si-NPs) with balanced cationic and hydrophobic core composition[20,43,47–49] and allows us to systematically examine the functional significance of the p(DMAEMA-co-BMA) block molecular weight, which our group has not previously studied.

The first set of polymers with varied p(DMAEMA-co-BMA) block composition was designed to investigate the effects of the ratio of hydrophobe to cation on endosomal escape (**Figure 3.1B** & **Table 3.1**). These polymers consisted of constant si-NP corona-forming block (5000 g/mol PEG) and constant si-NP core-forming block molecular weight (average of 22 000 g/mol) but varied mole percentages (mol %) of hydrophobic BMA and cationic DMAEMA monomers ranging from 0-75 mol % BMA (**Table 3.1**). The second set of polymers was synthesized with a constant ratio of DMAEMA to BMA (50:50), but with varied total molecular weight of the p(DMAEMA-co-BMA) block (**Figure 3.1C & Table 3.2**). The molecular weight (MW) library consisted of seven polymers synthesized from an equimolar feed ratio of BMA and DMAEMA with total PEG-(DMAEMA-co-BMA) diblock polymer molecular weights ranging from 16,300 g/mol to 52,500 g/mol, named 50B-S, 50B-M, 50B-L, 50B-XL, 50B-2XL, 50B-3XL, and 50B-4XL. As a result of the RAFT controlled free radical polymerization method, all resultant polymers have low polydispersity indices and controlled molecular weights as measured by gel permeation chromatography (**Figure 3.1D & 3.1E**), with expected compositions as measured by ^{1}H-NMR (**Table 3.1 & 3.2**).

Table 3.1: Polymer Characteristics, Composition Library

Name	Diblock MW (NMR)*	Units DMAEMA	Units BMA	DMAEMA Content (%)	BMA Content (%)
0B	28 600	150	0	100.0	0.0
25B	29 000	118	38	75.6	24.4
40B	28 300	93	61	60.4	39.6
50B	26 100	71	70	50.4	49.6
60B	26 500	60	85	41.1	58.9
75B	24 400	34	99	25.4	74.6

* Diblock MW refers to number average total polymer molecular weight (M_n), including 5000 g/mol PEG “corona” block, in addition to the “core” p(DMAEMA-co-BMA) block.

To elucidate the relative effects of polymer composition on pH-dependent behavior, the logarithmic acid dissociation constant (pK_a) was measured for all polymers *via* acid-base titration (**Figure 3.1F & 3.1G**). Composition had a strong effect on pK_a, with increasing hydrophobic BMA mol% reducing the pK_a of the protonatable amines on DMAEMA by 18.9×10^{-3} units *per* additional percent BMA (**Figure 3.1F**). In the MW library, core block molecular weight had only a modest effect on pK_a, with increasing molecular weights decreasing the pK_a by 9.6×10^{-3} units *per* 10^3 g/mol (**Figure 3.1G**).

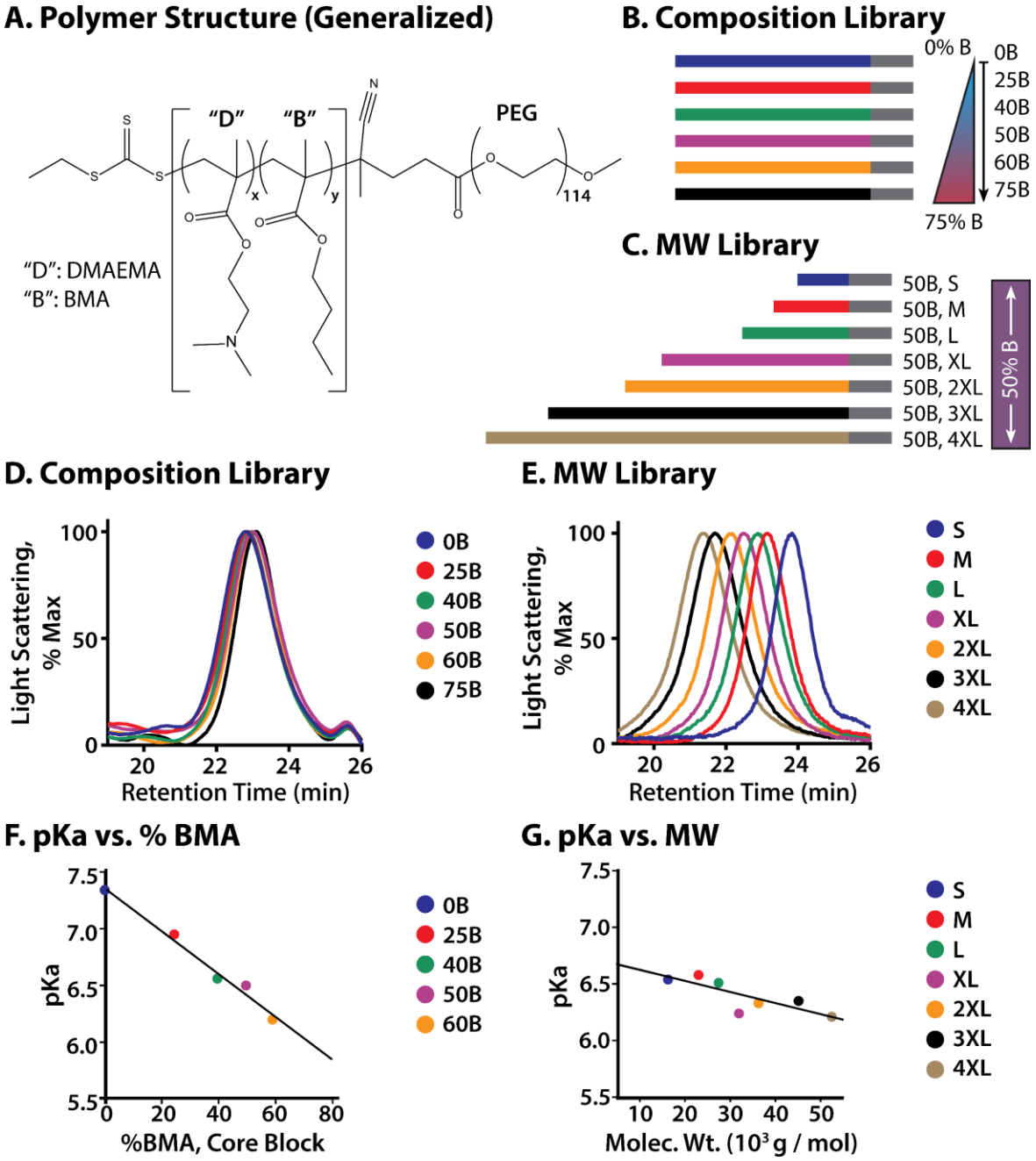

Figure 3.1. Polymer library construction and characterization

(A) Generalized structure for PEG-b-(DMAEMA-co-BMA) polymers (B) The composition library consists of six polymers, ranging from 0% BMA to 75% BMA. Each polymer comprises a 5000 g/mol PEG block and a second random copolymer block with an average MW of approximately 22 000 g/mol. (C) The MW library consists of seven polymers. Each contains a 5000 g/mol PEG block and a second random copolymer block comprising an approximately 50:50 ratio of DMAEMA to BMA monomers and with MW ranging from 11 300 to 47 500 g/mol. (D) Gel permeation chromatography traces show that all polymers in the composition library have well controlled polydispersity and approximately equivalent MW. (E) Gel permeation chromatography traces show that the MW library has well controlled polydispersity and contains a wide range of MW values. (F) Plot of log acid dissociation constant (pK_a) shows that composition significantly impacts pK_a; 75B is omitted due to insolubility under assay conditions; line of best fit: $pK_a = 7.36 - 0.019\ x$ [x expressed in % BMA] (G) Plot of log acid dissociation constant (pK_a) shows that MW has only a modest effect on pK_a; line of best fit: $pK_a = 6.71 - (9.6\times10^{-6})\ x$ [x expressed in g/mol]

3.3.2 Composition Library Cytotoxicity and Gene Silencing Bioactivity

The composition polymer library was screened for cytotoxicity and model gene knockdown in MDA-MB-231 cells that stably expressed firefly luciferase under a constitutive promoter. The successful delivery of siRNA targeting luciferase reduces bioluminescence of luciferin treated cells, and data are normalized to bioluminescence of cells treated with dose-matched formulations loaded with a negative control, nontargeting siRNA. The 25B and 40B polymers formulated into si-NPs loaded with negative control nucleic acids were both significantly cytotoxic, while other compositions did not create cytotoxicity (**Figure 3.2A**). This is consistent with pH-dependent hemolysis data shown subsequently in this report that polymers that are membrane disruptive at physiologic pH are generally cytotoxic. Without sufficient hydrophobicity to drive NP assembly and stability, the hydrophobic BMA containing block becomes exposed to and disrupts outer cell membranes. The si-NPs should be finely tuned to become destabilized and expose the core block only under low pH conditions in the endosomal environmental in order to avoid nonspecific cell-membrane-disruption-mediated cytotoxicity. In other words, the lower %BMA containing polymers are sufficiently hydrophobic to interact with and disrupt lipid bilayer membranes but contain insufficient hydrophobic content to stably assemble (and block DMAMA-co-BMA block outer cell membrane interactions) at physiologic, extracellular pH.

In luciferase model gene knockdown studies, 25B, 40B, and 50B polymers showed significant gene silencing activity using a 100 nM siRNA dose (**Figure 3.2B**). This shows that 50B, containing equimolar cationic DMAEMA and hydrophobic BMA, is the only polymer of this library that is nontoxic and bioactive, confirming earlier studies.[20] We carried forward the nontoxic formulations (0B, 50B, 60B, 75B) into Gal8 recruitment experiments and hypothesized

that, because it showed potent gene silencing, the 50B formulation would show the greatest Gal8 recruitment, as measured qualitatively by the appearance of punctate fluorescent spots (**Figure 3.2C**). These initial experiments had nearly binary results. No Gal8 recruitment was observed for 0B or 75B while a minimal level of Gal8 recruitment was seen for 60B. Robust Gal8 recruitment, visualized as disappearance of diffuse cellular fluorescence and appearance of bright, punctate fluorescent spots was observed for 50B (**Figure 3.2D**). These initial experiments validated 50B as the best composition for the basis of a second library with varied molecular weight, due to its combination of minimal toxicity and efficient siRNA delivery which correlated with gene knockdown data. The desirable results produced using polymers with an equally balanced ratio of DMAEMA to BMA are consistent with several prior *in vitro* and *in vivo* experiments.[20,47–49]

3.3.3 MW Library Cytotoxicity and Gene Silencing Bioactivity

We next sought to screen a broader series of 50B polymers with varied p(DMAEMA-co-BMA) block molecular weight as our previous, undocumented observations had suggested that molecular weight of this block is an important driver of intracellular delivery, but this variable has not been carefully studied. Therefore, we synthesized a well-defined library of 50B polymers over a broad molecular weight range (**Table 2**) with the intention of yielding a series of NP formulations with varied levels of activity that would enable a robust Gal8 recruitment *versus* bioactivity correlation analyses. We characterized this polymer library for toxicity at a range of siRNA doses using the highly sensitive CellTiter Glo assay. It was found that no polymers were toxic at the lowest dose of 12.5 nM siRNA, while there was minor but statistically significant cytotoxicity at the highest polymer doses for the two largest MW p(DMAEMA-co-BMA) core

blocks (**Figure 3.S2**). Two polymers showed statistically significant toxicity; 50B-3XL exhibited 85% viability at 50 nM siRNA, and 50B-4XL exhibited 76% and 86% viability at 50 nM and 25 nM siRNA respectively.

We then characterized this polymer library for luciferase knockdown activity relative to scrambled controls in luciferase expressing MDA-MB-231 cells. All polymers except 50B-S showed statistically significant gene silencing (**Figure 3.3A**). Because we had observed that the knockdown effect was saturated for several polymers at the 50 nM dose, we extended this study to assess lower doses. At the lowest dose of 12.5 nM, we could more sensitively detect the correlation between knockdown activity and molecular weight, with the largest molecular weight 50B-4XL formulation producing 74% reduction in luciferase activity at this relatively low dose. These data were statistically significant for polymer molecular weight, dose, and interaction thereof when tested by 2-way ANOVA ($p < 10^{-4}$, all), with polymer molecular weight accounting for 69% of statistical variation. These data confirm that the MW polymer library provides a solid foundation for the correlation of endosomal escape and bioactivity across a series of polymers with structural similarity but varied levels of bioactive cargo delivery.

Table 3.2: Polymer Characteristics, 50B MW Library

Name	Diblock MW (NMR)*	Units DMAEMA	Units BMA	DMAEMA Content (%)	BMA Content (%)
50B S	16 300	39	36	52.0	48.0
50B M	23 000	63	57	52.5	47.5
50B L	27 500	75	75	50.0	50.0
50B XL	31 900	90	90	50.0	50.0
50B 2XL	36 300	105	104	50.2	49.8
50B 3XL	45 200	137	131	51.1	48.9
50B 4XL	52 500	160	157	50.5	49.5

* Diblock MW refers to number average total polymer molecular weight (M_n), including 5000 g/mol PEG “corona” block, in addition to the “core” p(DMAEMA-co-BMA) block.

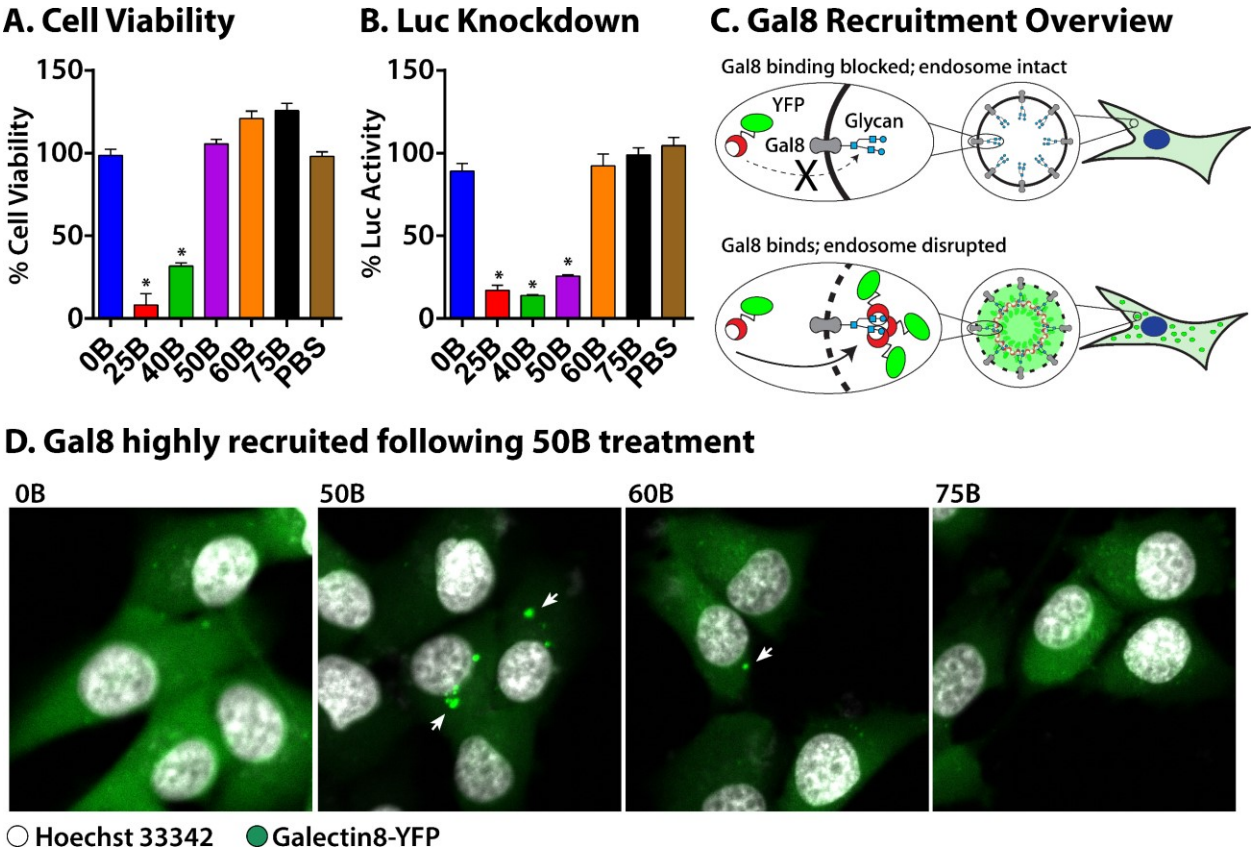

Figure 3.2. Visualization of Gal8 recruitment correlates with the most bioactive (50B) polymeric carrier composition.
(A) Cytotoxicity of formulations loaded with a negative control siRNA (100 nM siRNA). Viability levels were normalized to PBS treated cells; 25B and 40B caused statistically significant cytotoxicity. Overall $p < 0.001$ by ANOVA; *: significant toxicity by Dunnett's post hoc testing vs. PBS.
(B) Bioactivity based on silencing of luciferase activity (luciferase signal in cells treated with 100 nM luciferase siRNA normalized to cells treated with negative control siRNA with the same formulation. Overall $p < 0.0001$ by ANOVA; *: significant gene silencing by Dunnett's post hoc testing vs. PBS.
(C) Schematic of intracellular Gal8 recruitment; in cells with intact endosomes, Gal8 is dispersed in the cytoplasm without access to intra-endosomal glycans [blue circles]. When endosomal membranes are disrupted, Gal8-YFP binds to these glycans, concentrating into bright, punctate fluorescent spots.
(D) Gal8 confocal micrographs of non-toxic polymers confirms 50B induces robust Gal8 response [white arrow]. Negligible Gal8 recruitment is detected for other polymeric carriers.

3.3.4 Validation of Gal8 Recruitment Assay Using MW Library

In order to produce sufficient data points to assess the correlation between Gal8 recruitment and functional biomacromolecule delivery, Gal8 recruitment (**Figure 3.3B**) was assayed and quantified for all si-NPs at multiple doses. In order to robustly and objectively quantify Gal8 recruitment, automated methods were developed using MATLAB to identify and quantify Gal8 positive spots normalized to total cell number within each imaging frame. Images of recruited punctate Gal8 spots were obtained for the MW library (**Figure 3.3C**), which were automatically annotated (**Figure 3.3C**, magenta) using MATLAB. Image processing algorithms are detailed in the supplemental methods and in **Figure 3.S3**.

All 50B MW series polymers except 50B-S produced striking Gal8 recruitment. Increasing polymer MW increased Gal8 recruitment, with larger MW polymers producing larger degrees of Gal8 recruitment at each dose tested. These data were statistically significant for polymer molecular weight, dose, and interaction thereof when tested by 2-way ANOVA ($p<10^{-4}$, all), with polymer molecular weight, dose, and interaction accounting for 32, 36, and 26% of statistical variation, respectively, suggesting that this method is more sensitive to polymer dosing than even gene knockdown experiments.

To assess the suitability of this assay, the signal-to-noise ratio (S/N), signal-to-background (S/B), and Z-factor score[50] were calculated using the highest response data (50 nM, 50B-XL) as an estimated reference positive control. S/N was calculated to be 2840, S/B to be 6078, and Z′-Factor to be 0.61. In describing the Z′-Factor for assessing the quality of high throughput screening (HTS), Zhang *et al.* describe a $Z' \geq 0.5$ as "an excellent assay," with a high band of separation between the negative control data and identified hits, whereas any assay with a positive Z′-factor "can be used for HTS". In terms of user setup, the data in **Figure 3.3B** can

notably be contained on one well plate, and by leveraging automated fluorescent confocal microscopy, these measurements can be imaged in less than one hour of microscope time.

3.3.5 Cross-Validation Against Standard Methods

We next cross-validated the ability of Gal8 recruitment to serve as a predictor of intracellular bioactivity relative to other widely used standard endosomal escape and drug delivery characterization assays. A robust statistical cross-validation allows the direct comparison of the sensitivity of Gal8 recruitment against other methods of measuring endosomal escape. The 50B system is a well suited polymer system for validating this technique, as it has been well characterized previously,[20,43,47–49] and here characterized with varying molecular weights.

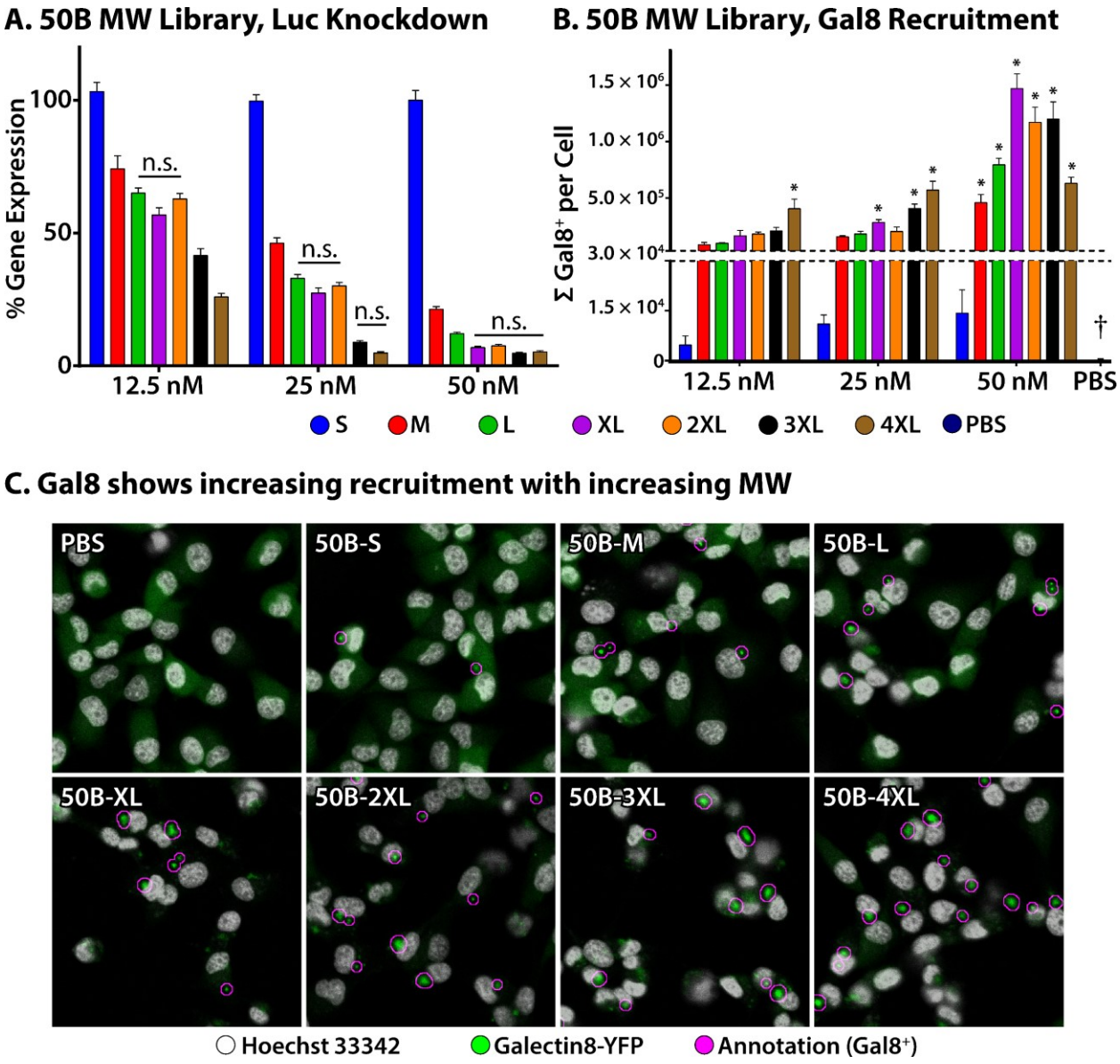

Figure 3.3. Gene knockdown level and Gal8 recruitment correlate for MW library
(A) Dose dependent bioactivity for MW library. Overall $p < 0.0001$ for MW (59% of variation), dose (24%), and interaction (6%) by two-way ANOVA. For each dose, all polymers are statistically different from all other polymers by Tukey's multiple comparisons test, except within groups denoted n.s.
(B) Quantification of Gal8 recruitment confocal images reveals that Gal8 recruitment increases with increasing siRNA dose and increasing polymer MW. PBS treated cells had near zero response, highlighted with †. Overall $p < 0.0001$ for MW (32% of variation), dose (35%), and interaction (25%). *: polymers identified as significant hits by Dunnet's comparison test.
(C) Representative confocal micrographs of Gal8 recruitment at 50 nM siRNA dose. The images have been false-colored; white represents Hoechst staining; green represents Gal8; magenta represents automated annotation of Gal8 positive fluorescent spots.

3.3.5.1. Hemolysis

To assess pH dependent membrane disruptive behavior, we used a hemolysis assay, which is commonly employed as a surrogate marker for pH-dependent endosome membrane disruption.[51] Washed human red blood cells were incubated with si-NPs in buffer at pH 7.4, 6.8, and 6.2, corresponding to physiologic pH and progressively acidifying early endosomes. Intact red blood cells were removed by centrifugation, and the released hemoglobin within the supernatant was measured by absorbance (**Figure 3.4A**). As a control, we repeated hemolysis of the composition library (**Figure 3.4B**). No hemolysis was observed for purely cationic 0B without any hydrophobic BMA incorporation, whereas 25B and 40B exhibit hemolysis at all pH, consistent with their observed high cytotoxicity (**Figure 3.2A**). Only 50B exhibits no hemolysis at pH 7.4 and high hemolysis at pH 6.8. This "switch-like" hemolysis has been hypothesized to be predictive of bioactivity.[30,51,52] Hemolysis results from the MW library showed that the smallest MW polymer, 50B-S, produced weak hemolysis at pH 6.8, which may explain its low bioactivity throughout these studies. The largest two polymers had modest hemolysis at pH 7.4, again in agreement with the observation of mild cytotoxicity for 50B-3XL and 4XL at higher doses (**Figure 3.S2**). All 50B polymers produced switch-like, pH-dependent behavior, with only minor differences in the hemolysis profiles for 50B-M through 50B-2XL, corresponding to MW from 23 000 to 36 300 g/mol. Taken together, these data suggest that overall pK_a, relative hydrophobic content, and molecular weight all cooperate to dictate polymer pH-dependent membrane disruptive activity as measured by the hemolysis assay. Two primary conclusions from these data are: that switch-like hemolysis profiles (*i.e.*, low hemolysis at pH 7.4 with high hemolysis at pH 6.8) are necessary for endosomal disruption, and that hemolysis at pH 7.4 is predictive of cytotoxicity. Hemolysis is useful for ascertaining crude pH responsive profiles and for prediction of cytotoxicity. However,

desirable performance by hemolysis assay does not necessarily predict potent bioactivity, as it does not have the sensitivity to discriminate differences in the 50B MW library that have a broad range of bioactivity levels. In fact, hemolysis at pH 7.4 (which is also indicative of cytotoxicity) was the only hemolysis outcome with statistically significant correlation to bioactivity (**Supplemental Table 1**).

3.3.5.2. Lysotracker Co-Localization Imaging

Next, we correlated knockdown activity with Lysotracker colocalization, a commonly employed method to assess endosomal entrapment. Acidic, membrane-bound vesicles are stained using the acidotropic dye Lysotracker, while the cargo is tracked using a covalently attached fluorophore, in this case, Alexa-488, which has been shown to minimally alter cellular uptake[22] (**Figure 3.4D**). We used blinded, automated analysis to calculate the Manders Coefficient[53] of overlap to qualitatively and quantitatively assess si-NP entrapment in endo-lysosomes (**Figure 3.4E**). At 50 nM siRNA dose, Lysotracker colocalization matches expected values, with smaller molecular weight 50B polymers being more strongly colocalized with endo-lysosomal staining than larger ones. At lower doses, however, the decreased signal from the siRNA fluorophore reduces quality of localization (**Figure 3.4F**). In short, the Lysotracker colocalization data support the hypothesis that larger MW 50B polymers more efficiently escape endosomes. Statistical testing by 2-way ANOVA measured $p < 10^{-4}$ for polymer molecular weight and $p < 0.05$ for interaction between polymer and dose. Polymer MW accounted for 65% of dataset variation, with little measured dose dependency effect. One of the main shortcomings in using Lysotracker colocalization for endosome-buffering polymers is exemplified by the data on 0B polymer (**Figure 3.4D**). The 0B polymer is highly cationic, resulting in high cellular uptake and

endosomal buffering capacity but minimally membrane disruptive, generating negligible endosomal escape activity and consequently little bioactivity (**Figure 3.2B**). The Manders Coefficient for 0B is 0.22, in all likelihood artefactually suggesting little endo-lysosomal colocalization. Presumably, Lysotracker is unable to accumulate in vesicles that contain 0B, due to the polymer's high tertiary amine content and associated pH buffering capacity. These data support the contention that neither high cellular uptake nor a lack of Lysotracker colocalization ensures intracellular bioactivity, in agreement with our previous observations.[43,48] Further, we confirm earlier reports that accurate Lysotracker colocalization data requires siRNA doses higher than those that confer near-maximal gene knockdown,[14] as the 12.5 and 25 nM doses of siRNA produce strong knockdown but have poor signal in Lysotracker colocalization analyses. This is because the amount of siRNA that reaches the cytoplasm necessary to achieve efficient gene knockdown is lower than the limit of detection of many microscopy setups.

Figure 3.4

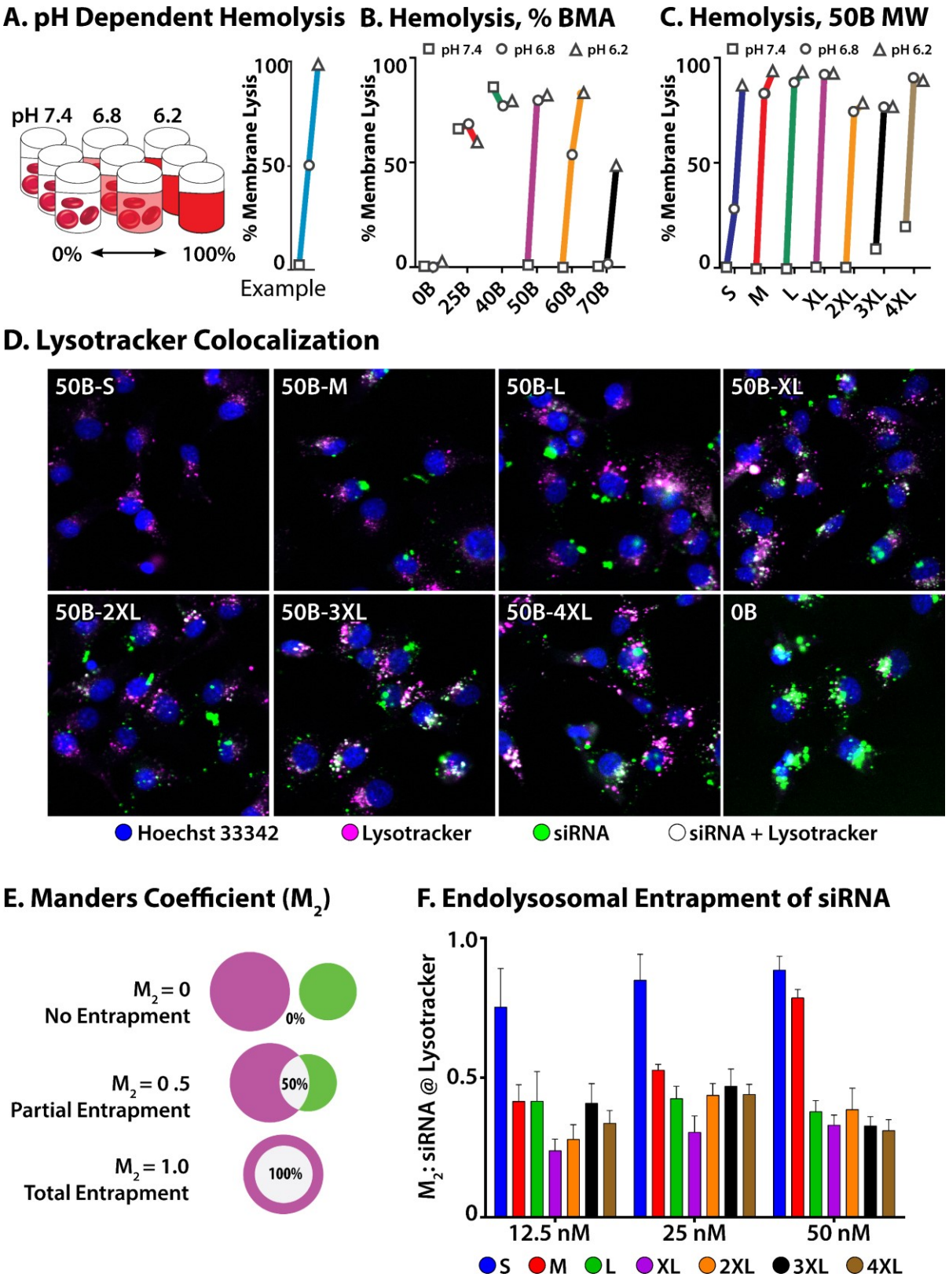
A. pH Dependent Hemolysis
pH 7.4 6.8 6.2
0% 100%
% Membrane Lysis
100
50
0
Example
B. Hemolysis, % BMA
pH 7.4 pH 6.8 pH 6.2
% Membrane Lysis
0B 25B 40B 50B 60B 70B
C. Hemolysis, 50B MW
pH 7.4 pH 6.8 pH 6.2
% Membrane Lysis
S M L XL 2XL 3XL 4XL
D. Lysotracker Colocalization
50B-S
50B-M
50B-L
50B-XL
50B-2XL
50B-3XL
50B-4XL
0B
Hoechst 33342
Lysotracker
siRNA
siRNA + Lysotracker
E. Manders Coefficient (M2)
M2 = 0
No Entrapment
0%
M2 = 0 .5
Partial Entrapment
50%
M2 = 1.0
Total Entrapment
100%
F. Endolysosomal Entrapment of siRNA
M2: siRNA @ Lysotracker
1.0
0.5
0
12.5 nM
25 nM
50 nM
S M L XL 2XL 3XL 4XL

Figure 3.4. MW library pH-dependent hemolysis and Lysotracker colocalization
(A) Overview of red blood cell hemolysis assay; red blood cells are incubated with si-NPs at pH 7.4, 6.8, or 6.2. Intact red blood cells are separated by centrifugation; the relative amount hemoglobin released from disrupted red blood cells is measured in the supernatant by absorbance.
(B) Hemolysis profiles for composition series reveal switch-like hemolysis profiles for 50B from pH 7.4 to 6.8, whereas 60B and 75B require increasingly acidic conditions for hemolysis. No lysis was observed for 0B, and 25B and 40B caused hemolysis at all pHs. pH legend: □, 7.4; ○, 6.8; △, 6.2.
(C) Hemolysis profiles for MW series reveal switch-like hemolysis profiles for all 50B polymers, however, 50B-S has reduced hemolysis at pH 6.8, while 50B-3XL and 50B-4XL have observable hemolysis at pH 7.4. pH legend: □, 7.4; ○, 6.8; △, 6.2.
(D) Representative false-color confocal micrographs of lysotracker microscopy at 50 nM siRNA dose; blue represents Hoechst nuclear staining, magenta represents Lysotracker staining, green represents Alexa-488-siRNA, and white represents colocalization of siRNA with Lysotracker.
(E) Calculation of Manders coefficient of colocalization overlap; where siRNA and Lysotracker are not colocalized, a value of 0 is obtained, but complete colocalization results in a value of 1.0.
(F) Quantification of siRNA colocalization with Lysotracker reveals that the majority of siRNA delivered using 50B-S is localized to endo-lysosomes, whereas less than half of siRNA is colocalized with Lysotracker for all larger polymers.

3.3.5.3. Transmission Electron Microscopy

Endosomal disruption and escape was also visualized directly using TEM for the smallest (50B-S), an intermediate (50B-L), and the largest (50B-4XL) MW polymers with the goal of validating the Gal8 recruitment data. The si-NPs were formulated with 10 nm diameter gold nanoparticles (AuNPs)[29] and applied to cells to enable visualization with TEM imaging. We hypothesized that, based on the Gal8 recruitment data, free AuNP and 50B-S/AuNP would localize to intact lysosomes and that 50B-L and 50B-4XL si-NPs would cause disruption and escape from endosomal membranes (**Figure 3.5A**) as we previously reported for endosome-disruptive poly(propylacrylic acid).[29] The free AuNPs accumulated in electron dense, multilayered lysosomal structures (**Figure 3.5B 1 & S4**). In the sample treated with 50B-S (**Figure 3.5B 2 & S5**), the AuNP were found in membrane bound multi-vesicular bodies which resemble literature reports of late endosomes or autolysosomes,[54] but nearly all gold was found within membrane bound structures. For the 50B-L (**Figure 3.5B 3 & S6**) and 50B-4XL (**Figure 3.5B 4 & S7**) polymers that robustly triggered recruitment of Gal8, lysosomal structures appeared disrupted, and AuNP label was apparent both in the cytosol (white arrowheads) and in structures that may retain a membrane (black arrowheads). Membranes, such as those seen encapsulating AuNP and 50B-S/AuNP, were not apparent and/or were visibly damaged in cells treated with si-NPs formulated with 50B-L and 50B-4XL. These data confirm that pH responsive 50B polymers disrupt the endo-/lysosomal system and release large molecules and even 10 nm gold NPs to the cytosol.

Figure 3.5. Transmission electron microscopy confirms endosomal disruption as predicted by Gal8 recruitment

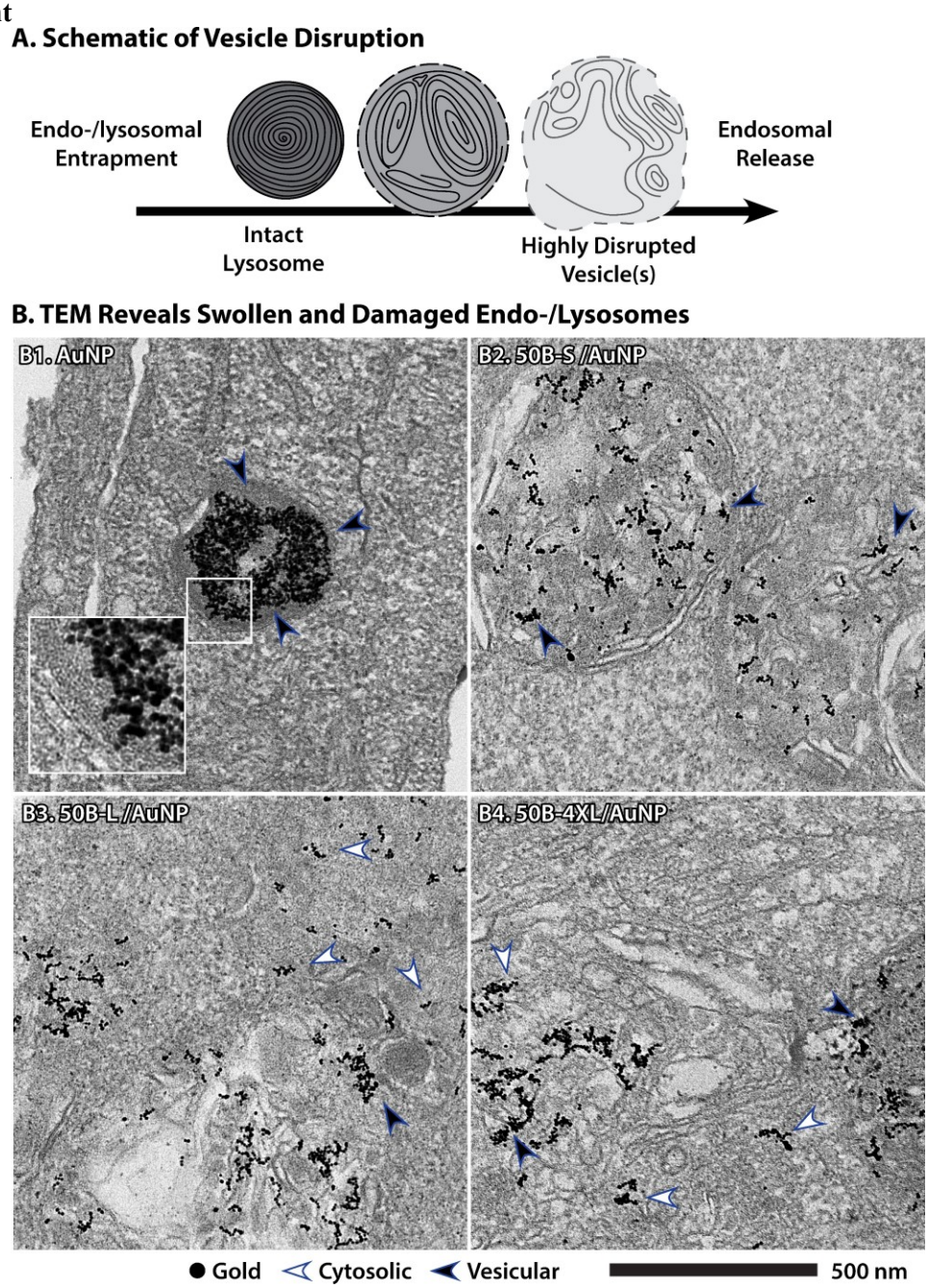

(A) Endo-lysosomes are are multi-lamellar, electron dense structures, that become more swollen with weakly membrane active polymers, while highly membrane active polymers more fully disrupt endosomal membranes and induce a fragmented, multi-vesicular phenotype with incomplete or discontinuous membranes.
(B) Transmission electron microscopy shows AuNPs traffic to electron dense lysosomes, B1, where they are fully enclosed by a lipid bilayer (black arrow), while 50B-S induces a swollen vesicle phenotype, B2, though membrane remains intact. Endosome disruptive polymers 50B-L and 50B-4XL induce widespread loss of endosomal membrane and release AuNPs into cytoplasm (white arrows), though some AuNP remains trapped in membranes (black arrows).

3.3.5.4. Correlation Analysis

Finally, to statistically compare Gal8 recruitment against a variety of predictive assays used to screen biomacromolecular delivery technologies, we plotted the data from **Figure 3.3B** (Gal8 recruitment), **Figure 3.4F** (Lysotracker colocalization), and **Figure 3.S8** (cellular uptake), against dose matched luciferase knockdown data (**Figure 3.3A**) to quantitatively assess the correlation of these measures to intracellular bioactivity using Spearman's method (**Figure 3.6A-C**). For the hemolysis data set, we plotted the difference in hemolysis from pH 7.4 to pH 6.8 at 15 μg/mL against luciferase knockdown at all three doses because human red blood cell hemolysis was only performed at one concentration of polymer. Because this assay is performed on red blood cells in a buffered solution rather than inside an endosome, dose matching is not straightforward. Gal8 recruitment was found to have the highest correlation to luciferase knockdown, with $r = 0.953$ and $p < 10^{-4}$ (**Figure 3.6A**). Measured Lysotracker colocalization was found to have very poor correlation to overall knockdown data, with nonsignificant correlation (**Figure 3.6B**; $r = -0.36$, $p = 0.10$). Cellular uptake as measured by flow cytometry (**Figure 3.S8**) was found to have intermediate correlation for the MW library, with $r = 0.732$ and $p < 10^{-3}$ (**Figure 3.6C**). In addition, the change in hemolysis from pH 7.4 to 6.8 had very low predictive value (**Figure 3.6D**; $r = 0.04$, $p = 0.96$), and does not clearly predict which polymers will have the highest in-cell endosome disruption capacity. The hemolysis assay is good at ruling out cytotoxic formulations and true negative hits; however, what appear to be ideal endosomolysis profiles can be see with "false positives" that do not generate high levels of in-cell activity, and the assay is not sensitive enough to discriminate between formulations with varied levels of efficacy. Further, molecular weight of the polymers has statistically significant correlation to knockdown at all three doses tested, validating our hypothesis that increasing p(DMAEMA-co-BMA) si-NP core-forming block

molecular weight increases gene knockdown activity (**Figure 3.S9**, $r > 0.9$, $p < 0.01$).

Next, we wanted to confirm the predictive value of Gal8 recruitment imaging in a different cell type and for a therapeutically-relevant, non-model gene. To do so, we focused on a non-cancer A7R5 rat vascular smooth muscle cells and the gene prolyl hydroxylase domain-containing protein 2 (PHD2) with a validated rat siRNA, which we have been interested in studying as a target relevant for pro-angiogenic wound healing therapy.[55–57] For this study, we used quantitative reverse transcription PCR to measure PHD2 mRNA levels following treatment with siNPs formulated with 50B-S, 50B-L, and 50B-3XL polymers to get a range of endosomolytic potency properties based on the MDA-MB-231 studies. In this study, we saw the expected trends between polymer molecular weight and gene knockdown (**Figure 3.6E**), and between polymer molecular weight and Gal8 recruitment level (**Figure 3.6F**). In agreement with the model gene observations in MDA-MB0231 cells, there was a statistically significant correlation ($r = 0.995$, $p < 0.001$) between Gal8 recruitment level and percent gene knockdown (**Figure 3.6G**). As an added confirmation, we also found that knockdown of the model gene luciferase in the A7R5 cells followed the expected trend with regard to polymer molecular weight (**Figure 3.S10**). These results confirm the more general application of Gal8 as predictive of gene silencing across multiple polymers, doses, cell types, and genes.

Figure 3.6.

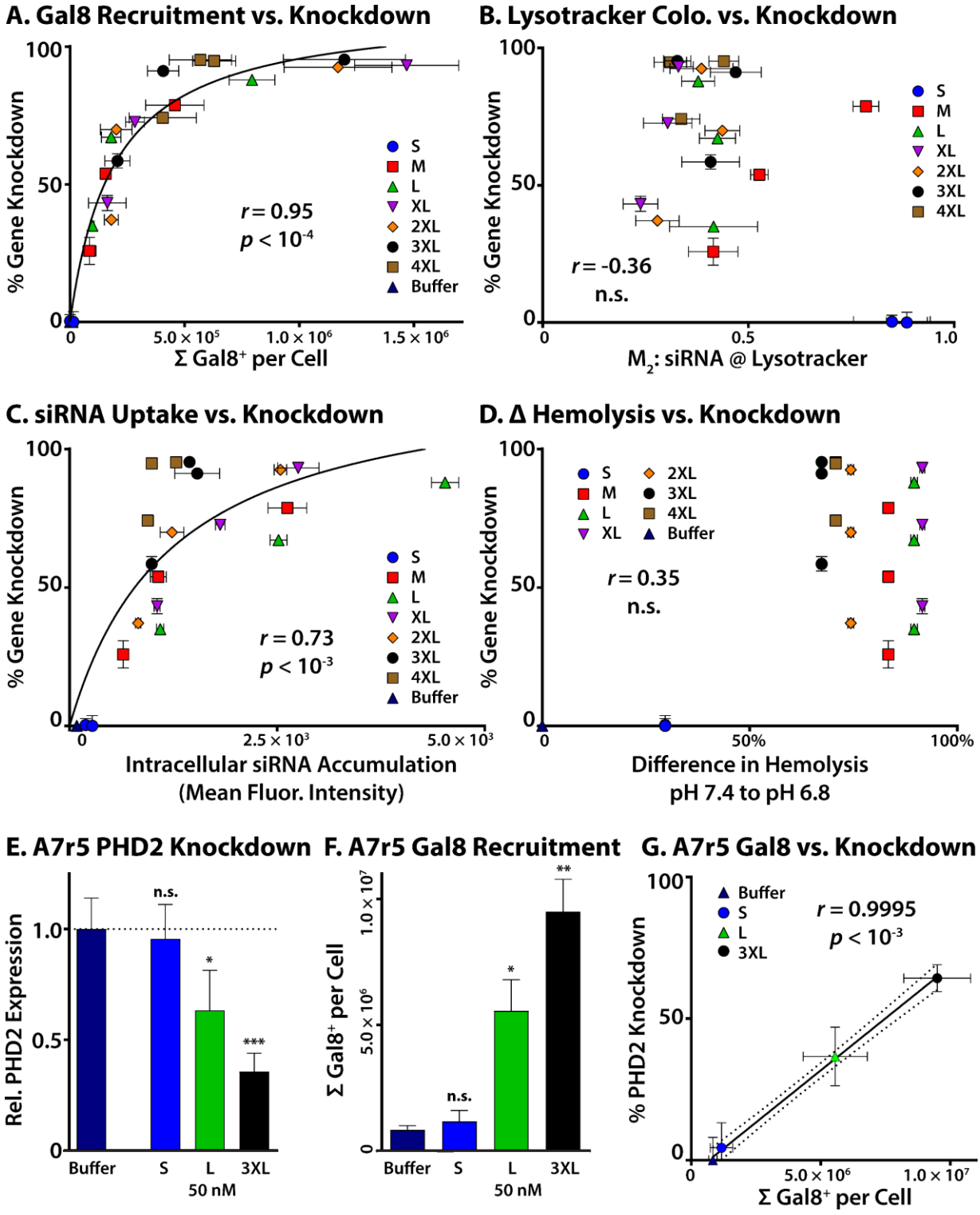
A. Gal8 Recruitment vs. Knockdown
% Gene Knockdown
Σ Gal8⁺ per Cell
r = 0.95
p < 10⁻⁴
S
M
L
XL
2XL
3XL
4XL
Buffer
B. Lysotracker Colo. vs. Knockdown
% Gene Knockdown
M2: siRNA @ Lysotracker
r = -0.36
n.s.
C. siRNA Uptake vs. Knockdown
% Gene Knockdown
Intracellular siRNA Accumulation
(Mean Fluor. Intensity)
r = 0.73
p < 10⁻³
D. Δ Hemolysis vs. Knockdown
% Gene Knockdown
Difference in Hemolysis
pH 7.4 to pH 6.8
r = 0.35
n.s.
E. A7r5 PHD2 Knockdown
Rel. PHD2 Expression
Buffer
S
L
3XL
50 nM
n.s.
F. A7r5 Gal8 Recruitment
Σ Gal8⁺ per Cell
G. A7r5 Gal8 vs. Knockdown
% PHD2 Knockdown
Σ Gal8⁺ per Cell
r = 0.9995
p < 10⁻³

Figure 3.6. Validation of Gal8 recruitment as a predictor of bioactivity relative to common standard delivery and endosome escape readouts
(A) Gal8 recruitment (*x*-axis) and luciferase gene knockdown data (*y*-axis) from MDA-MB-231 cells were plotted, and a hyperbolic fit was calculated. Correlations were calculated by Spearman's method; $r = 0.95$, $p < 10^{-4}$. Gal8 recruitment and knockdown measurements are dose-matched (12.5, 25, and 50 nM) and include buffer treated control. For additional discussion of this data, see Technical Note 1 in the supplemental information.
(B) Lysotracker colocalization as measured by Manders coefficient (*x*-axis) and luciferase gene knockdown data (*y*-axis) from MDA-MB-231 cells were plotted. Correlations were calculated by Spearman's method; correlation was not statistically significant. Manders coefficients and knockdown measurements are dose-matched (12.5, 25, and 50 nM).
(C) siRNA cellular uptake as measured by mean fluorescence intensity by flow cytometry (*x*-axis) and luciferase gene knockdown data (*y*-axis) from MDA-MB-231 cells were plotted, and a hyperbolic fit was calculated. Correlations were calculated by Spearman's method; $r = 0.73$, $p < 10^{-3}$. Cell uptake and knockdown measurements are dose-matched (12.5, 25, and 50 nM) and include buffer treated vehicle control.
(D) The difference in hemolysis response from pH 7.4 to 6.8 (*x*-axis) from human erythrocytes and luciferase gene knockdown data (*y*-axis) from MDA-MB-231 cells were plotted. Correlations were calculated by Spearman's method for hemolysis data for each dose of knockdown data individually; despite increased likelihood of Type I error, correlation at no individual dose was statistically significant. Hemolysis data are for 15 μg/mL polymer concentration, and knockdown data are at 0 (vehicle control), 12.5, 25, and 50 nM siRNA.
(E) Relative PHD2 expression from A7r5 cells treated with si-NPs at 50 nM were measured using qPCR and calculated as $2^{-\Delta\Delta CT}$. Treatment with 50B-L or 50B-3XL induced statistically significant reductions in PHD2 mRNA levels. The symbols * and *** represent $p < 0.05$ and 0.001 respectively.
(F) Gal8 recruitment measurements from A7r5 cells treated with 50 nM siNPs show 50B-L and 50B-3XL induce statistically significant Gal8 recruitment. The symbols * and ** represent $p < 0.05$ and 0.01 respectively.
(G) Gal8 recruitment (x-axis) and PHD2 gene knockdown data ($100 \times [1 - 2^{-\Delta\Delta CT}]$; y-axis) were plotted. Because saturation was not observed in either Gal8 recruitment or gene knockdown data, a linear fit was calculated and correlations were calculated by Pearson's method; $r = 0.995$, $p < 10^{-3}$. Gal8 recruitment and knockdown measurements are dose-matched (50 nM) and include buffer treated control. For additional discussion of this data, see Technical Note 1 in the supplemental information.

3.3.6 Gal8 Imaging Extension to In Vivo Endosome Disruption Visualization

As a further extension of this technique, we sought proof of concept of Gal8 imaging for *in vivo* visualization and measurement of endosome disruption. To show that Gal8 recruitment occurs *in vivo* and that it corresponds to *in vivo* bioactivity, we used an optimized si-NP formulation based on our previous work.[47,49,57] This system consists of the same 50B core as our *in vitro* library combined with an inert, zwitterionic corona chemistry and a hydrophobized siRNA to confer additional stability and pharmacokinetic benefits. To validate the utility of the Gal8 system *in vivo*, we characterized both *in vivo* luciferase knockdown and *in vivo* Gal8 recruitment in an orthotopic breast cancer model. Orthotopic MDA-MB-231 tumors carrying either firefly luciferase or Gal8-YFP constructs were introduced into the mammary fat pads of nude mice, and si-NPs were injected *via* the tail vein.

Gal8 imaging revealed that tumors from mice treated with si-NPs exhibited a significant increase in Gal8-associated endosomal disruption of 4.58-fold relative to mice treated with PBS injections (**Figure 3.7A & Figure 3.S11A**). In a separate cohort of mice, we showed, as expected, intravital luminescence readings reveal a statistically significant reduction in luciferase activity for the si-NPs formulated with luciferase targeting siRNA relative to the scrambled control (**Figure 3.7B**). This indicates that Gal8 imaging successfully measures drug carrier mediated endosomal disruption, which correlates with siRNA delivery to the cytosol of tumor cells *in vivo*. These data are notable as providing visualization and measurement of endosomal disruption mediated by *in vivo* nanocarrier treatments performed on fresh, unfrozen, intact tissue without exogenous fluorophores or acidotropic dyes. Notably, a small number of confocal micrographs of tumors from PBS treated animals showed detectable Gal8 recruitment, probably associated with cell stress response to the tumor microenvironment. One extreme outlier within

the PBS group, which was not excluded from analysis, showed Gal8 recruitment that was 348-fold higher than median PBS tumor. Likewise, Gal8 imaging of tumors from animals treated with si-NPs was expectedly variable, likely due to known heterogeneities in tumor microenvironment[58–60] (**Figure 3.S11B**). It is increasingly recognized that many types of cancer have dysregulated increased levels of autophagy to promote survival under stressful conditions.[61,62] It is reported that endosomal disruption specifically induces autophagy,[29,35,37] possibly leading to enhanced basal Gal8 recruitment in tumors *in vivo* relative to *in vitro* contexts, as poorly vascularized cancer cells induce autophagy to fuel additional growth. Further, the Gal8 response observed was weaker than anticipated given the luciferase knockdown results, potentially due to suboptimal time points chosen. Multiple events with independent kinetics occur simultaneously *in vivo*: distribution by the vascular system, tissue and cellular uptake, endosomal escape, mRNA degradation by RISC, and endogenous degradation of luciferase protein. Gal8 imaging only provides a snapshot of endosomal disruption at one timepoint. Timing for the experiment could likely be improved, especially with advanced animal techniques such as intravital microscopy or tumor window models, which would increase statistical power by providing same tumor controls and repeated sampling. Obviously, the need for statistically powered cohorts of animals precludes the use of *in vivo* Gal8 imaging for high throughput screening; this experiment is best understood as providing proof of concept that interesting information can be inferred about the real-time, *in vivo* status of endosomal integrity, though these studies are complicated by pharmacokinetics and potential false positives from intracellular polymer delivery without accompanying cargo delivery (*e.g., bona fide* endosomal disruption from polymer after siRNA has been unpackaged). Despite these limitations, intra-tumoral Gal8 imaging shows strong promise as a technique for assessing endosomal disruption by nanocarriers

in animal experiments, and there may be opportunity to improve *in vivo* application of this methodology by intravital imaging over a more extended timeframe or achieving more complete sampling throughout the tumor with reduced logistic burden by cryosectioning, especially when combined with fluorescent labels to track polymer and siRNA.

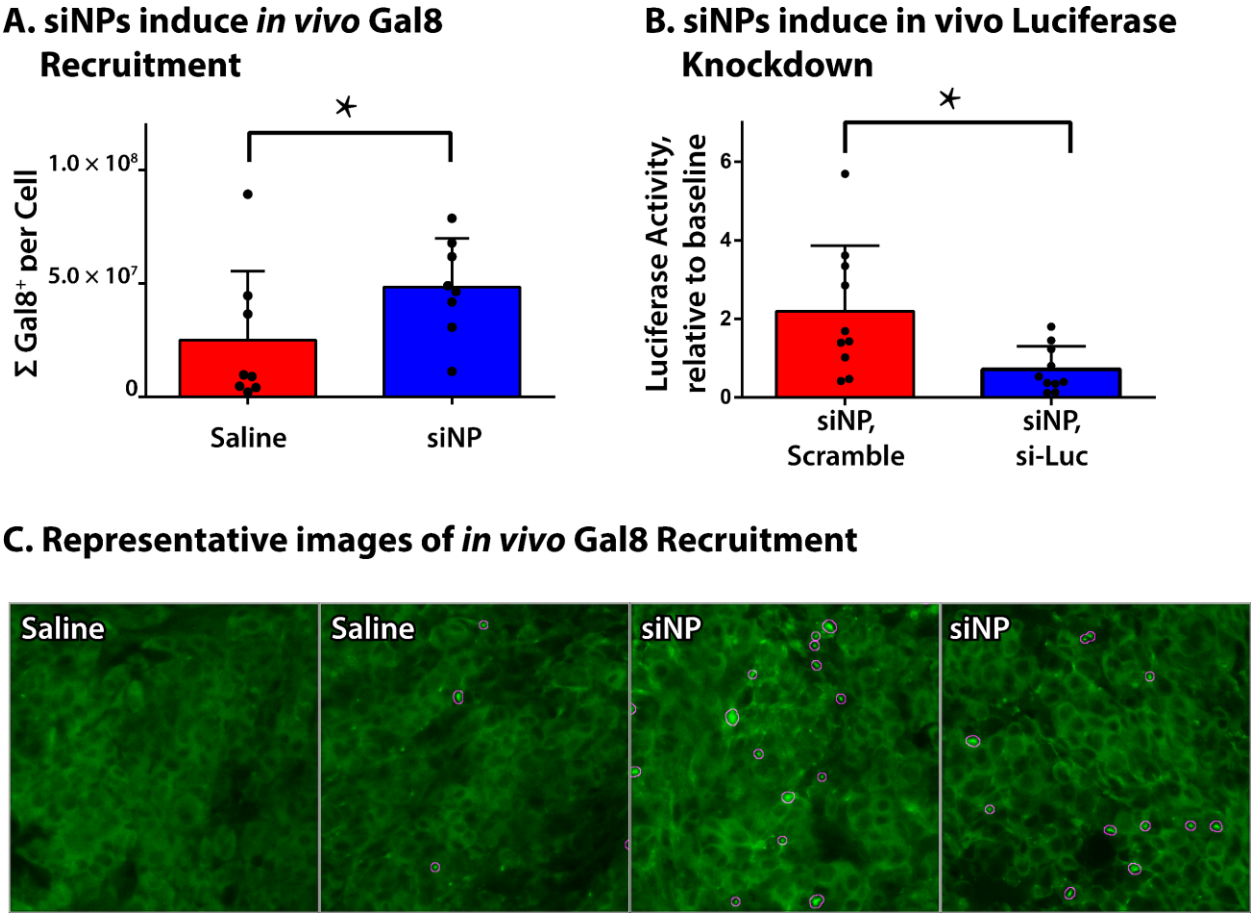

Figure 3.7. In vivo proof of concept for utilization of Gal8 imaging for visualization and measurement of endosome disruption within tumor tissue following systemic delivery of endosome-disruptive si-NPs.

(A) si-NPs induce significant endosomal disruption; n = 8 tumors *per* group, *: $p < 0.05$ by unpaired two-sided Mann Whitney test.
(B) si-NPs delivering luciferase targeting siRNA significantly reduce luciferase signal relative to scrambled sequence control; n = 10 tumors *per* group, *: $p < 0.02$ by unpaired two-sided Student's t-test.
(C) Representative images of saline (left) and si-NP treated tumors (right). Disrupted endosomes as identified algorithmically are identified with magenta circles.

3.4 Conclusions

One of the major limitations in developing improved intracellular drug delivery systems has been the difficulty of directly assessing active endosomal escape. Existing methods are prone to artefacts, typically require fluorophore labeling of the biologic cargo, are often indirect and thus not representative of the extent of endosomal damage, and are not amenable to high throughput analysis. Here we validated Gal8 recruitment as a measure of endosomal disruption that circumvents limitations of current common, standard techniques, and correlated this endosomal disruption to siRNA bioactivity. By validating the technique with a well-characterized series of different polymer compositions, we show that endosome disrupting polymers that facilitate intracellular biologic cargo activity result in increased Gal8 recruitment. This technique was then used to study the effects of 50B MW on endosome disruption. We show that Gal8 recruitment has a higher correlation to functional bioactivity for a library of endosome-escaping siRNA delivery polymers than alternative methods of predicting bioactivity for drug carriers, such as Lysotracker colocalization, hemolysis, or cellular uptake, and that this method further obviates the need for expensive, exogenous fluorophores to track cargo localization and uptake. This study also provided insights into the strong correlation between polymer molecular weight and endosome escape and bioactivity for the 50B polymer composition. Further, we extended this technique to orthotopic breast tumors *in vivo,* showing that Gal8-visualized, nanocarrier-mediated endosomal disruption also correlates with *in vivo* gene knockdown activity in the tissues of treated animals.

One underappreciated aspect within the drug delivery field is that endosomal disruption *ipso facto* induces autophagy of damaged endosomes as a consequence of Gal8 recruitment.[29,35,37] Gal8 signaling to NDP52[63,64] leads to the formation of phagophores capturing

these damaged organelles. Phagophores then mature into autophagosomes, which fuse with lysosomes.[65] The steps downstream of endosomal disruption are poorly understood in the context of drug carriers, and additional efforts should focus on understanding and modulating the timing and mechanisms at play between disruption and ultimate re-containment of the damaged endosome, presumably the time period when cargo escape can occur.

We believe that the quantitative Gal8 imaging technique will show broader utility beyond siRNA-focused library screens for silencing of model genes such as luciferase. For siRNA, activity and mechanistic (endosome disruption) screens completed in parallel are expected to provide a deeper level of structure-function insight and lead to better paths to carrier structural optimization relative to screening for activity alone. However, this assay may in fact find its greatest utility in screening formulations of biologic drugs whose delivery is more difficult to assay using high throughput using reporter (*e.g.*, luciferase or GFP) methods. For example, the development of therapeutic peptides, enzyme replacement therapies, blocking antibodies, and non-viral gene editing systems have all been hampered to a degree by inefficient screening techniques.[10,16,30,66–68] Our vision for the system is that Gal8 recruitment activity can be used as an early "down-selection criteria" in HTS screening of candidate delivery system libraries, especially when a specific parameter of structure or formulation is being investigated (*e.g.*, overall MW, as we investigated here). In conjunction with additional, orthogonal HTS assays (*e.g.*, toxicity), a large number of experimental groups can be reduced to a manageable number ("hits", occurring at the intersection of top performers in both Gal8 and toxicity screening) for use in more intensive assays that provide additional information about intracellular pharmacokinetics, intracellular trafficking, or bioactivity. Indeed, our studies here show the best performing polymers also perform best in the Gal8 recruitment screen, although this predictive

power is not perfect.

Despite its potentially broad applicability, there are some obvious limitations of the Gal8 recruitment imaging method. First, it requires the engineering of cell lines to express a transgene construct and requires a microscope equipped with a software-controlled stage, multi-well or 96-well plate mount, and appropriate excitation and emission filters. While here we used a typical Nikon confocal system, this method should be amenable to other high throughput and plate-reader based microscopy systems, as Gal8 recruitment produces puncta that can be resolved with a relatively low power 20x objective. Further, cells must be very carefully handled in conjunction with this assay, and use of inappropriate wash buffers may induce Gal8 recruitment independent of carrier-driven endosomal rupture, creating false positive signals. Careful use of vehicle controls is a viable way to be sure to have an accurate baseline. Finally, while the system is amenable to multiple polymers, doses, and cell types, assay conditions such as time point and wash buffers may need to be optimized to account for differences in polymer characteristics or cell-type specific differences in mechanisms of endocytosis, endosomal trafficking, and endosomal disruption. In sum, imaging and quantification of Gal8 recruitment allows high-throughput, real-time, live-cell, and fluorophore-free measurements of active endosomal escape. This method provides a powerful tool for rapidly optimizing and elucidating structure-function relationships for libraries of biologic nanomedicine candidates.

3.5 Materials and Methods

3.5.1 Materials

All chemical synthesis reagents were obtained from Sigma-Aldrich and used as received unless otherwise noted. 2-(Dimethylamino)ethyl methacrylate (DMAEMA) and butyl

methacrylate (BMA) monomers were passed twice through a basic alumina gravity column prior to use in order to remove inhibitors. 2,2-Azobis(2-methylpropionitrile) (AIBN) was recrystallized twice from methanol. Titration reagents, hydrochloric acid (HCl) solution (certified 0.0995-0.1005 N), and sodium hydroxide (NaOH) solution (certified 0.0995-0.1005 N), were obtained from Fisher Scientific. Poly[(ethylene glycol)-b-[(2-(dimethylamino)ethyl methacrylate)-co-(butyl methacrylate)]] polymers were synthesized using RAFT polymerization as previously reported.[20,47] The macro-chain transfer reagent was synthesized by coupling 5000 g/mol PEG to 4-Cyano-4-(ethylsulfanylthiocarbonyl) sulfanylvpentanoic acid (ECT) using DCC-DMAP coupling. Macro-CTA synthesis and polymer synthesis are shown as **Figure 3.S1** and previously reported.[20,49,69] An optimized *in vivo* polymer, poly[2-(methacryloxyethyl) phosphorylcholine] (PMPC)-b-(DMAEMA-co-BMA) was synthesized, characterized, and purified as previously described[47] with a degree of polymerization of 75 for the each of DMAEMA, BMA, and 2-(methacryloxyethyl) phosphorylcholine. PD10 desalting columns (GE Healthcare, Waukesha, WI, USA) were used for the final purification of polymers according to manufacturer's instructions. Oligonucleotide sequences were used as previously reported from Integrated DNA Technologies or Sigma-Aldrich.[49] Alexa 488 labeled dsDNA were used for Lysotracker and cell uptake experiments. LysoTracker Red DND-99 was obtained from ThermoFisher Scientific.

3.5.2 Polymer Characterization

Polymers were characterized using ^{1}H nuclear magnetic resonance spectroscopy (Bruker, 400 MHz). Units of DMAEMA and BMA were calculated by integrating these peaks relative to the PEG peak; number average molecular weight (M_n) was calculated by adding the mass from

these components and is referred to using the acronym MW throughout the manuscript. Polydispersity was evaluated with DMF mobile phase gel permeation chromatography (GPC, Agilent Technologies, CA), dissolved at 10 mg/mL in DMF containing 0.1 M LiBr.

3.5.3 pK_a Measurement

The log acid dissociation constant (pK_a) was measured for all polymers *via* acid-base titration using an MPT Titrino automatic titrator (Metrohm, Switzerland). Polymers were dissolved in 0.1 N HCl to a final concentration of 5 mg/mL and titrated to the basic endpoint with 100 µL additions of 0.1 N NaOH. The pK_a was calculated as the half-neutralization point of each titration.

3.5.4 Nanoparticle Complexation

Desalted, lyophilized polymers were dissolved in 100% ethanol at 33.3 mg/mL, diluted 1:10 into pH 4.0 citric acid buffer (10 mM) and stored at -20 °C until further use. Polymers were complexed with siRNA at pH 4.0 for 0.5 h, then neutralized with 5-fold excess pH 8.0 phosphate buffer (10 mM). The product was syringe filtered (0.45 µm) and then diluted into appropriate buffer for siNP characterization studies or DMEM containing 10% FBS for *in vitro* cellular studies. The naming scheme used for the composition library corresponds to the mole percent BMA in the feed for the p(DMAEMA-co-BMA) block of the polymer. The naming scheme used for the MW library corresponds to the relative MW of the p(DMAEMA-co-BMA) block, where S, M, L, XL, 2XL, 3XL, and 4XL correspond to small, medium, large, extra-large, double extra-large, triple extra-large, and quadruple extra-large, respectively.

3.5.5 Dynamic Light Scattering (DLS) to Measure Nanoparticle Size

Si-NPs were prepared at 100 μg/mL in PBS -/-. Hydrodynamic radius was measured using dynamic light scattering (Zetasizer Nano ZS, Malvern Instruments, Westborough, MA).

3.5.6 Cell Culture

Human epithelial breast cancer cells (MDA-MB-231) were obtained from ATCC. To generate cells stably expressing luciferase and GFP, HEK-239-T cells from ATCC were transfected with pGreenFire1-CMV (constitutive firefly luciferase, GFP, and puromycin resistance) plasmid and packaging plasmids pMDLg/pRRE, pRSV-Rev, and pMD2.G with lipofectamine to generate psueodotyped lentiviral particles which were applied to MDA-MB-231s, selected with puromycin, and sorted using FACS as previously reported.[49] Gal8 retrovirus was generated using HEK 293-T cell transfected with Gal8-YFP, pUMVC, and pCMV-VSV-G. Luciferase transduced cells (Luc-MDA-MB-231) were obtained following fluorescence activated cell sorting (BD LSR II Flow Cytometer, San Jose, CA) for GFP+ cells after a two-week puromycin selection. Gal8-YFP transduced cells (Gal8-MDA-MB-231) were obtained by one-week selection with blasticidin, followed by single clonal expansions obtained through the limiting dilution method in blasticidin containing media; clonal populations were used to ensure consistent expression of YFP constructs. Cells were cultured in DMEM supplemented with 10% fetal bovine serum and 0.1% gentamicin. All cell culture reagents were obtained from Gibco (Carlsbad, CA, USA). Both MDA-MB-231 engineered cell lines were assessed for flow cytometry and were found to have minimally altered levels of cellular uptake of si-NPs (**Figure 3.S12**).

3.5.7 Gal8 Recruitment Assays

Gal8-MDA-MB231 cells were plated in Nunc Lab-Tek 8-well chambered coverglass (Nunc, Thermo Fisher Scientific Inc., Waltham, MA, USA) or Corning 96 Well Half-Area High Content Imaging Glass Bottom Microplates (Corning Inc., Corning, NY, USA; product no. 4580) at a density of 6250 cells / cm^2. Cells were left to adhere and proliferate for 24 h before being treated siRNA formulations. After a 17 h treatment, media was aspirated and replaced with warm FluoroBrite DMEM supplemented with 25 mM HEPES, 10% FBS, and Hoechst 33342. Images were acquired with Nikon C1si+ confocal microscope system on a Nikon Eclipse Ti-0E inverted microscope base, Plan Apo VC 20× objective, Galvano scanner, and 408/488/543 dichroic mirror. PerfectFocus was used to maintain focus between wells. The PerfectFocus offset was set to the optimal focal plane of the nuclear stain (blindly, without looking at the Gal8 layer) in combination with the well-scanning mode in ND Acquisition to acquire images, removing microscopist bias. A software-controlled motorized stage moved the plate between images. For additional information regarding microscopy systems for reproduction of this assay, please see Technical Note 2 in the supplemental information. Images were exported to lossless multipage TIF from Nikon NIS-Elements AR version 4.30.01. Exported images were then analyzed in bulk using a blinded, automated MATLAB script which is detailed below and has been made available *via* the FigShare platform.[70] To improve print clarity, images were brightened *via* linear scaling to the max pixel intensity value *per* channel of the top 0.01% of Gal8 pixels or top 1% of Hoechst pixels using MATLAB. While these enhancements were made for print, all quantification was done on raw images.

3.5.8 Gal8 Image Processing

A MATLAB script was written to identify Gal8 positive spots (**Figure 3.S2. A-C**). A binary mask was generated containing Gal8 positive puncta, which were used to integrate underlying Gal8 intensities on unprocessed images and normalized to the number of nuclei. The Gal8 mask was generated by using a tophat filter on the YFP fluorescence channel to perform localized background subtraction to suppress diffuse cytosolic fluorescence (**Figure 3.S2. D**). This was followed by simple thresholding to identify Gal8 pixels (**Figure 3.S2. E**) and subsequent image "morphological opening" using a 3 x 3 pixel "+" shaped structuring element to restrict positive pixels to puncta (**Figure 3.S2. F**). From this, a "visual check" layer was generated by the exclusive or ("XOR") of the mask and its dilation, generating a "halo" around identified spots (**Figure 3.S2. G**) to allow manual verification of algorithm detection success. The Gal8 mask (**Figure 3.S2.F.**) was applied to the unprocessed Gal8 image and the result was integrated, quantifying total Gal8 present within the puncta. This sum was divided by cell number, which was determined by the following image analysis method: a simple threshold was applied to the Hoechst channel (**Figure 3.S2. I**), followed by an image opening to separate proximal nuclei (**Figure 3.S2. J**), and segmenting using a watershed transformation (**Figure 3.S2. K**). A rainbow colormap was applied to the image and the result was exported (**Figure 3.S2. L**), which served as verification that nuclei were properly quantified. Note that contiguous nuclei (*e.g.*, during mitosis) were counted as one cell. Fluorescent composite images (**Figure 3.S2. A**), as well as three method verification images were exported. The first verification image circles identified Gal8 spots (**Figure 3.S2. M**); the second verification image shows identified puncta as magenta overlays (**Figure 3.S2. N**); the

third verification image identifies nuclear number (**Figure 3.S2. L**). Gal8 recruitment code has been made available by the authors *via* the FigShare platform at the URL https://doi.org/10.6084/m9.figshare.7066472.[70]

3.5.9 Lysotracker Colocalization Image Processing

Wild type MDA-MB-231 cells were seeded at a density of 6250 cells / cm^2 in half area 96 well imaging plates as for Gal8 assays. Cells were treated with Alexa488-labeled dsDNA loaded si-NPs at indicated doses. After treatment for 24 h, media was replaced with Lysotracker Red (Invitrogen Life Technologies, Grand Island, NY, USA) containing media (75 nM) and incubated 1 h. Before imaging, cells were washed and media was replaced with Fluorobrite DMEM supplemented with 10% FBS and 25 mM HEPES. Images were analyzed using an automated MATLAB script for Manders Coefficient as originally described.[53] Code to calculate Manders Coefficient of Overlap has been made available by the authors on the FigShare platform, accessible at the URL https://doi.org/10.6084/m9.figshare.7066490.[71]

3.5.10 siRNA Cell Internalization Flow Cytometry Studies:

Wild type MDA-MB-231 cells were seeded in triplicate in 12-well plates at a density of 60 000 cells/well and left to grow for 24 h, before being treated with si-NPs formulated with Alexa-488 labeled dsDNA at indicated doses and incubated for 16 h. Cells were washed with PBS, treated with 0.05% trypsin, and centrifuged at 500 × g for 5 minutes. The supernatant was removed, and cells were resuspended in 300 μL PBS. Single cell suspensions were analyzed using a BD LSR Fortessa flow cytometer, gated according to FSC and SSC. Mean fluorescence intensities (MFI) were calculated using FlowJo (FlowJo LLC, Ashland, OR).

3.5.11 pH-Dependent Membrane Disruption Hemolysis assays:

Hemolysis with red blood cells was performed as previously described.[51] Briefly, blood was donated by an anonymous human donor using a protocol approved by the Vanderbilt institutional review board (IRB). Red blood cells (RBCs) were isolated and washed by centrifugation and then diluted into buffered saline solutions at pH 7.4, 6.8, or 6.2 representative of extracellular, early endosomal, and late endosomal environments. si-NPs at concentration of 15 ug/mL polymer were incubated with RBCs in each buffer for 1 h at 37 ºC. RBCs were centrifuged, and the optical absorption of the supernatant at 450 nm was used to measure the hemoglobin released compared to PBS (negative control) and 1% Triton X-100 (positive control) treated RBCs.

3.5.12 Luciferase Knockdown siRNA Bioactivity Assay

Luc-MDA-MB-231 cells were plated in black walled 96 well plates at a density of 67 000 cells/cm^2. The cells adhered overnight and were then treated with the si-NPs containing siRNA targeting luciferase or non-targeting negative control siRNA for 24 h. Media containing 150 μg/mL luciferin was added at 24 h and 48 h time-points, and bioluminescence was measured using an IVIS 200 Series imaging system (Xenogen Corporation, Alameda, CA, USA).[20]

3.5.13 Cell Viability

For the composition library toxicity studies, Luc-MDA-MB-231s were treated with PBS or si-NPs loaded with control nucleic acids. Luciferase activity was measured to assess intact cells as for luciferase knockdown studies. The ratio of luminescence of scrambled sequence si-NP

treated cells to PBS treated cells at 24 h post treatment was used as a measure of viability. For the MW library, the more sensitive CellTiter Glo assay (Promega, Madison, WI), which measures retained cellular ATP, was used according to manufacturer protocol to measure dose-dependent and polymer-dependent toxicity effects. Wild type MDA-MB-231 cells were plated in black walled 96 well plates at a density of 67 000 cells/cm^2 and allowed to adhere overnight and were then treated with the si-NPs containing non-targeting negative control siRNA for 24 h before CellTiter Glo assay components were added to cells. Luminescence was read using an IVIS 200 Series imaging system.

3.5.14 Transmission Electron Microscopy

MDA-MB-231 cells were plated in 100 mm dishes. Gold labeled si-NPs were formulated at 50 nM siRNA loaded into 50B-S, 50B-L, or 50B-4XL and loaded with anionic surface functionalized 10 nm colloidal gold (Sigma Aldrich Cat. 752584) as previously reported[29]. Cells were treated for 24 h and washed with 0.1 M cacodylate buffer prior to fixation and processing. Samples were fixed in 2.5% glutaraldehyde in 0.1 M cacodylate buffer, pH 7.4 at 37 °C for 1 h and then stored at 4 °C overnight. Samples were submitted to the Vanderbilt Cell Imaging Shared Resource Electron Microscopy Center, where they were washed in 0.1 M cacodylate buffer, then incubated 1 h in 1% osmium tetraoxide at RT then washed with 0.1 M cacodylate buffer. Subsequently, the samples were dehydrated through a graded ethanol series, followed by 3 exchanges of 100% ethanol and 2 exchanges of pure propylene oxide (PO). Dehydrated samples were infiltrated with 25% Epon 812 resin and 75% PO for 0.5 h at RT, followed by infiltration with Epon 812 resin and PO [1:1] for 1 h at RT and subsequent infiltration with fresh Epon 812 resin and PO [1:1] overnight at RT. The samples were subsequently infiltrated with

resin for 48 h and then allowed to polymerize at 60 °C for 48 h. Samples were cut into 500 – 1000 nm thick sections using a Leica Ultracut microtome. Thick sections were contrast stained with 1% toluidine blue and imaged with a Nikon AZ100 microscope to locate cells. 70–80 nm ultra-thin sections were cut and collected on 300-mesh copper grids and then post-stained with 2% uranyl acetate followed by Reynolds' lead citrate. Thin samples were imaged on a Philips/FEI Tecnai T12 electron microscope. For publication, TEM images were contrast enhanced and sharpened in Adobe Photoshop CS6 using the "Levels" tool, setting the 50% grey point to the center of the intensity distribution. Images were then sharpened using the "Smart Sharpen" filter, with "Amount: 100%" and "Radius: 5 px" to "Remove: Gaussian Blur." This procedure was used on all images.

3.5.15 qPCR Studies

Real-time, quantitative, reverse transcription PCR (qPCR) was performed using TaqMan assay reagents and primers to quantify expression of PHD2. Total RNA was isolated purified from cultured A7r5 rat cells with Qiazol and RNeasy spin columns (Qiagen). RNA was reverse transcribed (1 μg) with an iScript Reverse Transcription Supermix kit (Bio-Rad Laboratories). Relative expression of PHD2 was assessed as $2^{-\Delta\Delta CT}$, normalized to housekeeping gene GAPDH (assay IDs: Rn00710295_m1, Rn01775763_g1; Applied Biosystems). siRNA was used as previously described.[55–57]

3.5.16 In Vivo Studies

Athymic nude mice (catalog 002019 Nu/J) were ordered from Jackson Labs. All procedures were carried out under Vanderbilt University IACUC approved protocols. Mice were

injected with 10^6 MDA-MB-231 cells suspended in 1:1 DMEM-Matrigel into the mammary fat pad. MDA-MB-231 cells stably expressing firefly luciferase or Gal8-YFP were used for knockdown or Gal8 experiments, respectively. *In vivo* formulations of (PMPC)-b-(DMAEMA-co-BMA) with 50 mol% BMA and 50 mol% DMAEMA were made according to our previously published methods[47] using palmitoylated siRNA.[49,57] For luciferase studies, mice (5 *per* group, n=10 tumors) were injected with 1 mg/kg siRNA against luciferase or scrambled control siRNA *via* the tail vein. To measure luminescence, mice were injected with 15 mg/kg luciferin i.p. and imaged the day of and at 24 h after siRNA treatment using an IVS imaging system (Caliper Life Sciences, Waltham, MA). For Gal8 studies, mice were injected with *in vivo* formulations of polyplex at 1 mg/kg siRNA or an equal volume saline injection. Tumors were explanted into ice cold PBS following euthanasia 18 h post injection. The tumors were bisected with a razor blade, and immediately subjected to confocal imaging. Seven to eleven images were taken *per* tumor and averaged; each plotted point represents the average data for one tumor, and 8 tumors were analyzed *per* group.

3.5.17 Statistical Methods

Data were analyzed and plotted using Microsoft Excel, Prism GraphPad 6, and MathWorks MATLAB R2016a. Lines of best fit for Figure 3.1 were generated through a linear fit in GraphPad; both lines have statistically significant non-zero slope ($p < 0.05$). Luciferase activity and toxicity data for the composition library were tested using one-way ANOVA in GraphPad with Dunnett's post hoc testing against PBS. For the MW library: cytotoxicity, luciferase activity, Manders coefficient, and Gal8 recruitment were tested using two-way ANOVA with no sample matching in GraphPad Prism. Where noted, post-hoc analysis was

performed using Tukey's multiple comparisons test to calculate corrected p values for multiple comparisons, while Dunnett's post-hoc test was used for significant differences relative to control in GraphPad Prism. All two-way ANOVA data presented are statistically significant at the dataset level ($p<0.001$) for polymer, dose, and interaction thereof. For Figure 3.6A-C, data were plotted using dose matched datasets; for **Figure 3.6D**, knockdown data at the 3 doses were plotted against hemolysis. Spearman correlation coefficients and two tailed p values were generated using GraphPad Prism; for hemolysis data, this calculation was done for each dose individually against hemolysis, and as a whole. For **Figure 3.6,** hyperbolic lines of best fit were calculated using GraphPad Prism; best fit models did not converge for **Figure 3.6B and 6D**. Correlations were calculated independently of lines of best fit. For *in vivo* experiments (**Figure 3.7**), *p* values were calculated using two-sided t tests without pairing for luciferase knockdown data, while Gal8 recruitment data were analyzed with two side Mann-Whitney testing without pairing, which was chosen due to statistically significant deviation of negative control data from normal distribution by testing with the D'Agostino & Pearson omnibus normality test ($p < 0.05$) as calculated in GraphPad Prism. The threshold of statistical significance, α, was set to 0.05 throughout this work. Signal-to-noise, signal-to-background, and Z′-factor calculations were carried out as described by Zhang *et al.*[50] using the maximal response polymer condition (50 nM, 50B-XL) as an estimated positive control for the range of the assay.

3.6 Acknowledgements

This work was supported by the United States National Institutes of Health grants R01HL122347, R01EB019409, and R01CA224241 and Department of Defense CDMRP W81XWH-14-1-0298 to CLD, National Science Foundation Graduate Research Fellowship to

KVK, TAW, MAJ, and SKB (0909667 and 1445197), and Vanderbilt SyBBURE Searle Undergraduate Research Program funding to SCD. Dynamic light scattering was conducted at the Vanderbilt Institute of Nanoscale Sciences and Engineering. Flow cytometry experiments were performed in the Vanderbilt University Medical Center Flow Cytometry Shared Resource, supported by the Vanderbilt Ingram Cancer Center (P30 CA68485) and the Vanderbilt Digestive Disease Research Center (DK058404). Electron Microscopy was performed were performed through the use of the VU Cell Imaging Shared Resource (supported by NIH grants CA68485, DK20593, DK58404, DK59637 and EY08126). We are thankful for electron microscopy assistance and expertise from J. Williams and for gifts of plasmids from F. Randow and R. Weinberg.

3.7 References

(1) Stein, C. A.; Castanotto, D. FDA-Approved Oligonucleotide Therapies in 2017. *Mol. Ther.* **2017**, *25*, 1069–1075.

(2) Akcea Therapeutics Press Release. Akcea and Ionis Receive FDA Approval of TEGSEDI™ (inotersen) for the Treatment of the Polyneuropathy of Hereditary Transthyretin-Mediated Amyloidosis in Adults https://ir.akceatx.com/news-releases/news-release-details/akcea-and-ionis-receive-fda-approval-tegseditm-inotersen (accessed Oct 25, 2018).

(3) Mullard, A. FDA Approves Landmark RNAi Drug. *Nat. Rev. Drug Discov.* **2018**, *17*, 613–613.

(4) Yin, H.; Kanasty, R. L.; Eltoukhy, A. A.; Vegas, A. J.; Dorkin, J. R.; Anderson, D. G. Non-Viral Vectors for Gene-Based Therapy. *Nat. Rev. Genet.* **2014**, *15*, 541–555.

(5) Dowdy, S. F. Overcoming Cellular Barriers for RNA Therapeutics. *Nat. Biotechnol.* **2017**, *35*, 222–229.

(6) Whitehead, K. A.; Langer, R.; Anderson, D. G. Knocking Down Barriers: Advances in siRNA Delivery. *Nat. Rev. Drug Discov.* **2009**, *8*, 129–138.

(7) Pack, D. W.; Hoffman, A. S.; Pun, S.; Stayton, P. S. Design and Development of Polymers for Gene Delivery. *Nat. Rev. Drug Discov.* **2005**, *4*, 581–593.

(8) Varkouhi, A. K.; Scholte, M.; Storm, G.; Haisma, H. J. Endosomal Escape Pathways for Delivery of Biologicals. *J. Control. Release* **2011**, *151*, 220–228.

(9) Belting, M.; Sandgren, S.; Wittrup, A. Nuclear Delivery of Macromolecules: Barriers and Carriers. *Adv. Drug Deliv. Rev.* **2005**, *57*, 505–527.

(10) Akishiba, M.; Takeuchi, T.; Kawaguchi, Y.; Sakamoto, K.; Yu, H. H.; Nakase, I.;

Takatani-Nakase, T.; Madani, F.; Gräslund, A.; Futaki, S. Cytosolic Antibody Delivery by Lipid-Sensitive Endosomolytic Peptide. *Nat. Chem.* **2017**, *9*, 751–761.

(11) Li, H.; E. Nelson, C.; C. Evans, B.; L. Duvall, C. Delivery of Intracellular-Acting Biologics in Pro-Apoptotic Therapies. *Curr. Pharm. Des.* **2011**, *17*, 293–319.

(12) Kim, H.; Lee, D.; Kim, J.; Kim, T.; Kim, W. J. Photothermally Triggered Cytosolic Drug Delivery *via* Endosome Disruption Using a Functionalized Reduced Graphene Oxide. *ACS Nano* **2013**, *7*, 6735–6746.

(13) Sonawane, N. D.; Szoka, F. C.; Verkman, A. S. Chloride Accumulation and Swelling in Endosomes Enhances DNA Transfer by Polyamine-DNA Polyplexes. *J. Biol. Chem.* **2003**, *278*, 44826–44831.

(14) Gilleron, J.; Querbes, W.; Zeigerer, A.; Borodovsky, A.; Marsico, G.; Schubert, U.; Manygoats, K.; Seifert, S.; Andree, C.; Stöter, M.; Epstein-Barash, H.; Zhang, L.; Koteliansky, V.; Fitzgerald, K.; Fava, E.; Bickle, M.; Kalaidzidis, Y.; Akinc, A.; Maier, M.; Zerial, M. Image-Based Analysis of Lipid Nanoparticle-Mediated siRNA Delivery, Intracellular Trafficking and Endosomal Escape. *Nat. Biotechnol.* **2013**, *31*, 638–646.

(15) Vermeulen, L. M. P.; Brans, T.; Samal, S. K.; Dubruel, P.; Demeester, J.; De Smedt, S. C.; Remaut, K.; Braeckmans, K. Endosomal Size and Membrane Leakiness Influence Proton Sponge-Based Rupture of Endosomal Vesicles. *ACS Nano* **2018**, *12*, 2332–2345.

(16) Berguig, G. Y.; Convertine, A. J.; Shi, J.; Palanca-Wessels, M. C.; Duvall, C. L.; Pun, S. H.; Press, O. W.; Stayton, P. S. Intracellular Delivery and Trafficking Dynamics of a Lymphoma-Targeting Antibody-Polymer Conjugate. *Mol. Pharm.* **2012**, *9*, 3506–3514.

(17) Medina-Kauwe, L. K.; Xie, J.; Hamm-Alvarez, S. Intracellular Trafficking of Nonviral Vectors. *Gene Ther.* **2005**, *12*, 1734–1751.

(18) Tamura, A.; Oishi, M.; Nagasaki, Y. Enhanced Cytoplasmic Delivery of siRNA Using a Stabilized Polyion Complex Based on PEGylated Nanogels with a Cross-Linked Polyamine Structure. *Biomacromolecules* **2009**, *10*, 1818–1827.

(19) Sakurai, Y.; Hatakeyama, H.; Sato, Y.; Akita, H.; Takayama, K.; Kobayashi, S.; Futaki, S.; Harashima, H. Endosomal Escape and the Knockdown Efficiency of Liposomal-siRNA by the Fusogenic Peptide ShGALA. *Biomaterials* **2011**, *32*, 5733–5742.

(20) Nelson, C. E.; Kintzing, J. R.; Hanna, A.; Shannon, J. M.; Gupta, M. K.; Duvall, C. L. Balancing Cationic and Hydrophobic Content of PEGylated siRNA Polyplexes Enhances Endosome Escape, Stability, Blood Circulation Time, and Bioactivity *in Vivo*. *ACS Nano* **2013**, *7*, 8870–8880.

(21) Basha, G.; Novobrantseva, T. I.; Rosin, N.; Tam, Y. Y. C.; Hafez, I. M.; Wong, M. K.; Sugo, T.; Ruda, V. M.; Qin, J.; Klebanov, B.; Ciufolini, M.; Akinc, A.; Tam, Y. K.; Hope, M. J.; Cullis, P. R. Influence of Cationic Lipid Composition on Gene Silencing Properties of Lipid Nanoparticle Formulations of siRNA in Antigen-Presenting Cells. *Mol. Ther.* **2011**, *19*, 2186–2200.

(22) Hughes, L. D.; Rawle, R. J.; Boxer, S. G.; Doose, S.; Heilemann, M. Choose Your Label Wisely: Water-Soluble Fluorophores Often Interact with Lipid Bilayers. *PLoS One* **2014**, *9*, e87649.

(23) Swiecicki, J. M.; Thiebaut, F.; Di Pisa, M.; Gourdin-Bertin, S.; Tailhades, J.; Mansuy, C.; Burlina, F.; Chwetzoff, S.; Trugnan, G.; Chassaing, G.; Lavielle, S. How to Unveil Self-Quenched Fluorophores and Subsequently Map the Subcellular Distribution of Exogenous Peptides. *Sci. Rep.* **2016**, *6*, 20237.

(24) Gruber, H. J.; Hahn, C. D.; Kada, G.; Riener, C. K.; Harms, G. S.; Ahrer, W.; Dax, T. G.;

Knaus, H. G. Anomalous Fluorescence Enhancement of Cy3 and Cy3.5 *versus* Anomalous Fluorescence Loss of Cy5 and Cy7 upon Covalent Linking to IgG and Noncovalent Binding to Avidin. *Bioconjug. Chem.* **2000**, *11*, 696–704.

(25) Behr, J. The Proton Sponge: A Trick to Enter Cells the Viruses Did Not Exploit. *Chim. Int. J. Chem.* **1997**, *2*, 34–36.

(26) Martens, T. F.; Remaut, K.; Demeester, J.; De Smedt, S. C.; Braeckmans, K. Intracellular Delivery of Nanomaterials: How to Catch Endosomal Escape in the Act. *Nano Today* **2014**, *9*, 344–364.

(27) Zelphati, O.; Szoka, F. C. Mechanism of Oligonucleotide Release from Cationic Liposomes. *Proc. Natl. Acad. Sci. U. S. A.* **1996**, *93*, 11493–11498.

(28) Richard, J. P.; Melikov, K.; Vives, E.; Ramos, C.; Verbeure, B.; Gait, M. J.; Chernomordik, L. V; Lebleu, B. Cell-Penetrating Peptides. A Reevaluation of the Mechanism of Cellular Uptake. *J. Biol. Chem.* **2003**, *278*, 585–590.

(29) Kilchrist, K. V.; Evans, B. C.; Brophy, C. M.; Duvall, C. L. Mechanism of Enhanced Cellular Uptake and Cytosolic Retention of MK2 Inhibitory Peptide Nano-Polyplexes. *Cell. Mol. Bioeng.* **2016**, *9*, 368–381.

(30) Evans, B. C.; Hocking, K. M.; Kilchrist, K. V.; Wise, E. S.; Brophy, C. M.; Duvall, C. L. Endosomolytic Nano-Polyplex Platform Technology for Cytosolic Peptide Delivery to Inhibit Pathological Vasoconstriction. *ACS Nano* **2015**, *9*, 5893–5907.

(31) Liu, X.; Fagotto, F. A Method to Separate Nuclear, Cytosolic, and Membrane-Associated Signaling Molecules in Cultured Cells. *Sci. Signal.* **2011**, *4*, pl2.

(32) Shi, J.; Chou, B.; Choi, J. L.; Ta, A. L.; Pun, S. H. Investigation of Polyethylenimine/DNA Polyplex Transfection to Cultured Cells Using Radiolabeling and Subcellular

Fractionation Methods. *Mol. Pharm.* **2013**, *10*, 2145–2156.

(33) Cohen, R. N.; van der Aa, M. A. E. M.; Macaraeg, N.; Lee, A. P.; Szoka, F. C. Quantification of Plasmid DNA Copies in the Nucleus after Lipoplex and Polyplex Transfection. *J. Control. Release* **2009**, *135*, 166–174.

(34) Hadari, Y. R.; Paz, K.; Dekel, R.; Mestrovic, T.; Accili, D.; Zick, Y. Galectin-8. A New Rat Lectin, Related to Galectin-4. *J. Biol. Chem.* **1995**, *270*, 3447–3453.

(35) Thurston, T. L. M.; Wandel, M. P.; Von Muhlinen, N.; Foeglein, Á.; Randow, F. Galectin 8 Targets Damaged Vesicles for Autophagy to Defend Cells against Bacterial Invasion. *Nature* **2012**, *482*, 414–418.

(36) Maier, O.; Marvin, S. A.; Wodrich, H.; Campbell, E. M.; Wiethoff, C. M. Spatiotemporal Dynamics of Adenovirus Membrane Rupture and Endosomal Escape. *J. Virol.* **2012**, *86*, 10821–10828.

(37) Wittrup, A.; Ai, A.; Liu, X.; Hamar, P.; Trifonova, R.; Charisse, K.; Manoharan, M.; Kirchhausen, T.; Lieberman, J. Visualizing Lipid-Formulated siRNA Release from Endosomes and Target Gene Knockdown. *Nat. Biotechnol.* **2015**, *33*, 870–876.

(38) Perlman, Z. E.; Slack, M. D.; Feng, Y.; Mitchison, T. J.; Wu, L. F.; Altschuler, S. J. Multidimensional Drug Profiling by Automated Microscopy. *Science* **2004**, *306*, 1194–1198.

(39) Mitchison, T. J. Small-Molecule Screening and Profiling by Using Automated Microscopy. *ChemBioChem* **2005**, *6*, 33–39.

(40) Pepperkok, R.; Ellenberg, J. High-Throughput Fluorescence Microscopy for Systems Biology. *Nat. Rev. Mol. Cell Biol.* **2006**, *7*, 690–696.

(41) Conrad, C.; Gerlich, D. W. Automated Microscopy for High-Content RNAi Screening. *J.*

Cell Biol. 2010, pp 453–461.

(42) de Groot, R.; Lüthi, J.; Lindsay, H.; Holtackers, R.; Pelkmans, L. Large-Scale Image-Based Profiling of Single-Cell Phenotypes in Arrayed CRISPR-Cas9 Gene Perturbation Screens. *Mol. Syst. Biol.* **2018**, *14*, e8064.

(43) Werfel, T. A.; Jackson, M. A.; Kavanaugh, T. E.; Kirkbride, K. C.; Miteva, M.; Giorgio, T. D.; Duvall, C. Combinatorial Optimization of PEG Architecture and Hydrophobic Content Improves Ternary siRNA Polyplex Stability, Pharmacokinetics, and Potency *in Vivo*. *J. Control. Release* **2017**, *255*, 12–26.

(44) Siegwart, D. J.; Whitehead, K. A.; Nuhn, L.; Sahay, G.; Cheng, H.; Jiang, S.; Ma, M.; Lytton-Jean, A.; Vegas, A.; Fenton, P.; Levins, C. G.; Love, K. T.; Lee, H.; Cortez, C.; Collins, S. P.; Li, Y. F.; Jang, J.; Querbes, W.; Zurenko, C.; Novobrantseva, T.; *et al*. Combinatorial Synthesis of Chemically Diverse Core-Shell Nanoparticles for Intracellular Delivery. *Proc. Natl. Acad. Sci. U. S. A.* **2011**, *108*, 12996–13001.

(45) Green, J. J.; Langer, R.; Anderson, D. G. A Combinatorial Polymer Library Approach Yields Insight into Nonviral Gene Delivery. *Acc. Chem. Res.* **2008**, *41*, 749–759.

(46) Akinc, A.; Zumbuehl, A.; Goldberg, M.; Leshchiner, E. S.; Busini, V.; Hossain, N.; Bacallado, S. A.; Nguyen, D. N.; Fuller, J.; Alvarez, R.; Borodovsky, A.; Borland, T.; Constien, R.; de Fougerolles, A.; Dorkin, J. R.; Narayanannair Jayaprakash, K.; Jayaraman, M.; John, M.; Koteliansky, V.; Manoharan, M.; *et al*. A Combinatorial Library of Lipid-like Materials for Delivery of RNAi Therapeutics. *Nat. Biotechnol.* **2008**, *26*, 561–569.

(47) Jackson, M. A.; Werfel, T. A.; Curvino, E. J.; Yu, F.; Kavanaugh, T. E.; Sarett, S. M.; Dockery, M. D.; Kilchrist, K. V.; Jackson, A. N.; Giorgio, T. D.; Duvall, C. L.

Zwitterionic Nanocarrier Surface Chemistry Improves siRNA Tumor Delivery and Silencing Activity Relative to Polyethylene Glycol. *ACS Nano* **2017**, *11*, 5680–5696.

(48) Beavers, K. R.; Werfel, T. A.; Shen, T.; Kavanaugh, T. E.; Kilchrist, K. V.; Mares, J. W.; Fain, J. S.; Wiese, C. B.; Vickers, K. C.; Weiss, S. M.; Duvall, C. L. Porous Silicon and Polymer Nanocomposites for Delivery of Peptide Nucleic Acids as Anti-MicroRNA Therapies. *Adv. Mater.* **2016**, *28*, 7984–7992.

(49) Sarett, S. M.; Werfel, T. A.; Chandra, I.; Jackson, M. A.; Kavanaugh, T. E.; Hattaway, M. E.; Giorgio, T. D.; Duvall, C. L. Hydrophobic Interactions between Polymeric Carrier and Palmitic Acid-Conjugated siRNA Improve PEGylated Polyplex Stability and Enhance *in Vivo* Pharmacokinetics and Tumor Gene Silencing. *Biomaterials* **2016**, *97*, 122–132.

(50) Zhang, J. H.; Chung, T. D. Y.; Oldenburg, K. R. A Simple Statistical Parameter for Use in Evaluation and Validation of High Throughput Screening Assays. *J. Biomol. Screen.* **1999**, *4*, 67–73.

(51) Evans, B. C.; Nelson, C. E.; Yu, S. S.; Beavers, K. R.; Kim, A. J.; Li, H.; Nelson, H. M.; Giorgio, T. D.; Duvall, C. L. *Ex Vivo* Red Blood Cell Hemolysis Assay for the Evaluation of pH-Responsive Endosomolytic Agents for Cytosolic Delivery of Biomacromolecular Drugs. *J. Vis. Exp.* **2013**, No. 73, 50166.

(52) Evans, B. C.; Hocking, K. M.; Osgood, M. J.; Voskresensky, I.; Dmowska, J.; Kilchrist, K. V.; Brophy, C. M.; Duvall, C. L. MK2 Inhibitory Peptide Delivered in Nanopolyplexes Prevents Vascular Graft Intimal Hyperplasia. *Sci. Transl. Med.* **2015**, *7*, 291ra95.

(53) Manders, E. M. M.; Verbeek, F. J.; Aten, J. A. Measurement of Co-Localization of Objects in Dual-Colour Confocal Images. *J. Microsc.* **1993**, *169*, 375–382.

(54) Klumperman, J.; Raposo, G. The Complex Ultrastructure of the Endolysosomal System.

Cold Spring Harb. Perspect. Biol. **2014**, *6*, a016857.

(55) Nelson, C. E.; Kim, A. J.; Adolph, E. J.; Gupta, M. K.; Yu, F.; Hocking, K. M.; Davidson, J. M.; Guelcher, S. A.; Duvall, C. L. Tunable Delivery of siRNA from a Biodegradable Scaffold to Promote Angiogenesis *in Vivo*. *Adv. Mater.* **2014**, *26*, 607–614.

(56) Martin, J. R.; Nelson, C. E.; Gupta, M. K.; Yu, F.; Sarett, S. M.; Hocking, K. M.; Pollins, A. C.; Nanney, L. B.; Davidson, J. M.; Guelcher, S. A.; Duvall, C. L. Local Delivery of PHD2 siRNA from ROS-Degradable Scaffolds to Promote Diabetic Wound Healing. *Adv. Healthc. Mater.* **2016**, *5*, 2751–2757.

(57) Sarett, S. M.; Kilchrist, K. V.; Miteva, M.; Duvall, C. L. Conjugation of Palmitic Acid Improves Potency and Longevity of siRNA Delivered *via* Endosomolytic Polymer Nanoparticles. *J. Biomed. Mater. Res. - Part A* **2015**, *103*, 3107–3116.

(58) Jain, R. K.; Stylianopoulos, T. Delivering Nanomedicine to Solid Tumors. *Nature Reviews Clinical Oncology*. November 14, 2010, pp 653–664.

(59) Yuan, F.; Dellian, M.; Fukumura, D.; Leunig, M.; Berk, D. A.; Torchilin, V. P.; Jain, R. K. Vascular Permeability in a Human Tumor Xenograft: Molecular Size Dependence and Cutoff Size. *Cancer Res.* **1995**, *55*, 3752–3757.

(60) Yuan, F.; Leunig, M.; Huang, S. K.; Berk, D. A.; Papahadjopoulos, D.; Jam, R. K. Mirovascular Permeability and Interstitial Penetration of Sterically Stabilized (Stealth) Liposomes in a Human Tumor Xenograft. *Cancer Res.* **1994**, *54*, 3352–3356.

(61) Mathew, R.; Karantza-Wadsworth, V.; White, E. Role of Autophagy in Cancer. *Nat. Rev. Cancer* **2007**, *7*, 961–967.

(62) White, E. The Role for Autophagy in Cancer. *J. Clin. Invest.* **2015**, *125* (1), 42–46.

(63) Li, S.; Wandel, M. P.; Li, F.; Liu, Z.; He, C.; Wu, J.; Shi, Y.; Randow, F. Sterical

Hindrance Promotes Selectivity of the Autophagy Cargo Receptor NDP52 for the Danger Receptor Galectin-8 in Antibacterial Autophagy. *Sci. Signal.* **2013**, *6*, ra9.

(64) Kim, B. W.; Beom Hong, S.; Hoe Kim, J.; Hoon Kwon, D.; Song, H. K. Structural Basis for Recognition of Autophagic Receptor NDP52 by the Sugar Receptor Galectin-8. *Nat. Commun.* **2013**, *4*, 1613.

(65) Feng, Y.; He, D.; Yao, Z.; Klionsky, D. J. The Machinery of Macroautophagy. *Cell Res.* **2014**, *24*, 24–41.

(66) Gupta, B.; Levchenko, T. S.; Torchilin, V. P. Intracellular Delivery of Large Molecules and Small Particles by Cell-Penetrating Proteins and Peptides. *Adv. Drug Deliv. Rev.* **2005**, *57*, 637–651.

(67) Lim, S. I.; Lukianov, C. I.; Champion, J. A. Self-Assembled Protein Nanocarrier for Intracellular Delivery of Antibody. *J. Control. Release* **2017**, *249*, 1–10.

(68) Lönn, P.; Kacsinta, A. D.; Cui, X.-S.; Hamil, A. S.; Kaulich, M.; Gogoi, K.; Dowdy, S. F. Enhancing Endosomal Escape for Intracellular Delivery of Macromolecular Biologic Therapeutics. *Sci. Rep.* **2016**, *6*, 32301.

(69) Convertine, A. J.; Benoit, D. S. W.; Duvall, C. L.; Hoffman, A. S.; Stayton, P. S. Development of a Novel Endosomolytic Diblock Copolymer for siRNA Delivery. *J. Control. Release* **2009**, *133*, 221–229.

(70) Kilchrist, K. V. Galectin 8 Recruitment Analysis MATLAB Software. *FigShare* **2018**, (doi: 10.6084/m9.figshare.7066472).

(71) Kilchrist, K. V. Manders Coefficient of Overlap Calculation Analysis MATLAB Software. *FigShare* **2018**, (doi: 10.6084/m9.figshare.7066490).

3.8 Supplemental Information

S1: PEG-b-(DMAEMA-co-BMA) Polymer Synthesis Scheme

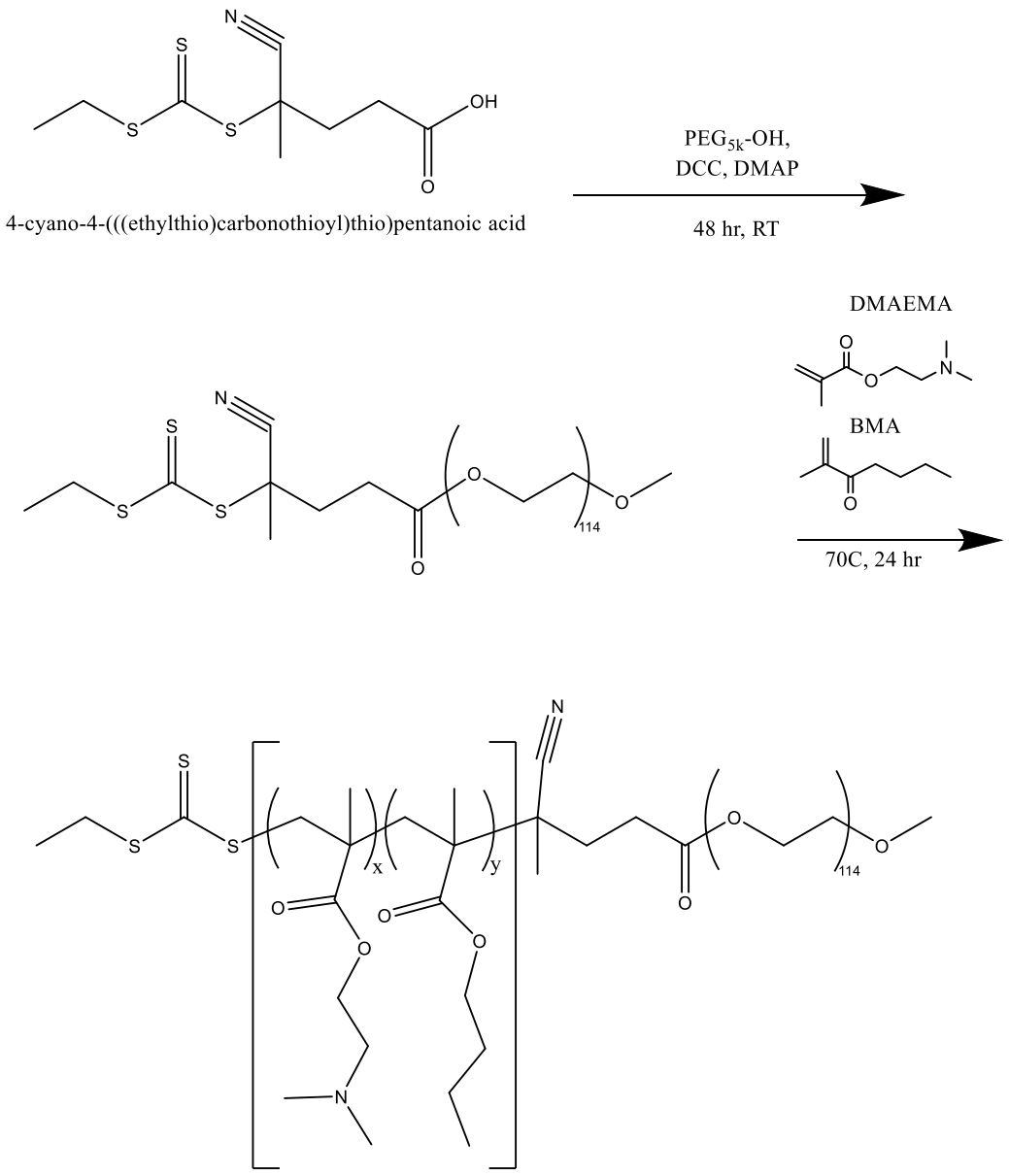

Reaction scheme 1. Synthesis of PEG macro CTA for RAFT synthesis.

S2: 50B Molecular Weight Library, Viability Data

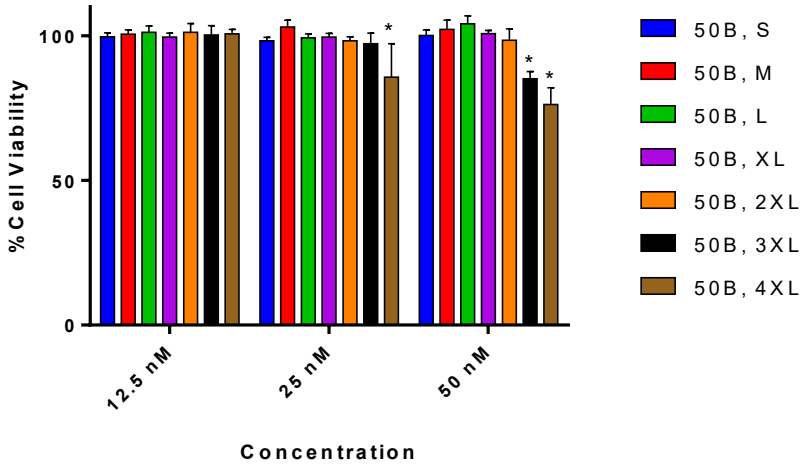

Figure S2: Formulations nontoxic, except modest toxicity for largest polymers and highest doses. Cells treated at indicated doses and assayed according to CellTiterGlo instructions.

S2: Gal8 Image Processing Pipeline

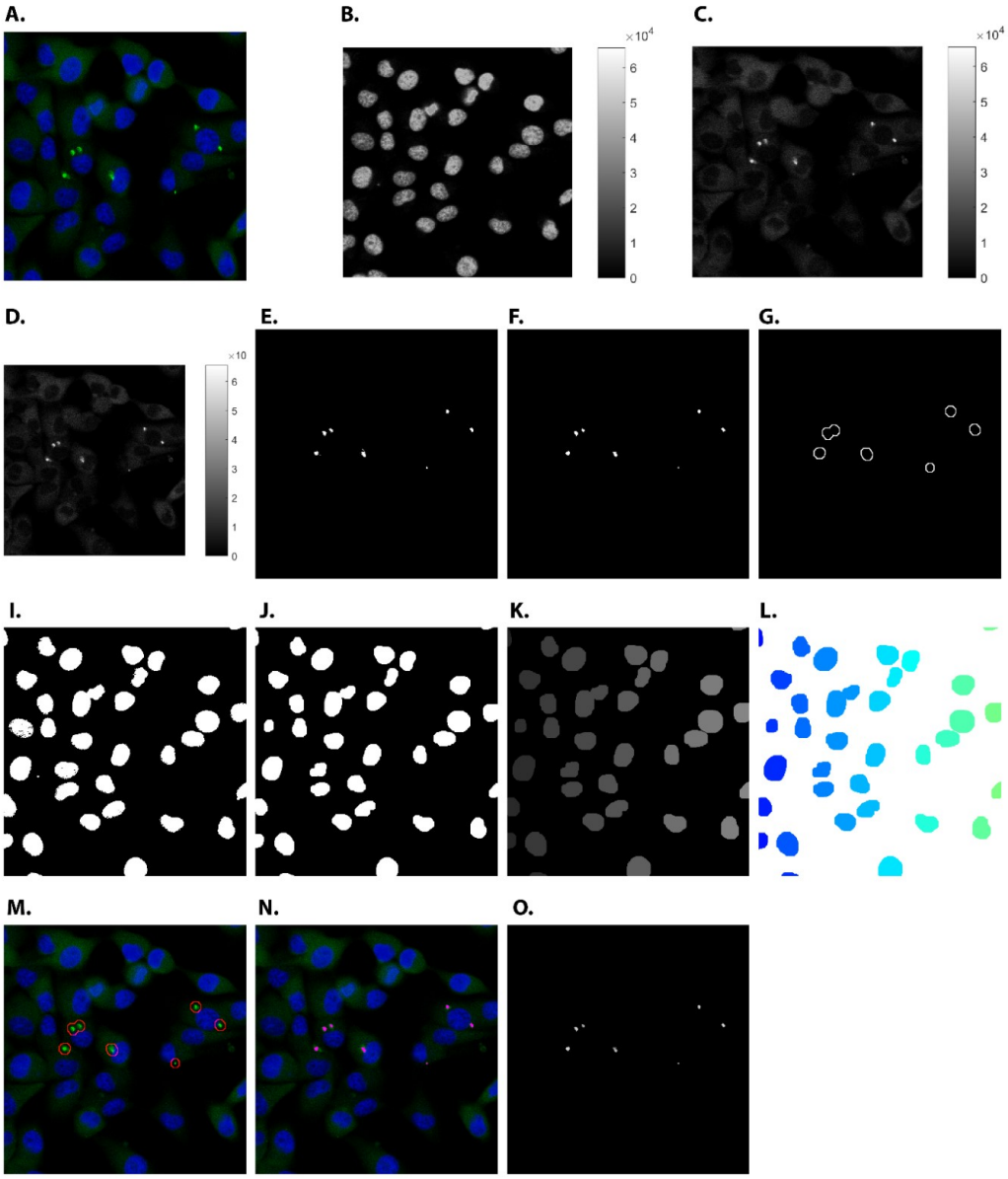

A: Original composite micrograph
B: Nuclear stain channel
C: Gal8 channel
D: Gal8 following tophat filter of *C*
E: Simple threshold of *D* to identify positive pixels
F: Morphological opening of *E*
G: Annotation layer generated using *E*, denoting positive spots
I: Simple threshold of B
J: Morphological opening of *I* to separate proximal nuclei
K: Watershed transform of *J*
L: Rainbow colormap applied to *K*
M: Exported composite, with annotations (red)
N: Exported composite, false color "positive spots" (red)
O: Binary mask of "positive spots"

S4: Full size image of Figure 5B1, showing AuNP treated control

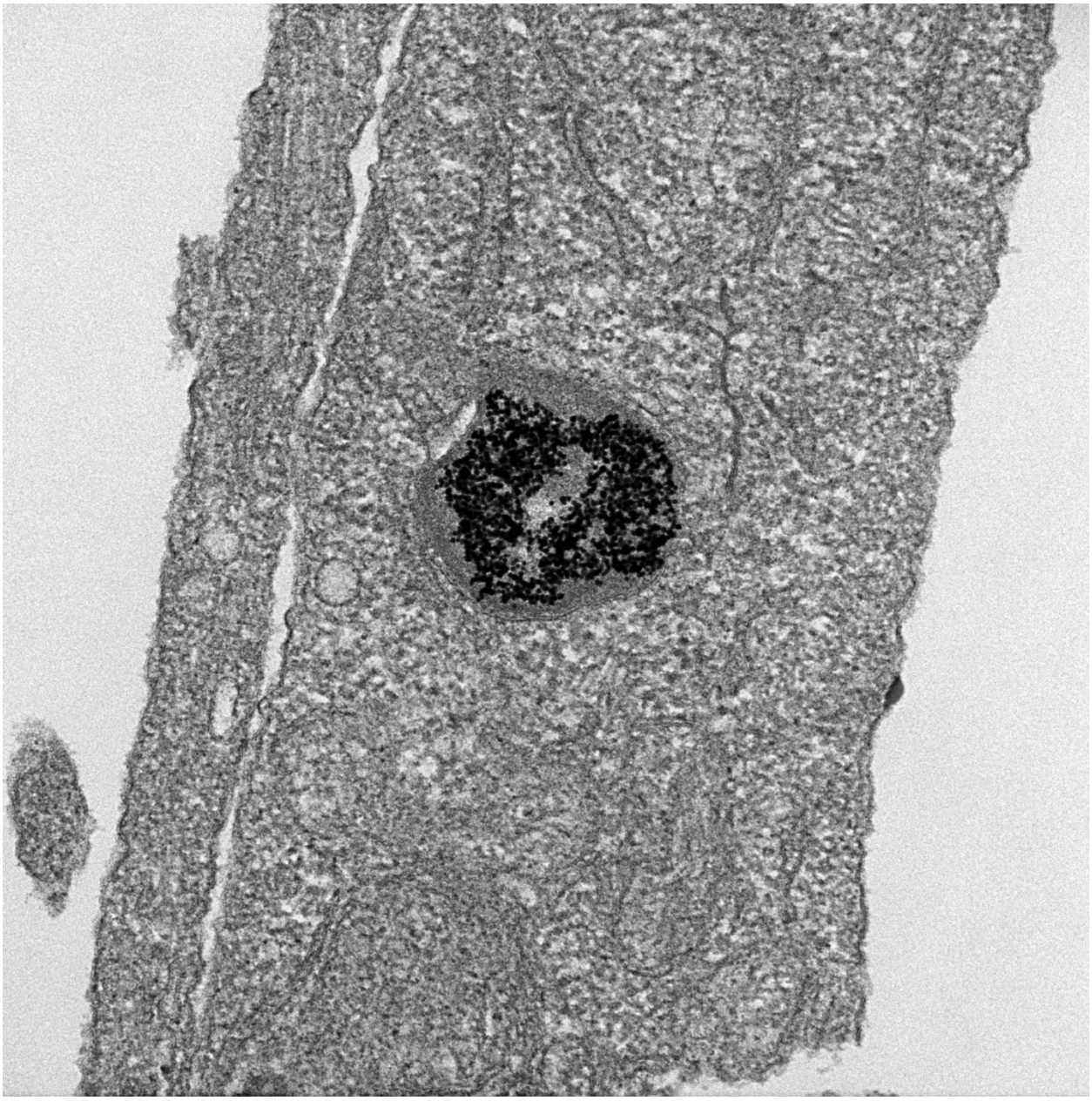

S5: Full size image of Figure 5B2, showing AuNP/50B-S treated cells

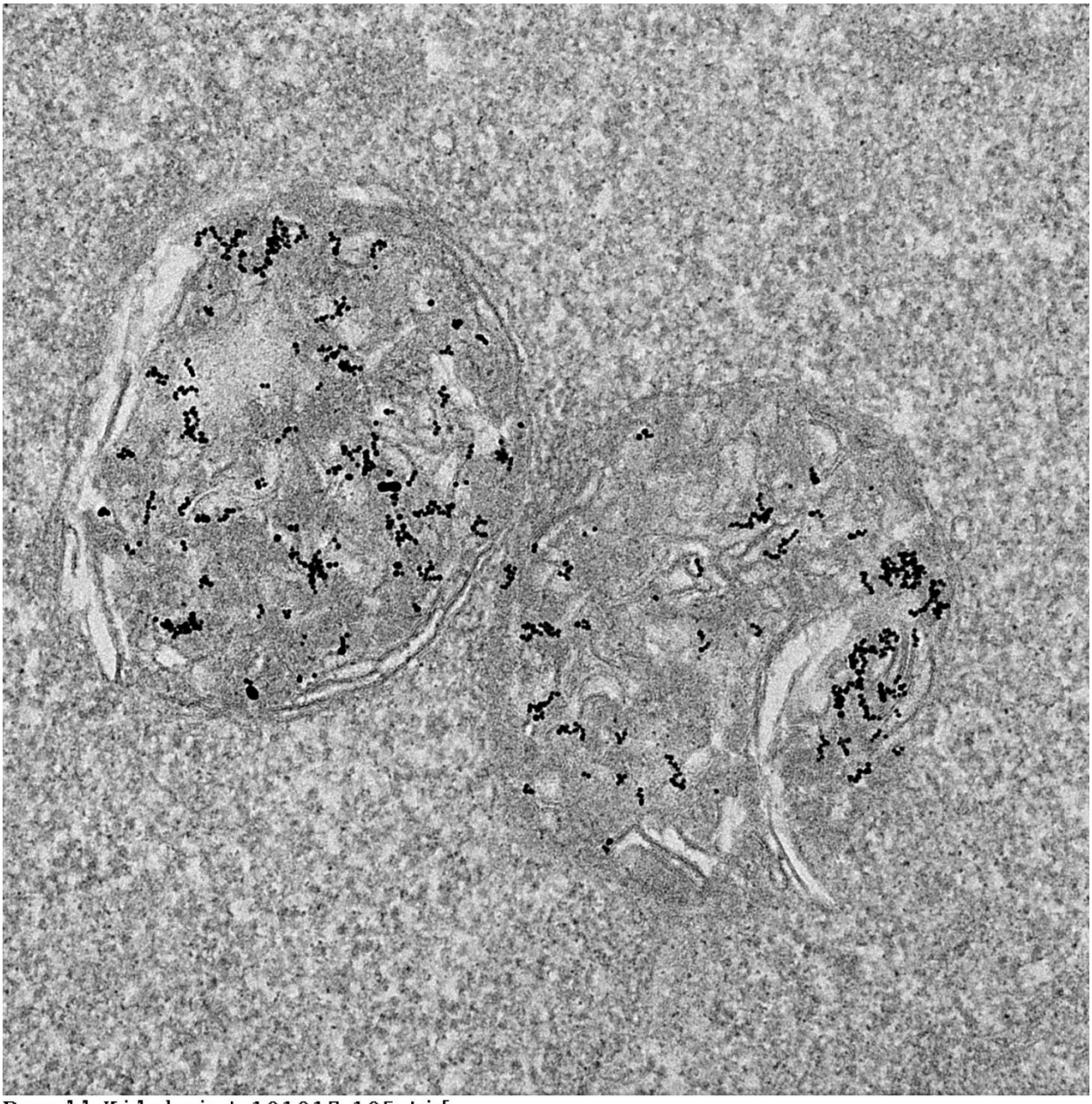

S6: Full size image of Figure 5B3, showing AuNP/50B-L treated cells

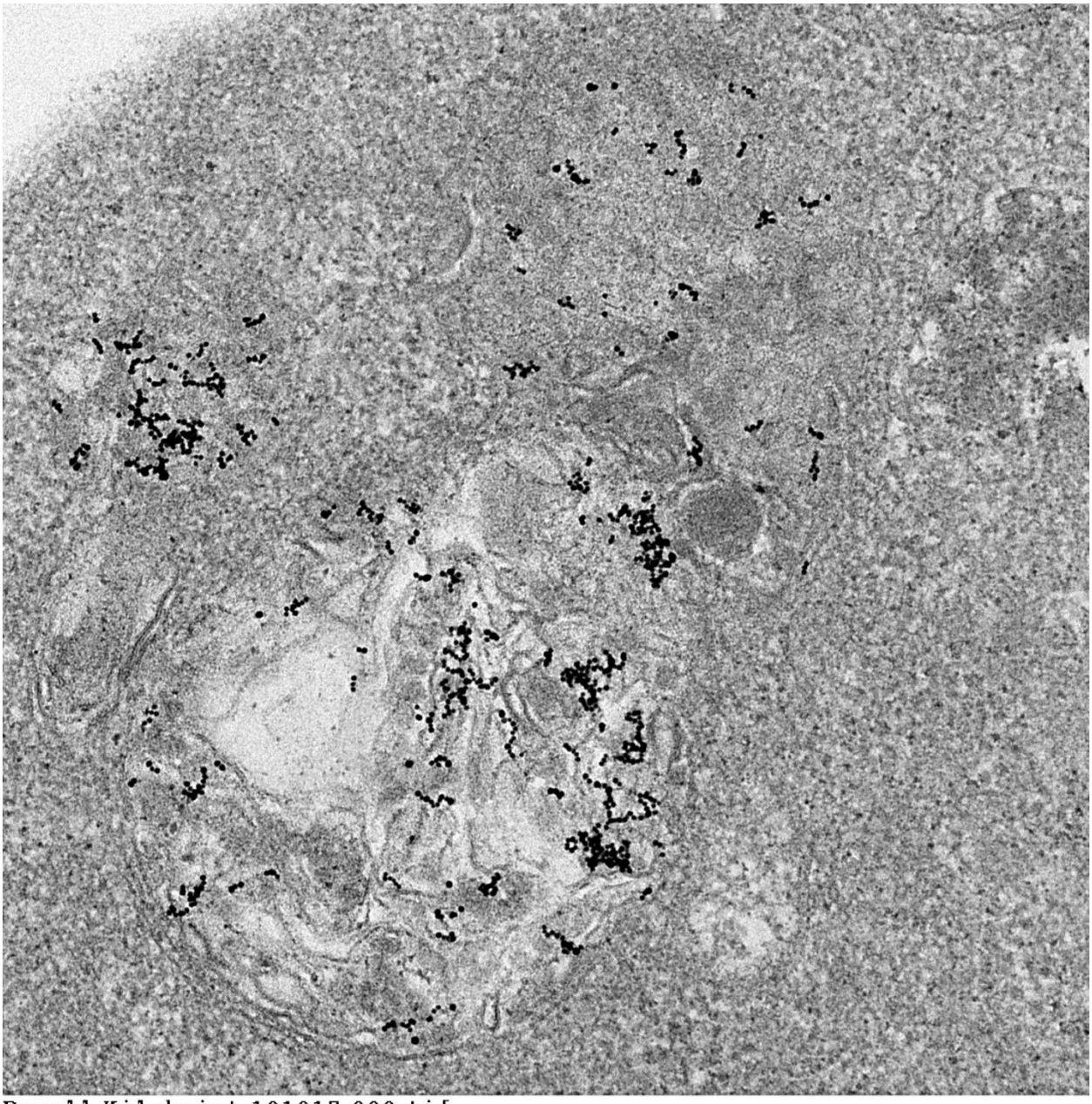

S7: Full size image of Figure 5B4, showing AuNP/50B-4XL treated cells

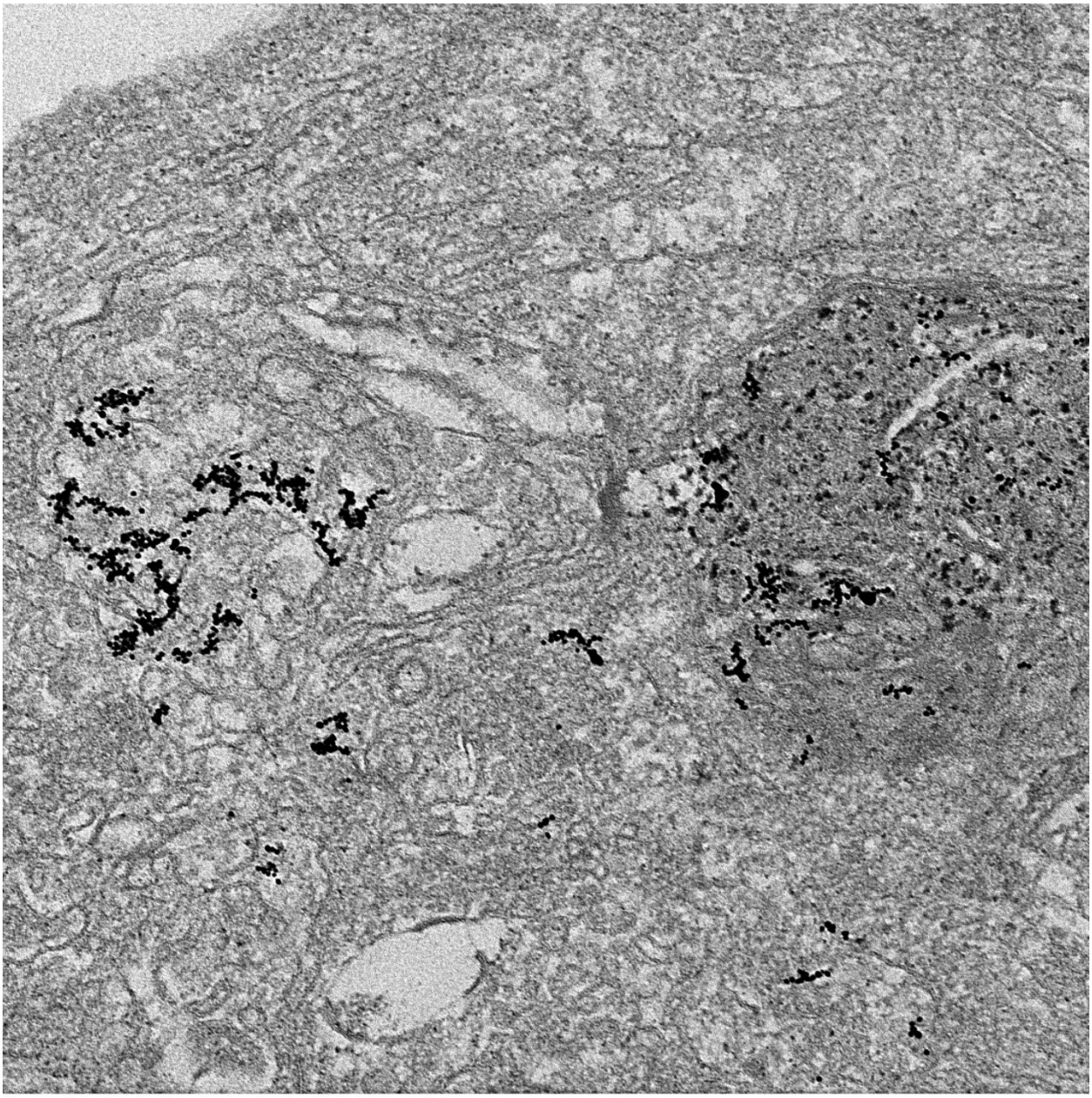

S8: Cellular uptake of siRNA in 50B Molecular Weight Library

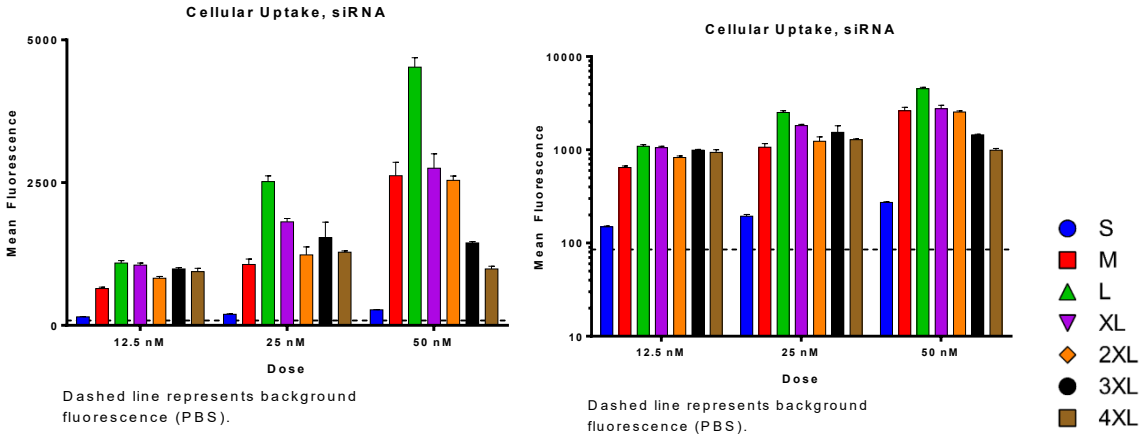

Mean fluorescence intensity was measured using flow cytometry at 12.5, 25, and 50 nM doses of Alexa-488 dsDNA in polyplexes and plotted on both linear (left) and log (right) scales. Cells treated with buffer produced fluorescence represented by the dotted line.

S9: Polymer molecular weight correlates with luciferase knockdown in 50B MW library

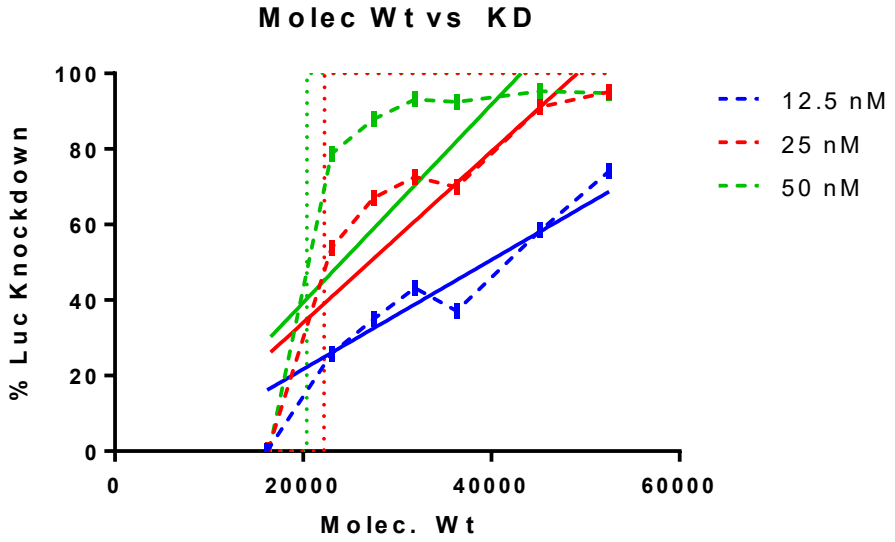

Polymer molecular weights correlate strongly with gene knockdown data at 12.5 nM (blue circles), 25 nM (red squares), and 50 nM (green triangles). These correlations are statistically significant by Spearman's method. Solid line indicates simple linear regression. Dashed line connects adjacent datapoints. Dotted lines represent the sigmoidal best fit, constrained with plateaus at 0% and 100%.

All three doses produce ~0 knockdown at the 16300 g/mol MW. Likewise, 50 and 25 nM doses overlap at the largest MW, 52500 g/mol.

Due to non-linear effects which become increasingly apparent at high doses (maximal knockdown of 100%, ~0% knockdown for all molecular weights below ~16500 g/mol), the 95% confidence interval for the slope of the linear regression for 50 nM does not exclude 0 slope, representing saturation of the assay as mentioned in the text.

A sigmoidal curve is likely the most appropriate model for such a system with constraints at both the low (=0%) and high (=100%) end, but the best fit to this model does not converge for the 12.5 nM dose, while for the 25 and 50 nM doses it produces an ambiguous response. Still, such a fit suggests a Log EC50 of 22237 and 20395 MW for 25 and 50 nM, respectively, suggesting polymers below these molecular weights may not be useful for gene knockdown. There may be interesting nonlinear polymer effects in this range of molecular weights.

Statistics for Fig S9:

	KD, 12.5 nM		KD, 25 nM		KD, 50 nM	
	r	*p*	*r*	*p*	*r*	*p*
Molec Weight	0.96	0.003	0.96	0.003	0.93	0.007

S10: Gal8 Recruitment Correlates to Gene Knockdown in Immortalized Rat Smooth Muscle Cells (A7r5)

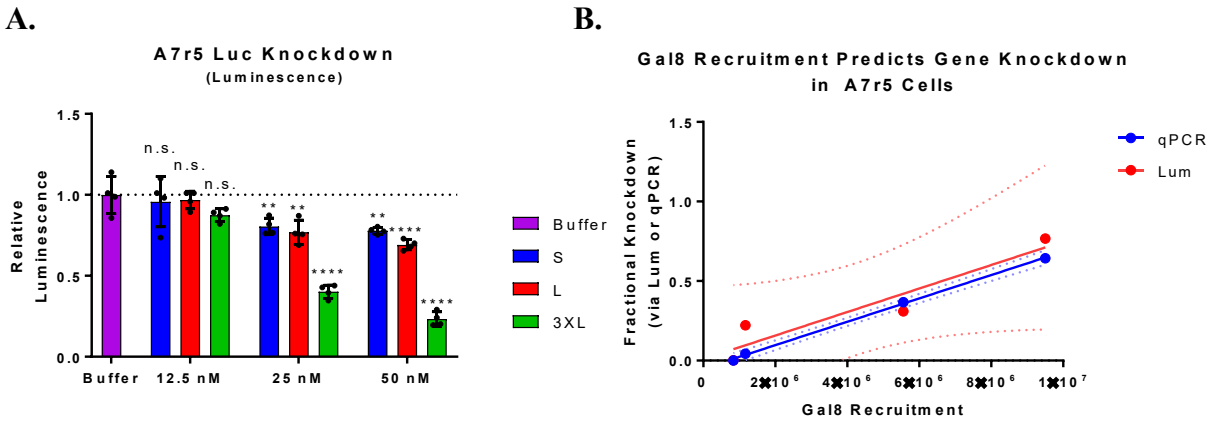

(A): A7r5 cells were treated with indicated concentrations of scrambled and siLuc sequences of siRNA. After 24 h of treatment, media was exchanged and luminescence was measured. The symbols *, **, ***, and **** represent $p < 0.05$, 0.01, 0.001, and 0.0001 respectively.

(B): Gal8 recruitment (From Figure 6F) was plotted on the x-axis against PHD2 levels (from Figure 6E) and luminescence levels (from Figure S10A) on the y-axis, and subjected to linear regression (solid lines, ± 95% confidence interval are dotted lines) and correlation analysis by Pearson's method. The correlation of the Gal8 to qPCR correlation was $r = 0.9995$, $p = 0.0005$ and the correlation of the Gal8 to knockdown by luminescence was $r = 0.94$, $p = 0.06$. This is summarized in the table below.

Statistical Summary, Figure S10B

Gal8 correlation to:	**qPCR**	**Luminescence**
r	0.9995	0.94
R^2	0.999	0.8836
P (two-tailed)	0.0005	0.06

S11: Spatial heterogeneity within Tumor Gal8 recruitment

A.

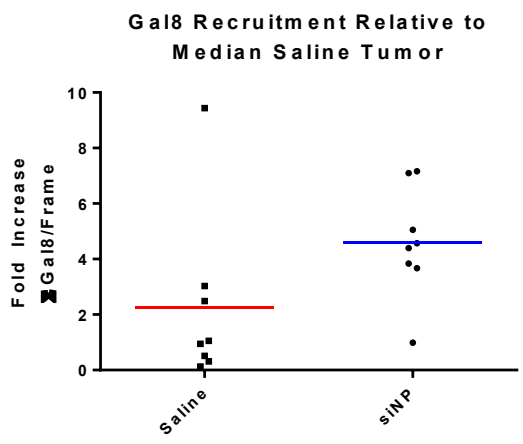

B.

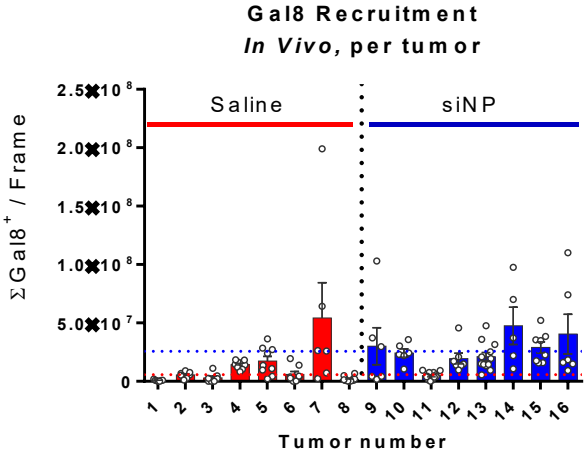

Tumors exhibited varying degrees of endosomal disruption.

A) An alternate plot of figure 7A, showing relative Gal8 recruitment relative to the median saline treated tumor's Gal8 recruitment measurement.

B) Some saline treated tumors (left) had Gal8 recruitment, and some locations within tumors of siNP treated mice (right) did not show Gal8 recruitment. Overall, siNP tumors were found to contain significantly more Gal8 recruitment. Lower, red ($0.57 * 10^7$) and upper, blue ($2.57 * 10^7$) dotted lines indicates the median tumor's average Gal8 recruitment *per* frame for saline and siNP treated mice, respectively. The median tumor's average Gal8 recruitment was 4.5 fold higher in siNP treated mice.

S11: Stably integrated genetic constructs do not substantially impact MDA-MB-231 siNP uptake.

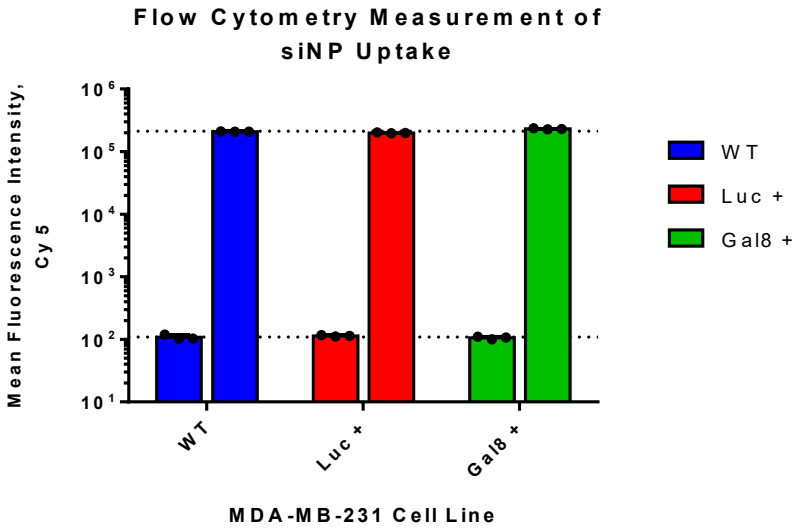

To assess whether stably integrated genetic constructs altered cellular uptake of 50B particle uptake, MDA-MB-231 cells (wild type, Luc+, and Gal8+) were treated with 50 nM Cy5 labeled siRNA loaded into 50B-L polyplexes for 24 hr then subjected to flow cytometric analysis of cellular fluorescence *per* methods in the main text.

Bar height represents mean fluorescence intensity of Cy5 channel; error bar represents standard deviation. Most error bars are too small to visualize on plot. Dashed lines represent the mean Cy5 fluorescence for siNP treatment (upper) and mean basal fluorescence (lower) of WT, Luc +, and Gal8 + cells.

Two-way analysis of variance (ANOVA) reveal that siNP treatment, genetic construct, and interaction thereof are statistically significant ($p < 10^{-4}$) contributors to dataset variance. siNP treatment contributes the overwhelming majority (99.2%) of dataset variation, while genetic construct and interaction with siNP treatment contributes 0.39% of variation each.

As over 99% of the total variance is explained by siNP treatment, we are satisfied that genetic constructs do not meaningfully alter siNP uptake relative to wild type MDA-MB-231 cells.

Supplemental Table 1: Correlation and statistics, Δ Hemolysis *versus* Knockdown

	KD, 12.5 nM		KD, 25 nM		KD, 50 nM	
	r	*p*	*r*	*p*	*r*	*p*
Hemolysis, pH 7.4	0.96	0.003	0.96	0.003	0.93	0.01
Hemolysis, pH 6.8	0.54	0.23	0.54	0.24	0.43	0.35
Hemolysis, pH 6.2	-0.36	0.44	-0.36	0.44	-0.46	0.30
Δ Hemolysis, pH 7.4-6.8	0.04	0.96	0.04	0.96	0.00	>0.99

Technical Note 1: Lines of best fit for correlation data

As with many biological phenomena, the underlying system is nonlinear. Gal8 recruitment measures endosomal disruption, not gene knockdown, so measurements of Gal8 recruitment can continue to increase even as siRNA-induced gene knockdown is saturated/maximized, although Gal8 recruitment can also be saturated (when all endo-/lysosomes are being simultaneously ruptured). On the other hand, gene knockdown increases asymptotically towards 100%; after all, gene expression cannot be negative.

Thus, we chose a hyperbolic fit to account for the asymptote of 100% gene knockdown in MDA-MB-231 cells. However, to further understand these data, we performed additional analysis. A linear fit constrained to pass through the origin provides an r^2=0.2701 for the whole dataset, but excluding the seven highest formulation-dose combinations that induced nearly saturating knockdown (>80%), the r^2 of the linear fit increases to r^2=0.8019. We see that these high values contribute to the deviation from a linear model. Even in that case of excluding the highest 7 values of knockdown (which are also the highest 7 values of Gal8 recruitment), a hyperbolic fit is still more appropriate ($p<0.0001$); with the linear fit resulting in 3.2-fold higher error. For the full dataset (including the 7 highest points), a linear fit contains 15.7-fold more error than the hyperbolic fit. We therefore concluded the hyperbolic fit is the appropriate fit for this dataset, with both strong biological and statistical rationale.

However, for the A7r5 dataset (Figure 6G), the rationale for a linear fit was twofold. One, the dataset contains fewer datapoints, resulting from the subset of polymers and doses tested (because in this cell line, knockdown was measured using qPCR), necessitating a simpler fit to avoid overfitting. Further, insufficient information is available to assess whether saturating effects were occurring in this cell line at this dose. These observed differences may be due to

myriad biological differences (e.g., differences in uptake, intracellular trafficking, endosomal integrity) between human metastatic breast cancer cells (MDA-MB-231) and rat smooth muscle cells (A7r5). Thus, without substantial rationale to support a more complicated model, we chose a linear best fit. In both the case of Figure 6A and 6G, the lines of best fit are to guide the reader to see trends we believe are present in the data, but were calculated independently of correlation and statistics.

At nonsaturating doses in MDA-MB-231 cells, 12.5 and 25 nM doses, the linear trends for both Gal8 recruitment (Fig 3A & 3B) are quite clean and thus highly predictive. At the highest dose (50 nM), the 4 largest polymers become statistically indistinguishable at gene knockdown, and these all have very robust Gal8 recruitment. Of course, to use this assay for any polymer system, dosing must be first be aligned to the limits of the assay, as with any new assay.

Technical Note 2: Microscopy requirements

Gal8 recruitment induces bright puncta against a relatively dim background, which are then identified algorithmically. The pixel intensities within these puncta are then integrated (summed). In exploring the data generated by this technique, we found this quantification method to be the most robust and generalizable.

The explanation is two-fold. One, the method requires relatively low power objectives (herein, a 20x) because it is not necessary to resolve two nearby disrupted endosomes from each other, so long as the total disruption is still quantified. (Higher power objectives may be needed for single endosome tracking studies, small cells, or time course experiments tracking a small number of cells.) Two, because our method integrates identified spots of high intensity, it minimizes the contribution of "false positives," *e.g.*, areas that are identified algorithmically as Gal8 positive but do not contain disrupted endosomes or particularly bright pixels, as encountered in spots of true Gal8 recruitment. These false positives spots contribute only a small amount to the sum of Gal8 intensity within Gal8+ spots, but would contribute a proportionately larger error in methods tracking the area fraction of Gal8+ or % Gal8+ cells.

The use of the 20x objective and this robust algorithm also affords another advantage. Our use of the 20× objective was critical to obtaining large fields of view, but also provided a thick optical slice in which the majority of the cytoplasm was in focus throughout the entire frame. In our hands, the low power 20x objective was far easier to focus than higher power 40x or 60x objectives, and still provided adequate resolution to resolve endosomes algorithmically when combined with a 2048 x 2048 pixel acquisition image. These large fields of view contained more cells (~200) which further increased the robustness of the system when combined with high quality, high-flatness glass coverslip bottom plates.

When combined with a nuclear stain, this allowed “blinded” focusing of the microscope system on the center plane of the MDA-MB-231 cell. Between this thick optical slice, automated focusing, and the robust quantification algorithm, we were surprised by the ease with which our imaging system proceeded, although optimizing these imaging settings for fast acquisition were crucial.

Implementing this method in other imaging systems may require the use of an autofocus algorithm, for which the nuclear channel would be well suited. This method does require an adequate resolution camera, adequate stage flatness, software-controlled stage and acquisition, *etc*. Each imaging system manufacturer has their own preferred implementation of focus assisting, usually using some combination of hardware and software. However, in our hands, imaging based autofocus algorithms increased image acquisition time unacceptably and did not improve data quality.

Indeed, before executing this assay on a new optical system, a sensitivity analysis should be conducted to ensure consistent and reproducible imaging and ensuring that the Gal8 signal remains within the focal plane. Appropriate method controls should be routinely employed when developing the method in house, especially to control for wash buffers, temperature and humidity changes, and other environmental factors that may affect endosomal integrity as cells are being manipulated.

CHAPTER 4
NOVEL ENDOSOME DISRUPTION REPORTER ASSAYS USING SPLIT LUCIFERASES

As we presented the work of Chapter 3 at conferences and shared these plasmids, cells, and viruses with other labs, we recognized that the Gal8-YFP system had several shortcomings. In particular, several groups struggled to optimize imaging and microscopy conditions, and our own work showed that Gal8-YFP had significant *in vivo* limitations. We thus set out to develop a high throughput "turn on" style assay whose analysis would be less technically challenging. We considered several systems, but ultimately chose to develop the split luciferase systems described here. We show proof of concept data that these systems produce luminescent responses with known endosome disrupting polymers in a dose dependent manner, motivating the further development of this type of assay.

4.1 Abstract

Endosomal disruption is a critical step in intracellular delivery of biomacromolecular drugs. We previously reported a high throughput microscopy-based endpoint assay based on intracellular Gal8-YFP tracking for use in the discovery and development of endosome disrupting drug formulations. While *in vitro* Gal8-YFP tracking is a robust and quantitative measure of endosome disruption, it requires advanced microscopy and an imaging time of approximately 45 minutes per plate. Meanwhile, *in vivo* Gal8-YFP tracking requires animal sacrifice per timepoint and generates noisy measurements. To overcome these limitations, we design, construct, and validate two novel high throughput assays based on split firefly luciferase, which can be measured quickly and easily using an IVIS luminometer. The first system labels

Gal8 with an N-terminal firefly luciferase fragment while CALCOCO2 is labeled with C-terminal firefly luciferase fragment. Gal8 and CALCOCO2 are hypothesized to interact following endosomal disruption, which reported as luminescence. The second system is constructed only as the minimal binding domain of Gal8 (Gal8 N-terminal carbohydrate recognition domain, G8-NCRD) fused to both N-terminal and C-terminal luciferase fragments. In both systems following endosome disruption, an increase in cellular luminescence is observed. Additionally and in contrast to Gal8-YFP tracking, these assays report as 'hits' only formulations and doses which are nontoxic, due luciferase's requirement of ATP, which is released from nonviable cells. In comparison studies between the lead luminescent cell line (G8G8 clone 4) and Gal8-YFP cells, the G8G8 system reveals endosomal disruption at a lower dose than Gal8-YFP is able to detect, and shows cytotoxicity in formulations where Gal8-YFP reports high endosome disruption. These systems represent a first-in-class luminescent assay to detect endosome disruption in high throughput while excluding toxic formulations and may prove useful in developing the next generation of drug carriers to enable the delivery of intracellular biologic drugs.

4.2 Introduction

Overcoming the intracellular endosomal membrane remains a critical barrier in the drug development of large molecule drugs with intracellular mechanisms of action. While there are now several exciting clinical success stories with large molecule drugs which act inside the cell, including drugs enabled by lipid nanoparticles and AAVs, the broad-scale clinical utilization of these medicines with the potential for unprecedented potency and specificity has been hindered by challenging pharmacokinetics in the circulatory system, specific tissue-level barriers to

delivery, and barriers at the cellular and subcellular level. At the cellular level, these hydrophilic molecules are first restricted from cellular entry by the plasma membrane, and even if internalized by endocytosis, are restricted from the cytosol by the endosomal and lysosomal membranes. A common strategy to enable cell entry and endosomal escape is by using nanoscale drug formulations or small molecule conjugates, which can shield cargos from enzymatic degradation and enhance intracellular accumulation via endocytosis.

Throughout this dissertation, I have focused primarily on a critical cellular barrier: the endosomal membrane, the final membrane barrier to productive cytosolic delivery. Following cellular endocytosis of biologic drugs, the endolysosomal system progressively acidifies and subjects cargos to a milieu of nucleolytic and proteolytic enzymes, which degrade these polymeric drugs made of nucleic or amino acids. One attractive strategy to overcome the multifaceted challenges of intracellular drug delivery is to encapsulate drugs in a nanoscale drug delivery system, which can be rationally designed to these challenges.

The most advanced example of this approach is a medicine developed by Alnylam, Onpattro (patisiran lipid complex formulation), which uses pH-responsive cationic lipid, PEG, and carrier lipids to encapsulate siRNAs for delivery to hepatocytes to reduce systemic levels of transthyretin, the misfolding of which causes hereditary ATTR amyloidosis, resulting in cardiac dysfunction and peripheral neuropathies.[1] Onpattro's nanoscale size and formulation cause accumulation in the liver, while its pH responsive lipid causes endosomal disruption and delivery of siRNAs to hepatocyte cytosol.

The use of this ionizable lipid has proven important to advancing this platform for intracellular delivery of siRNA, as its MC3 lipid component has an optimal pKa to disrupt endosomal membranes and deliver siRNA to the cytosol.[2] However, studying the factors that

directly control endosomal disruption remains difficult, as discussed in chapter 3. We and others have recently reported on the uses of fluorescence microcopy tracking of intracellular galectins to assess endosomal integrity.[3–5] Galectins are a family of glycan binding proteins which serve to mediate cell-cell and cell-matrix interactions, modulate immune cell functions, and function in the restriction of intracellular pathogens.[6] Glycosylation on the inner leaflet of endosomes becomes accessible to cytosolic galectin-3, -8 and -9 following membrane disruption by pathogens[3] or drug carriers.[4,5,7] By quantitative tracking of fluorescence redistribution from cytosol to disrupted endosomes, the extent of endosomal disruption by pathogens, viruses, and drug carriers can be compared.

Galectin 8 (here Gal8, but also known as hLGALS8 or LGALS8) is a particularly interesting lectin, as it is specifically involved in the detection of endosomal disruption and is critical to the restriction of intracellular infection by pathogens. Gal8 is a tandem-repeat lectin, containing two carbohydrate recognition domains (CRD) at the N and C termini with dissimilar substrate specificities. The N-terminal CRD (G8NCRD) binds to host glycans[3], specifically to sialylated glycans containing α2-3-sialylated or 3′ sulfated β-galactosides,[8] which are found as the terminal motif of human protein and lipid glycosylation.

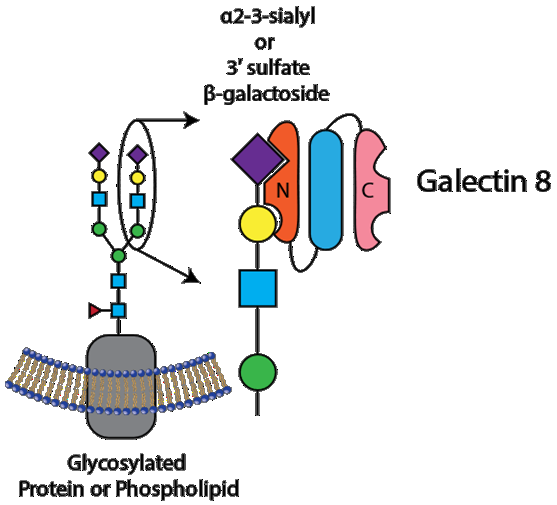

Figure 4.1. Binding and structure of Galectin 8. Gal8 binds to α2-3-sialylated or 3′ sulfated β-galactosides, which are found on transmembrane proteins and glycolipids inside endosomes. It consists of three domains, an N-terminal CRD (orange), a central linker region (blue), and a C-terminal CRD (pink).

Meanwhile, the C-terminal CRD (C-CRD) mediates trafficking of these damaged endosomes to an autophagic pathway by interacting with the C terminus of CALOCO2, which recruits LC3, an autophagy adapter protein, to induce macroautophagic engulfment of the damaged vesicle (Figure 4.1).[3,4,9] We have been particularly interested in the development of Gal8 based assays to monitor endosomal disruption in the context of subcellular trafficking of drug carriers.[4,5,7] We previously demonstrated a method of quantifying endosomal disruption that correlates to cytosolic siRNA delivery by quantifying the total recruited LGALS8 on a per cell basis, which was more highly predictive of cytosolic drug delivery than other measures when used to evaluate two related polymer libraries of the endosome disrupting polymer PEG-DMAEMA-co-BMA in vitro.[5] In *in vivo* screening, Gal8 tracking in MDA-MB-231 orthotopic tumors showed statistically significant endosomal disruption compared to vehicle control injections when analyzing freshly excised tumor slices. However, this method required high content microscopy capable of screening thousands of cells for robust analysis, and Gal8 recruitment *in vivo* was difficult to measure in thick, auto-fluorescent tissue. Further, because the skin is too thick to enable high resolution percutaneous microscopy, tumors were excised from sacked mice before imaging, precluding kinetic analyses typically performed to measure luciferase knockdown by siRNA in mice. In discussions with several colleagues at scientific meetings and by email, it became clear that a "turn on" style assay to measure endosomal disruption would be a welcome addition to the toolkit for nanoscale drug carrier development, especially if it were amenable to time course monitoring and/or use *in vivo*.

4.2.1 Design Considerations for a Next Generation Assay

We considered several possibilities for the construction of such a system, evaluating

several recent assay designs. We hypothesized that one paradigm for the assay construction was the interaction of Gal8 and another signaling partner, or structural protein in close proximity to Gal8 following endosomal disruption. To detect this, we considered split fluorescent protein systems, such as split GFP, which is widely used to assess protein-protein interactions. To measure the interaction between a protein pair A and B, one protein (A) is fused to the first 10 beta strands of GFP, creating A-GFP_{1-10}, while the putative second partner (B) is fused to GFP_{11}.Upon the interaction of A-GFP_{1-10} and B-GFP_{11}, the GFP_{1-10} and GFP_{11} domains undergo high affinity binding to mature into a stable fluorescent protein.[10] However, we chose not to pursue split GPF because fully assembled GFP is quite stable, and we presumed that two cytosolic interaction partners would likely produce quite high baseline complementation, especially because we planned to express both proteins from the same mRNA transcript, meaning both protein concentrations would be high at the site and time of translation from an mRNA. Further, GFP demonstrates pH-sensitive fluorescence, with a pK_a around 6.0,[11,12] suggesting that acidified vesicles below that pH would demonstrate reduced fluorescence. Finally, we had previously attempted to develop a split GFP system for a related peptide delivery project, and found that the system had a limited signal to noise ratio in our hands and required measurement by flow cytometry. While other fluorescent proteins are known to have less acid sensitivity, e.g., mCherry,[12] the use of non-GFP FPs in split FP systems is less well validated. A FRET-based reporter was considered, but helpful conversations with Dr. Joachim Goedhart, an expert in fluorescent proteins and FRET-based measurements, suggested such a reporter would not be substantially easier to use than our existing Gal8 methodology, and would require additional controls for each single-color pair, as well as cells expressing both fluorescent proteins without FRET. Initial experiments attempting to identify FRET activity between Gal8-YFP and

LC3B-mTurquoise2 (which form a large complex consisting of Gal8, CALCOCO2, and LC3B) using spectral confocal microscopy did not yield useful data, due to lack of these controls. These experiments showed that the execution of this assay would require three different cell lines—one containing both constructs, as well as single construct controls, as well as appropriate positive and negative control experimental groups for these donor-only and accepter-only control cell lines. This would be a prohibitive assay setup for high throughput and *in vivo* screening. Finally, we considered a split luciferase system based on the work of Paulmurugan and Gambhir, who demonstrated that the 550 amino acid firefly luciferase, when split into two fragments with four overlapping amino acids (A.A. 1-398 and 394-550), produced a low affinity pair suitable for assessing transient protein-protein interactions, with high overall luminescence and a response of ~800-fold for some interactions measured in cell lysates.[13] This system was attractive for several reasons: firefly luciferase is widely used *in vitro* and *in vivo*, utilizes the inexpensive and nontoxic substrate beetle D-luciferin, and is already established within our group to monitor siRNA mediated knockdown *in vitro* and *in vivo*. Finally, firefly luciferin (unlike *renilla* or related coelenterazine-dependent luciferases) requires ATP, which is at low concentrations outside the cell and in intact endosomes.

We therefore hypothesized that measuring the protein-protein interaction of Gal8 and a downstream signaling protein following endosomal disruption using a split luciferase system would be more amenable to high throughput screening and could potentially be used *in vivo* for repeated measurements in the same animal. Further, because the luminescent reaction requires ATP, found only in live cells with intact cellular membranes, any luminescent signal would measure endosomal disruption in live cells and would not produce high signal for cytotoxic doses of polymer, as we have seen for the Gal8-YFP system.

We designed two engineered split luciferase reconstitution systems *in silico* which we hypothesized would be useful for the high throughput study of endosomal disruption. The first system, dubbed the G8C2 system, was constructed to assess the protein-protein interactions of Gal8 and CALCOCO2 (also known as NDP52), which have been shown to interact downstream of Gal8 clustering to initiate LC3-medated mediated macroautophagy.[3] Full length copies of Gal8 and CALCOCO2 were connected N-terminal to human codon optimized luciferase-2 amino acids 1-398 (NLuc398) and C-terminal to luciferase amino acids 394-550 (CLuc394), respectively, by a long and highly flexible 3x(GGGGS) linker, with an internal ribosomal entry site to drive expression of both partners from the same mRNA transcript (Figure 4.2). Our design was informed by the recently elucidated structure of that interaction, such that NLuc398 and CLuc394 would be in close proximity upon hetero-tetramerization of the Gal8/Gal8/CALCOCO2/CALCOCO2 complex.[9] We hypothesized that such a system would demonstrate enhanced luminescence upon endosomal disruption due to the

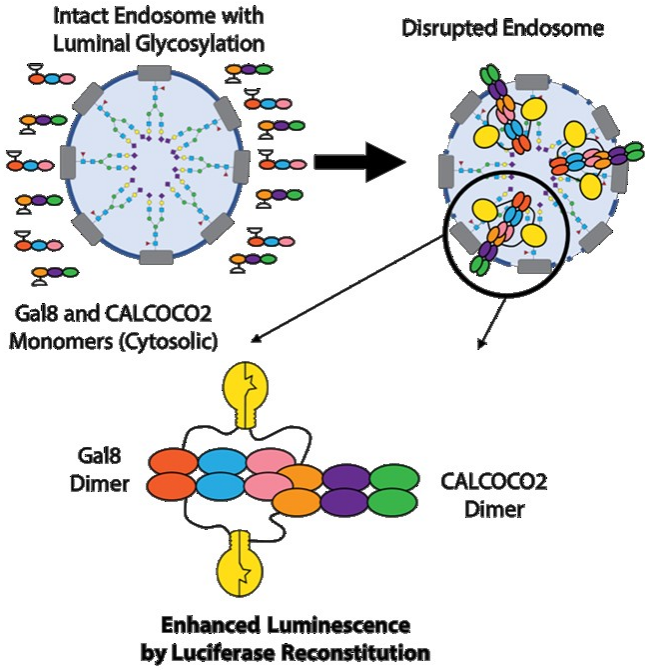

Figure 4.3. Hypothesized mechanism for the G8C2 System. Prior to endosomal disruption, NLuc-G8 and C2-CLuc exist as monomers in the cell cytosol outside endosomes. Following loss of endosomal membrane integrity, G8 binds to luminal glycans, triggering the formation of a G8/G8/C2/C2 heterodimer complex, which results in enhanced luminescence.

documented interaction between LGALS8 and CALCOCO2. The schematic for the hypothesized interaction is shown at Figure 4.3 and the plasmid will be deposited with AddGene under the name pLenti NLuc398-hGALS8 IRES hCALCOCO2-CLuc394.

The second system, dubbed G8G8, is based on a rational analysis of Gal8 domain-glycan interactions, and comprises two fragments of firefly luciferase attached to the Gal8 N-CRD *via* a flexible linker. NLuc398 was connected as an N terminal fusion to G8NCRD, while CLuc394 was connected as a C terminal fusion. Upon intra-endosomal concentration, Luc-N and Luc-C fragments could reconstitute and produce luciferase signal on the endosomal glycocalyx. A schematic of this is shown as Figure 4.4, and the plasmid encoding this system has been deposited with AddGene under the name pLenti NLuc398-G8NCRD IRES G8NCRD-CLuc394. Finally, both systems were inserted into a lentiviral vector containing blasticidin resistance to allow the relatively rapid generation of new cell lines using frozen lentiviral concentrates. Several aliquots have been generated, validated, and stored at -80 °C and are available upon request.

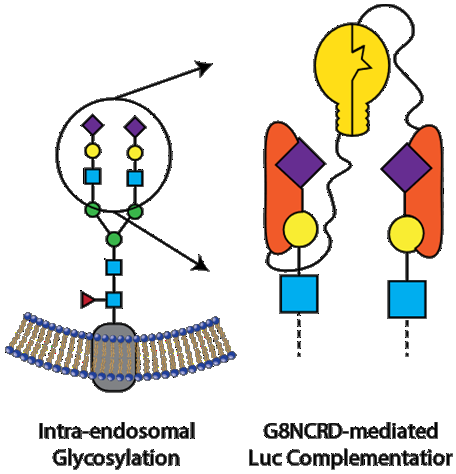

Figure 4.4. Hypothesized mechanism of G8G8 system.
Following endosomal disruption, G8 clusters at luminal glycans, which bring both fragments of NLuc and CLuc into sufficiently close proximity to trigger luminescence

4.3 Results and Discussion

4.3.1 Generation of Transgenic Cell Lines

Although the ratio of the two components was fixed by using an IRES element, we hypothesized that differential expression of the overall components may affect overall luminescence and the luminescent response of these constructs. Therefore, we generated cell lines using a variety of transduction ratios in parallel by first concentrating lentivirus using centrifugal spin filtration approximately 40-fold, then using this concentrate to generate a serial dilution of the virus in medium before cells were transduced in a 96-well plate. These cells were expanded in antibiotic-containing medium to purify the cell population. An example of this growth curve, measured by the Alamar Blue assay, is shown in Figure 4.5. This shows that several log concentrations of virus produce stable cell line integrants.

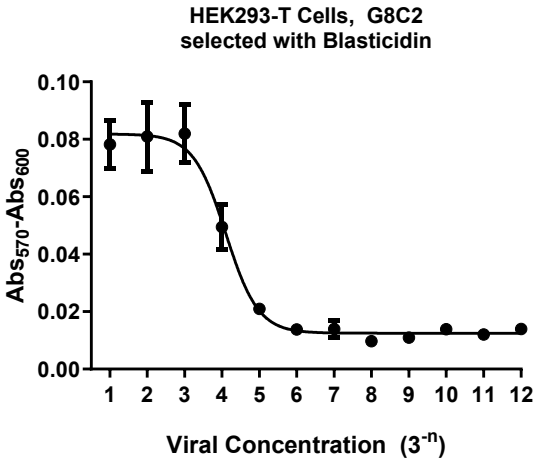

Figure 4.5. Example viability curve for G8C2 system dilution series
Cells were treated with a 3-fold dilution series of concentrated virus and cultured for approximately one week. Relative cell number was measured using the Alamar Blue assay. These data provide strong rationale for investigating the first 5 clonal populations.

4.3.2 The G8C2 System Shows Activity as an Endosome Disruption Assay

We assessed endosome disruption using the endo-lysosome disrupting polymer poly(propyl acrylic acid), which has been well studied for use as a peptide delivery reagent,[14,15] and which we have previously shown induces endosomal disruption which is detectable using the microscopy

based Gal8-YFP assay.[7,16] We tested five different clones of HEK293-T cells generated from different dilutions of G8C2 virus to assess which transfection ratios produced highly responsive cells. These results are presented in Figure 4.6. Two clones, number 1 and 3, produced statistically significant increases of cellular luminescence following PPAA treatment, while clones 2, 4, and 5 did not produce significant increases in cellular luminescence. Specifically, clone 1 of the G8C2 system is a highly responsive system with a favorable response profile that aligns with our understanding of PPAA treatment. PPAA induces cytotoxicity at high doses, which is observable as luminescence below baseline (-7512 RLU below vehicle control, n.s. for the highest dose tested, 1.25 mg/mL PPAA). At decreasing doses of PPAA, intra-endosomal interaction of NLuc and CLuc produce statistically significant increases in luminescence (4.7 fold at 312.5 μg/mL, $p = 0.002$; 4.8-fold at 156.25 μg/mL, $p < 10^{-4}$; 7.122-fold at 78.13 μg/mL, $p < 10^{-4}$; and 4.0 fold at 39.06 μg/mL, $p = 0.0002$). These results are, to our knowledge, the first system which reports a luminescence-based assay to measure intracellular endosomal disruption in live cells. For clone 1 of the G8C2 system, we report that two way ANOVA reveals that polymer treatment, dose, and interaction thereof all contribute as statistically significant factors in the dataset variance, with polymer/vehicle treatment accounting for 11% of variance ($p < 10^{-4}$), polymer concentration contributing 38% ($p < 10^{-4}$), and interaction thereof 38% of variance ($p < 10^{-4}$). The area under the response curve (Fig 4.6 B, D, F, H, J) with a baseline of Y=1 was 1766 (fold change) × (μg/mL) for Clone 1, which 26-fold higher than for the lowest AUC of Clone 5. Clone 3, the only other clone which produced statistically significant responses in dose matched post hoc testing, had an AUC of 266, or only 15% of the overall responsivity of Clone 1. The two-way ANOVA for Clone 3 further revealed that PPAA contributed 15% of variance ($p < 10^{-4}$), dose contributed 26% of variance ($p = 10^{-4}$), and interaction thereof contributed 18% (p

= 0.004). Clones 2, 4, and 5 did not have significant differences in post hoc testing, although dose had a statistically significant effect in clone 2 (29%, $p = 0.03$) and clone 5 (41%, $p = 0.001$).

These data confirm earlier reports of Gal8/CALCOCO2 interaction following endosomal disruption in general[3] and, to our knowledge, are the first direct confirmation of this protein-protein interaction in live cells following endosomal disruption. While the G8C2 system is quite promising at detecting endosomal disruption in population 1, the majority of cell populations were not useful. Further refinement of the cell population may prove advantageous, potentially by single cell isolation and expansion. Future work could focus on isolating particularly optimal cells or could remove endogenous Gal8 and CALCOCO2, e.g., by TALEN or CRISPR mediated gene disruption, because the untagged Gal8 and CALCOCO2 function as inhibitors of the luminescent protein complex.

Table 4.1: Summary of Statistical Tests for G8C2 system

	Source of Variation	% of Total Variation	P Value	P Value Summary
Clone 1, G8C2	Interaction	37.8	<0.0001	****
	Dose	38.01	<0.0001	****
	PPAA vs. Vehicle	10.86	<0.0001	****
Clone 2, G8C2	Interaction	13.48	0.4356	ns
	Dose	29.34	0.027	*
	PPAA vs. Vehicle	0.09896	0.7742	ns
Clone 3, G8C2	Interaction	17.83	0.0042	**
	Dose	25.55	0.0001	***
	PPAA vs. Vehicle	15.05	<0.0001	****
Clone 4, G8C2	Interaction	12.86	0.6018	ns
	Dose	20.18	0.2438	ns
	PPAA vs. Vehicle	0.161	0.7352	ns
Clone 5, G8C2	Interaction	6.915	0.8096	ns
	Dose	40.54	0.001	***
	PPAA vs. Vehicle	3.221	0.083	ns

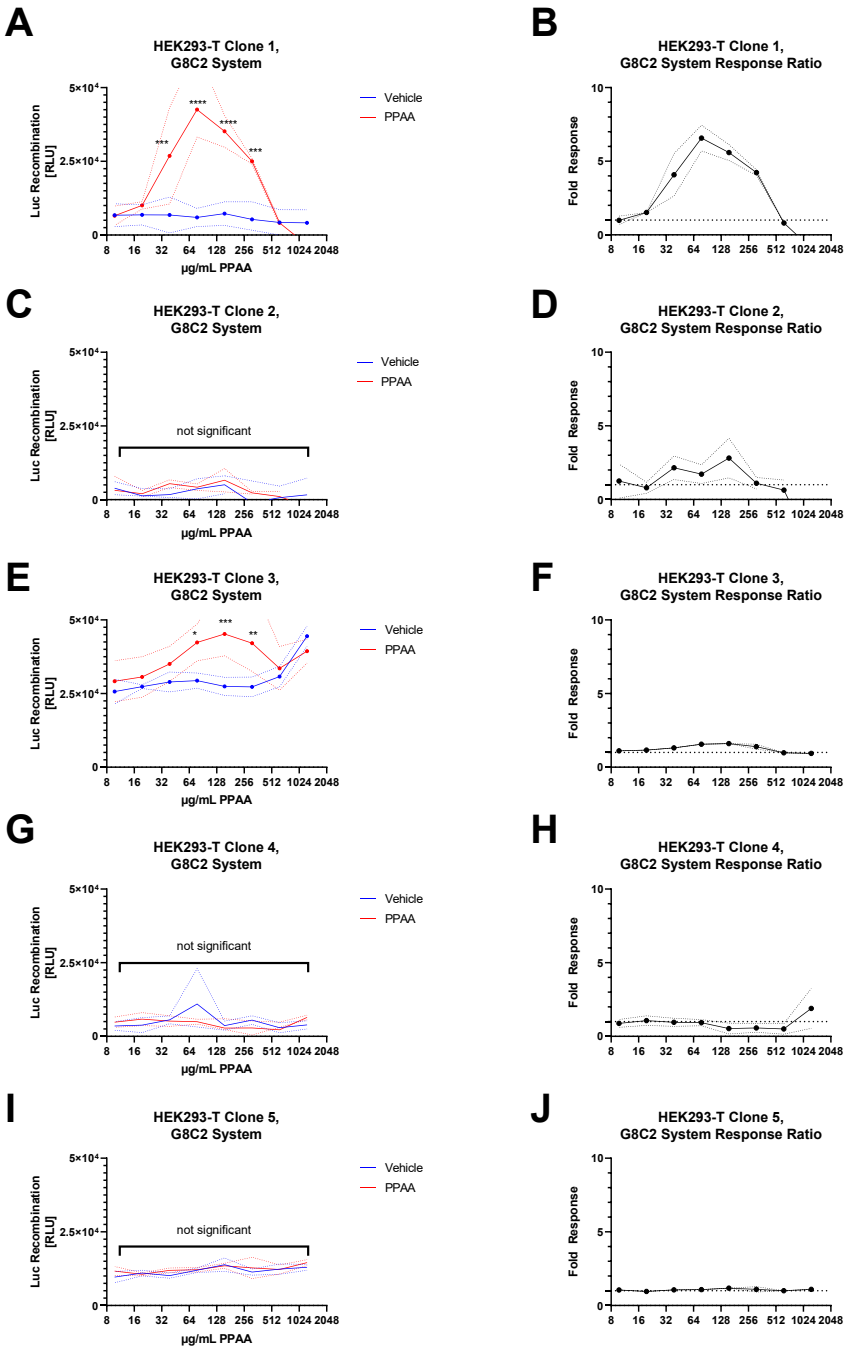

Figure 4.6. Some clones of G8C2 system show increased luminescence under endosomal disruption

A, C, E, G, I: G8C2 cells were treated with a 2-fold serial dilution of PPAA for 2 h, media exchanged, and luminescence measured. p values are indicated as: $p < 0.05$, *; < 0.01 **; < 0.001 ***; < 0.0001 ****

B, D, F, H, J: luminescent response was normalized to vehicle values and plotted as fold response versus PPAA concentration

4.3.3 Characterization of the G8G8 System

We then also characterized an alternate approach to ask whether merely clustering NLuc and CLuc at the intra-endosomal surface would function as a robust endosome disruption reporter. To achieve this, we used the Gal8 N-terminal carbohydrate recognition domain as a targeting moiety to direct both NLuc and CLuc to damaged endosomes. Because we suspected that overexpression of full length Gal8 and CALCOCO2 could alter the cellular response to endosomal disruption or otherwise alter cell behavior or endocytosis, we hypothesized that using the N-terminal carbohydrate recognition domain could be used as a sort of "minimal" endosomal escape detection system, with a 23.6% shorter DNA sequence (3,318 base pairs for G8G8 vs. 4,344 base pairs for the G8C2 system), which would allow additional elements to be introduced into the same vector. Because lentiviral systems are limited to approximately 6,400 base pairs of cargo DNA (consisting of promoters, genes of interest, and selection elements), the additional capacity may be useful in a downstream application. As proof of this concept, we additionally incorporated an EGFP element to assess transduction efficiency by microscopy into the G8G8 system. Further, literature sugested[9] that the effector functions of Gal8 signaling as an endosomal damage sensor occur through its C-terminal carbohydrate recognition domain, and that by removing these effector functions from the moiety used to target NLuc and CLuc to damaged endosomes, overexpression of G8NCRD in the G8G8 system may perturb underlying cell biology less than high levels of overexpressed, full-length Gal8 and CALCOCO2.

Clonal populations of HEK239T cells expressing the G8G8 system were generated using a dilution series of concentrated G8G8 lentivirus and were characterized as for the G8C2 system. We tested the first five populations of cells expressing the G8G8 system to characterize the overall response of this alternate design. In contrast to the G8C2 system, all five populations

tested produced statistically significant increases in luminescence in response to PPAA treatment. However, the maximal fold-increase in signal intensity was slightly below 3, whereas the maximal response in the G8C2 system, in G8C2 clone 1, was over 7-fold. All five clones of the G8G8 system produced statistically significant results in post hoc testing (Figure 4.7); the results from two-way ANOVA are presented in Table 4.2 below.

Interestingly, the G8G8 system overall produced an order of magnitude brighter overall luminescence, which likely contributed to the lower variance of measured signal, improving statistical confidence of measurements using this assay. It is not apparent what causes this higher baseline and response luminescence, though this higher signal and lower variance may prove useful in downstream screening assays and especially in the context of an *in vivo* reporter.

Table 4.2: Summary of Statistical Tests for G8G8 system

	Source of Variation	**% of Total Variation**	**P Value**	**P Value Summary**
Clone 1, G8G8	Interaction	38.69	< 0.0001	****
	Dose	45.61	< 0.0001	****
	PPAA vs. Vehicle	0.8182	0.0504	ns
Clone 2, G8G8	Interaction	46.91	< 0.0001	****
	Dose	39.76	< 0.0001	****
	PPAA vs. Vehicle	3.656	< 0.0001	****
Clone 3, G8G8	Interaction	39.38	< 0.0001	****
	Dose	42.96	< 0.0001	****
	PPAA vs. Vehicle	14.22	< 0.0001	****
Clone 4, G8G8	Interaction	37.43	< 0.0001	****
	Dose	39.04	< 0.0001	****
	PPAA vs. Vehicle	17.46	< 0.0001	****
Clone 5, G8G8	Interaction	41.36	< 0.0001	****
	Dose	40.34	< 0.0001	****
	PPAA vs. Vehicle	0.3359	0.2497	ns

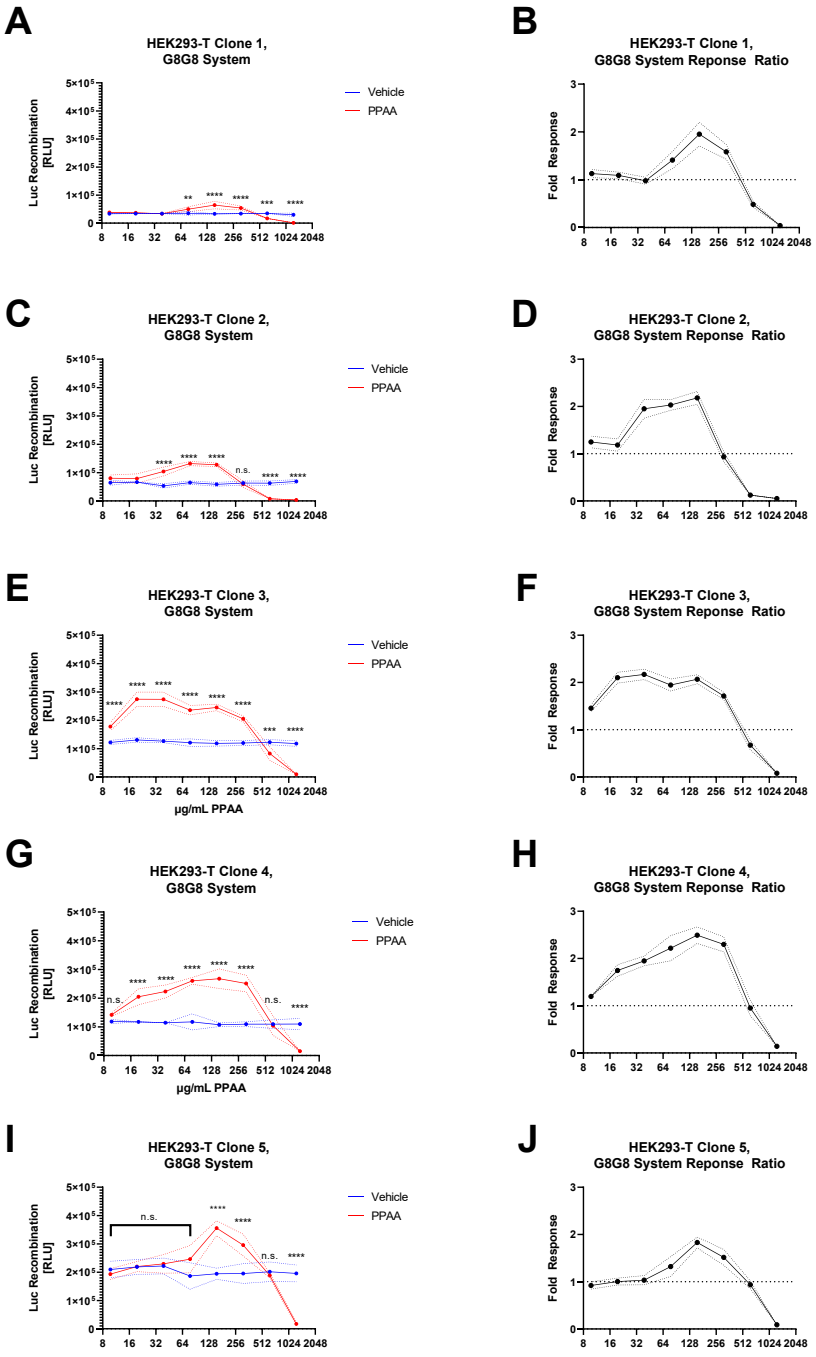

Figure 4.7: G8G8 system allows measurement of endosomal disruption in live cells across a variety of transduction ratios

A, C, E, G, I: G8G8 cells were treated with a 2-fold serial dilution of PPAA for 2 h, media exchanged, and luminescence measured. p values are indicated as: $p < 0.05$, *; < 0.01 **; < 0.001 ***; < 0.0001 ****

B, D, F, H, J: luminescent response was normalized to vehicle values and plotted as fold response versus PPAA concentration

4.3.4 Comparisons of G8C2 and G8G8 Systems

When looking at a plot the AUC versus viral concentration (Figure 4.8), we see that AUC correlates to viral concentration, with a statistically significant positive nonzero slope ($p < 0.05$, $R^2 = 0.90$) and thus conclude that very high transduction ratios are advantageous for the G8C2 system, for which NLuc-Gal8 and CALCOCO2-CLuc compete only with their endogenous protein to form a luminescent heterocomplex of Gal8 and CALCOCO2.

In order to qualify which system and clones were most appropriate for use as a screening assay, we further compared the G8C2 system to the G8G8 system. First, we calculated the area under the curve (AUC) of the fold-response curves (Figures 4.6 and 4.7: B, D, F, H, J) as the peak area above baseline ($y = 1$) to compare the overall responsivity for these systems, and plotted it against the relative concentration of viral concentrate used to initially transduce that cell clone. Linear best fits were calculated using Prism. For the G8C2 system, a line of best fit with statistically significant positive slope ($p = 0.0131$) and $R^2 = 0.90$ was found, suggesting that increased viral multiplicity of infection (MOI) improves the responsivity of the G8C2 system (Figure 4.8). For the G8G8 system, the calculated line of best fit had a slope whose 95% confidence interval did not exclude 0 ($p = 0.2741$, $R^2 = 0.29$), meaning that no statistically significant positive or negative correlation is present between multiplicity of infection and G8G8 system responsivity (Figure 4.8). When plotting AUC of the G8C2 and G8G8 response curves, we see that while G8C2 Clone 1 produced the highest overall response, but only two of these systems produced a useful response. All clones with an AUC above 225 ($n = 7$) had statistically significant luminescent responses, while all systems with an AUC below that threshold ($n = 3$) failed to detect endosomal disruption at any dose in post hoc testing. Further, all G8G8 clones tested had overall consistent response curves, suggesting that this system may be less sensitive to

MOI than the G8C2 system. We hypothesize that this may be due to the fact that, for the G8C2 system, NLuc-Gal8 and CALCOCO2-CLuc compete only against endogenous protein to produce a luminescent complex, whereas in the G8G8 system, both Gal8-CLuc and Gal8-NLuc, as well as endogenous Gal8, are competing among one another for binding to intra-endosomal galactosides to produce luminescence complementation. Essentially, the G8G8 system has a larger reaction surface area to catalyze Luc reconstitution, because it uses the entire luminal surface of the endosome, whereas in the G8C2 system, CALCOCO2 binds to clustered Gal8, one step downstream of the initial binding event. It therefore stands to reason that the G8G8 system has a higher overall binding surface to drive luciferase complementation. However, very high levels of endosomal disruption could provide more binding sites for Gal8NCRD than the cytosolic pool of Gal8NCRD can detect, limiting overall sensitivity. In such a case, a high MOI may be warranted.

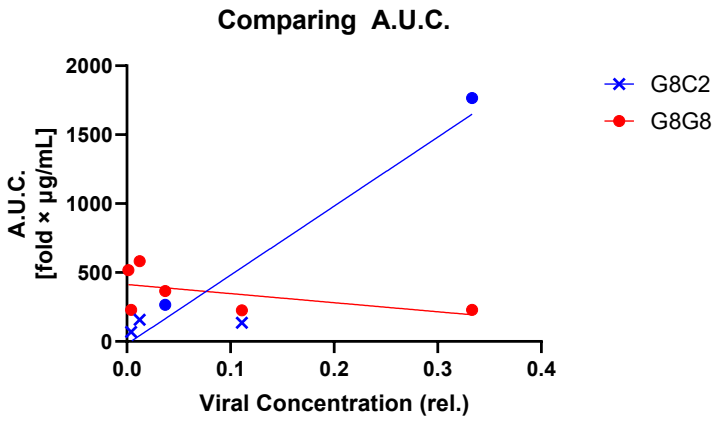

Figure 4.8. AUC versus viral concentration reveals the G8C2 but not the G8G8 system benefits from higher transfection ratios

The area under the curve for each PPAA endosome disruption experiment was calculated and plotted against the viral dilution factor to check whether MOI had any effect on system responsivity. The G8C2, but not G8G8 system did have a statistically significant correlation between MOI and AUC. Datapoints correspond to clones 1-5 for each system, counting from the right, *i.e.*, the rightmost points are clone 1 and the leftmost points are clone 5. Datapoints are plotted as closed circles if at least one dose of PPAA produced a

4.3.5 Comparisons to Validated Endosomal Escape Assay

Finally, to assess the overall ability of these new assays to detect endosomal disruption, a third cell line was generated based on previous work[5] (Aim 2), based on confocal fluorescence microscopy imaging of Gal8-YFP. While pilot experiments were performed with previously generated MDA-MB-231 Gal8-YFP cells, differences in cellular uptake and intracellular trafficking dictated that a comparison to the Gal8-YFP system of Aim 2 needed to be compared within the same cell type, so Gal8-YFP retroviruses were applied to HEK293-T to generate Gal8-YFP HEK293T cells. These cells were treated with dose and time matched PPAA and analyzed as in Aim 2.

Gal8-YFP tracking shows the same overall trend for PPAA in HEK293-T cells, with a strong dose response to PPAA treatment. However, the overall response ratio for the microscopy-based assay is much higher than either luminescence-based system. The AUC for the Gal8-YFP system (Figure 4.9 B) is 12572, versus 1766 for G8C2 clone 1 or 583 for G8G8 clone 4, indicating the Gal8-YFP system has a much larger magnitude of overall response to

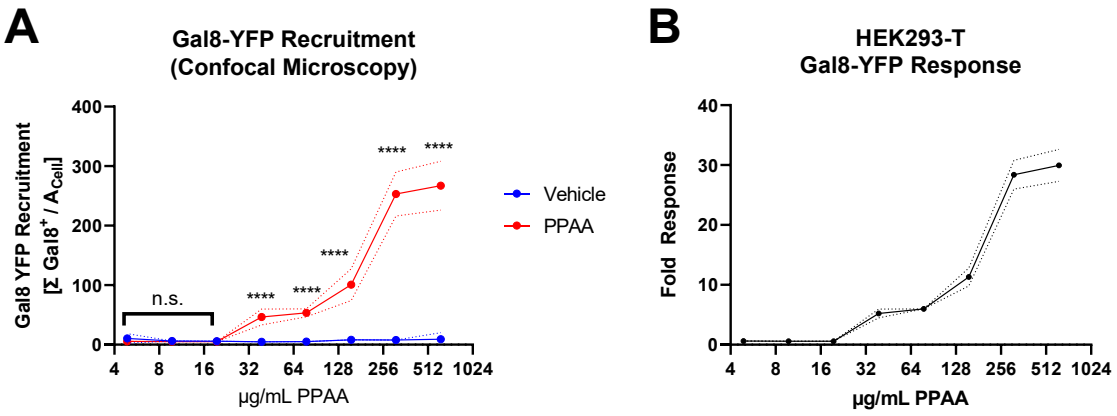

Figure 4.9. Gal8-YFP tracking shows Gal8-YFP recruitment occurring above ~20 µg/mL PPAA
Gal8-YFP expressing HEK 293-T cells were treated with a dose dilution series of PPAA for 2 h as for G8G8 and G8C2 studies. Cells were imaged and analyzed as in Chapter 3

endosomal disruption than either luminescent system. This is due to effective suppression of the background signal through image analysis algorithms developed in Aim 2, and suggests that luminescence-based assays should be improved an additional 7 to 22-fold in order to match the responsivity of Gal8-YFP based assays.

Finally, directly comparing the Gal8-YFP system against the most sensitive G8G8 assay, clone 4, we observe an interesting ability of the G8G8 system to detect two interesting things (Figure 4.10). One, G8G8 excludes the toxic PPAA dose of 625 µg/mL of PPAA. At this dose of PPAA, the polymer causes membrane leakiness, causing cytotoxicity and loss of cytosolic ATP. However, prior to loss of cell viability by membrane destruction, the polymer also disrupts endosomes and causes Gal8 punctation, causing a very high Gal8-YFP response. Thus, in some regards, Gal8-YFP returns false positive measurements for toxic doses of membrane interactive

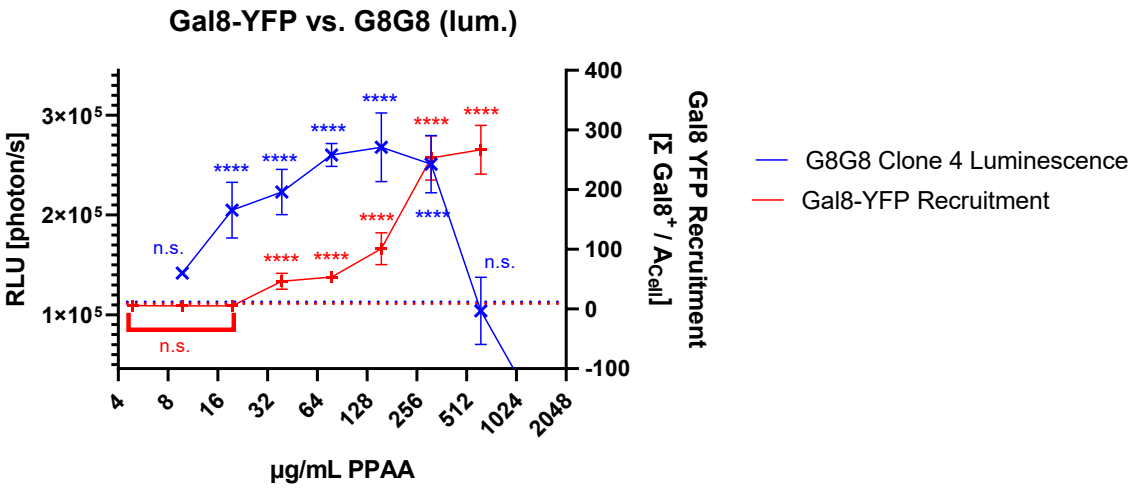

Figure 4.10. Gal8-YFP and G8G8 response are broadly correlated, with exceptions at toxic doses
The luminescent response of G8G8 clone 4 was plotted on the left axis (blue line, x) and Gal8-YFP response was plotted on the right axis (red line, +). Asterisks indicate statistical significance of same experiment relative to vehicle control. Left and right axes were adjusted such that vehicle (dotted lines) and highest responses approximately aligned between the two assays.

polymer, whereas the G8C2 and G8G8 luminescent systems require live and metabolically active cells due to the ATP-dependence of firefly luciferase. Further, G8G8 detects statistically significant endosomal disruption at 20 μg/mL PPAA ($p < 10^{-4}$), whereas Gal8-YFP recruitment tracking fails to observe these differences.

These results indicate that, while Gal8-YFP tracking produces superior signal to noise measurements, our novel systems based on split luciferase reconstitution are still useful, as they produce statistically significant results which nicely agree with previously validated endosome disruption measurement systems. Not only does the G8G8 system detect statistically significant differences for an additional low dose of PPAA, but it does not produce luminescence for high polymer doses that induce membrane permeability. This suggests that split firefly luciferase systems may prove superior to Gal8-YFP tracking despite the lower response ratio, due to less potential for false positives which can be observed for Gal8-YFP cells treated with toxic doses of drug carriers. However, a significant limitation of the luminescent systems are the small ratio of the luminescent response to the baseline signal, which may require a large number of measurement wells to have high statistical certainty in these responses.

4.4 Conclusions

The development of intracellular acting large molecule biologic drugs remains limited by cellular barriers to intracellular delivery, especially the plasma and endosomal membranes. The eventual development of intracellular, large molecule drugs may require drug carriers to shuttle molecules across these key barriers. While several assays have been developed to specifically assess intracellular drug delivery, we show here a first-in-class assay which uses luminescence to allow rapid and sensitive measurement of endosomal disruption in live cells. Further, like our

previous Gal8-YFP assay, it is carrier- and drug-agnostic and does not require labeling of either drug or carrier with tracers, dyes, or synthetic fluorophores which could alter cellular uptake or trafficking. Our work here is not without limitations, however. The luminescent signal from the G8G8 system is approximately 10-fold lower than our constitutive MDA-MB-231 cells used *in vivo* in Aim 2, and the leading G8C2 system is approximately 100-fold dimmer. Empirical testing will be required to assess whether these cells produce sufficient luminescence for application for intravital screening, although this is complicated by several factors, including the fact that several orders of magnitude more cells are used *in vivo* than a single well. However, the high numbers of cells present in tumors which make Gal8-YFP analysis difficult only help in producing a stronger luminescent signal. In all, the systems presented here are the first ever luminescence-based assays to study endosomal disruption, and reduce the time to measure an entire plate of cells from hours to 60 seconds. These new systems show that measurement of endosomal disruption using luminescence is possible and warrants closer study in the future.

4.5 Materials and Methods

4.5.1 Plasmid Design

Lentiviral transfer plasmids were designed *in silico* and generated by VectorBuilder (Chicago, IL, USA). The G8G8 system was designed as follows: the first ORF contained the following a Human eukaryotic translation elongation factor 1 alpha1 (EF1A) promoter driving an mRNA transcript containing the first 398 amino acids of *Photinus pyralis* luciferase (Ppy-Luc) connected in frame with “GGGGS” triplet spacer (3xG4S) to the first 157 amino acids of human Galectin 8, corresponding to the N-terminal carbohydrate recognition domain (G8NCRD) with a stop codon, followed by an internal ribosome entry site derived from the encephalomyocarditis

virus upstream of the complementary split luciferase partner, which was the terminal 156 amino acids of Ppy-Luc, a 3xG4S spacer, followed by the same G8NCRD. The second ORF consisted of a cytomegalovirus (CMV) promoter driving enhanced green protein connected to blasticidin-S deaminase *via* a T2A self-cleaving peptide. The degree of luciferase fragment overlap (4 AA) and split point (1:398; 394:550) were chosen based on work by Paulmurugan and Gambhir,[13] which showed this design to produce strong luminescence upon protein-protein interaction. The G8C2 system was designed as follows: the first ORF contained the following a Human eukaryotic translation elongation factor 1 alpha1 short form (EFS) promoter driving an mRNA transcript containing NLuc394, 3xG4S, and full length LGALS8 [NM_201545.2], followed by full length human CALCOCO2 [NM_001261390.1], 3xG4S, Luc394, then a stop codon. The second ORF consisted of a cytomegalovirus (CMV) promoter driving blasticidin-S deaminase.

4.5.2 Lentiviral Preparation

Psuedotyped lentiviral particles (PLV) were generated using transfer plasmids, pCMV delta R8.2 (AddGene Cat. No. 12263) and pMD2.G (AddGene Cat. No. 12259). Such that a final volume of 600 µL was reached, the following components were added, in order, to a 15 mL polypropylene conical tube to yield a transfection mixture: Opti-MEM media (Gibco, Cat. No. 31985062), 0.6 µg pMD2.G, 3.0 µg pCMV delta R8.2, 6.0 µg transfer plasmids, and 42 µL FuGENE 6 (Promega, Cat. No. E2691). The tube was gently flicked to mix the plasmids before and after the addition of FuGENE 6. The transfection mixture was added dropwise to a T-75 flask at approximately 50% confluency of HEK-293-T cells in 11.0 mL DMEM/F-12 supplemented to 10% FBS without antibiotics. After 18 h incubation, the media on the HEK-293-T cells was exchanged for DMEM supplemented with 10% FBS and 1% penicillin-

streptomycin. At 24 h, 48 h, and 72 h after this media change, the virus-containing supernatant was harvested, syringe filtered (0.45 μm, nylon), and concentrated from ~11 mL to ~250 μL with Amicon Ultra-15 centrifugal filtration unit (100 kDa nominal molecular weight cut off). The PLV were then either used immediately or aliquoted and frozen for later use.

4.5.3 Cell Line Generation

Cell lines stably expressing these reporters were generated as follows. A 2-fold dilution series was made in serum free, HEPES supplemented DMEM, starting with undiluted viral concentrate (2^0) and ending with 2^{-11} viral supernatant. To 12 wells of a 96-well plate, 100 μL of 10^5 cells / mL were added. Then, 100 μL from the dilution series was added to the plate of cells. After 48 h in which the cells adhered and proliferated, the media was changed and selection began, using DMEM supplemented with 10% FBS and 5 μg/mL blasticidin. Cells were monitored by phase contrast microscopy; as wells reached confluence, cells were washed twice with PBS -/-, trypsinized with a minimal volume of 0.25% trypsin, diluted with serum containing media, and transferred without centrifugation to progressively larger vessels. Media was changed every 48 – 72 h. As each T-75 flask reached ~80% confluence, half the cells were aliquoted and stored cryogenically in a 90:10 mixture of FBS and DMSO and further expanded using T-175 plates. Cells were periodically monitored throughout this process for EGFP expression *via* microscopy or for luciferase expression by IVIS imaging.

4.5.4 Luciferase Measurements

Luciferase measurements were in live cells by exchanging media with media supplemented with 10% FBS, 150 μg/mL D-luciferin, and 25 mM HEPES. Cells were imaged after 3-5

minutes of incubation at 37 °C in clear bottom, black wall, 96-well plates in an IVIS Lumina Imaging system (Xenogen Corporation, Alameda, CA, USA) with 60 s exposure. ROIs were drawn and average photon flux was calculated and exported. Dose response curves were plotted with GraphPad Prism.

4.5.5 Gal8-YFP Measurements

Gal8-YFP measurements were conducted as previously reported in Aim 2,[5] with two differences. First, HEK293-T were used instead of MDA-MB-231 to generate stable Gal8-YFP expressing cells. Second, recruited Gal8-YFP was normalized to total cellular area rather than cell number by quantifying cellular area by thresholding pixels above background. HEK-293-T Gal8-YFP cells and Gal8-YFP retrovirus concentrates are available upon request.

4.5.6 Data Processing and Statistical Methods

Plots and statistics were generated using Prism GraphPad 8.1.2. For the G8C2, G8G8, and Gal8-YFP systems, PPAA versus vehicle dose response curves were analyzed using ordinary two-way ANOVA with the following settings: no sample matching, column factor of PPAA versus vehicle, row factor of dose, with post-hoc testing to compare dose matched response of PPAA versus vehicle. Sidak's multiple comparison correction was used to calculate a multiplicity adjusted P value. The family-wise significance and confidence rate was set to 0.05, or a 95% confidence interval. Throughout the chapter, asterisks are used *per* the GraphPad Prism style: one asterisk for $p < 0.05$, two for $p < 0.01$, three for $p < 0.001$, and four for $p < 0.0001$.

4.6 References

(1) Adams, D.; Gonzalez-Duarte, A.; O'Riordan, W. D.; Yang, C.-C.; Ueda, M.; Kristen, A. V.; Tournev, I.; Schmidt, H. H.; Coelho, T.; Berk, J. L.; Lin, K.-P.; Vita, G.; Attarian, S.; Planté-Bordeneuve, V.; Mezei, M. M.; Campistol, J. M.; Buades, J.; Brannagan, T. H.; Kim, B. J.; et al. Patisiran, an RNAi Therapeutic, for Hereditary Transthyretin Amyloidosis. *N. Engl. J. Med.* **2018**, *379* (1), 11–21.

(2) Jayaraman, M.; Ansell, S. M.; Mui, B. L.; Tam, Y. K.; Chen, J.; Du, X.; Butler, D.; Eltepu, L.; Matsuda, S.; Narayanannair, J. K.; Rajeev, K. G.; Hafez, I. M.; Akinc, A.; Maier, M. A.; Tracy, M. A.; Cullis, P. R.; Madden, T. D.; Manoharan, M.; Hope, M. J. Maximizing the Potency of SiRNA Lipid Nanoparticles for Hepatic Gene Silencing In Vivo. *Angew. Chemie Int. Ed.* **2012**, *51* (34), 8529–8533.

(3) Thurston, T. L. M.; Wandel, M. P.; Von Muhlinen, N.; Foeglein, Á.; Randow, F. Galectin 8 Targets Damaged Vesicles for Autophagy to Defend Cells against Bacterial Invasion. *Nature* **2012**, *482* (7385), 414–418.

(4) Wittrup, A.; Ai, A.; Liu, X.; Hamar, P.; Trifonova, R.; Charisse, K.; Manoharan, M.; Kirchhausen, T.; Lieberman, J. Visualizing Lipid-Formulated SiRNA Release from Endosomes and Target Gene Knockdown. *Nat. Biotechnol.* **2015**, *33* (8), 870–876.

(5) Kilchrist, K. V.; Dimobi, S. C.; Jackson, M. A.; Evans, B. C.; Werfel, T. A.; Dailing, E. A.; Bedingfield, S. K.; Kelly, I. B.; Duvall, C. L. Gal8 Visualization of Endosome Disruption Predicts Carrier-Mediated Biologic Drug Intracellular Bioavailability. *ACS Nano* **2019**, acsnano.8b05482.

(6) Vasta, G. R. Galectins as Pattern Recognition Receptors: Structure, Function, and Evolution. *Adv. Exp. Med. Biol.* **2012**, *946*, 21–36.

(7) Kilchrist, K. V.; Evans, B. C.; Brophy, C. M.; Duvall, C. L. Mechanism of Enhanced Cellular Uptake and Cytosolic Retention of MK2 Inhibitory Peptide Nano-Polyplexes. *Cell. Mol. Bioeng.* **2016**, *9* (3), 368–381.

(8) Ideo, H.; Seko, A.; Ishizuka, I.; Yamashita, K. The N-Terminal Carbohydrate Recognition Domain of Galectin-8 Recognizes Specific Glycosphingolipids with High Affinity. *Glycobiology* **2003**, *13* (10), 713–723.

(9) Kim, B. W.; Beom Hong, S.; Hoe Kim, J.; Hoon Kwon, D.; Song, H. K. Structural Basis for Recognition of Autophagic Receptor NDP52 by the Sugar Receptor Galectin-8. *Nat. Commun.* **2013**, *4*, 1613.

(10) Cabantous, S.; Terwilliger, T. C.; Waldo, G. S. Protein Tagging and Detection with Engineered Self-Assembling Fragments of Green Fluorescent Protein. *Nat. Biotechnol.* **2005**.

(11) Shi, J.; Chou, B.; Choi, J. L.; Ta, A. L.; Pun, S. H. Investigation of Polyethylenimine/DNA Polyplex Transfection to Cultured Cells Using Radiolabeling and Subcellular Fractionation Methods. *Mol. Pharm.* **2013**, *10* (6), 2145–2156.

(12) Cranfill, P. J.; Sell, B. R.; Baird, M. A.; Allen, J. R.; Lavagnino, Z.; de Gruiter, H. M.; Kremers, G.-J.; Davidson, M. W.; Ustione, A.; Piston, D. W. Quantitative Assessment of Fluorescent Proteins. *Nat. Methods* **2016**, *13* (7), 557–562.

(13) Paulmurugan, R.; Gambhir, S. S. Combinatorial Library Screening for Developing an Improved Split-Firefly Luciferase Fragment-Assisted Complementation System for Studying Protein-Protein Interactions. *Anal. Chem.* **2007**, *79* (6), 2346–2353.

(14) Evans, B. C.; Hocking, K. M.; Osgood, M. J.; Voskresensky, I.; Dmowska, J.; Kilchrist, K. V.; Brophy, C. M.; Duvall, C. L. MK2 Inhibitory Peptide Delivered in Nanopolyplexes

Prevents Vascular Graft Intimal Hyperplasia. *Sci. Transl. Med.* **2015**, *7* (291), 291ra95.

(15) Evans, B. C.; Hocking, K. M.; Kilchrist, K. V.; Wise, E. S.; Brophy, C. M.; Duvall, C. L. Endosomolytic Nano-Polyplex Platform Technology for Cytosolic Peptide Delivery To Inhibit Pathological Vasoconstriction. *ACS Nano* **2015**, *9* (6), 5893–5907.

(16) Mukalel, A. J.; Evans, B. C.; Kilchrist, K. V.; Dailing, E. A.; Burdette, B.; Cheung-Flynn, J.; Brophy, C. M.; Duvall, C. L. Excipients for the Lyoprotection of MAPKAP Kinase 2 Inhibitory Peptide Nano-Polyplexes. *Journal of Controlled Release*. 2018.

CHAPTER 5

SUMMARY, IMPACTS, AND OUTLOOK

5.1 Chapter Summaries and Impact

Chapter one introduces the goals of this dissertation and provides a brief introduction to drug development as a process and discusses several modalities of large molecules. Because of the paucity of intracellular acting drugs, we give a brief review of all medicines in this class which the US FDA has approved as of the date of this dissertation. I then provide an overview of both families of polymers used in this dissertation.

Chapter 2 describes work to study more carefully a particularly exciting drug carrier invented by our group—MK2i-NP, which is formed by the simple mixing of a polymer poly(propylacrylic acid) and a MAPKAP kinase 2 inhibitory peptide. This drug / carrier system had been previously shown to have strong efficacy in preventing intimal hyperplasia in a preclinical rabbit model, which motivated a careful elucidation of the specific cellular mechanisms this system exploits. We uncovered an interesting mechanism of rapid, non-specific, hydrophobically-mediated binding due to PPAA that was not dependent on any of several types of specific receptors and that triggered macropinocytosis, as revealed by inhibitor studies and scanning electron microscopy. Further, we documented the cellular entry and endosomal disruption of this nanoparticle system using transmission electron microscopy and show that cellular entry and endosomal disruption were underway at 30 minutes post treatment. Finally, we showed a new assay based on Galectin 8 YFP which enabled us to characterize the kinetics of endosomal

Chapter 3 describes our efforts in developing the Gal8-YFP system for use as a high

throughput screening assay to assess families of drug carrier systems. We found that Gal8-YFP has uniquely high correlation to bioactivity assays, which correlates more strongly than other commonly used assays, including hemolysis, cellular uptake, and lysotracker colocalization. We further use this system to uncover novel insights into the effects of a well-studied drug delivery system based on PEG-50B, which uncovers that increasing molecular weight polymers have increased endosomal disruption potential in a dose matched setting. Finally, we also provide measurements of *in vivo* endosomal disruption and show that an *in vivo* optimized formulation of siNP produces both detectable endosomal disruption and detectable gene knockdown.

Chapter 4 describes two entirely new assays to measure endosomal disruption more quickly than the assay validated in chapter 3. These assays are designed to measure the interaction between Gal8 and CALCOCO2 or Gal8-NCRD with another Gal8-NCRD. These assays exhibit statistically significant luminescent increases when compared to vehicle controls. Further, we compare these assays to the previous best-in-class assay, Gal8-YFP and show that the overall trends match nicely, although the luminescent systems have reduced response ratios compared to Gal8-YFP, which is an acceptable trade off given the drastically reduced time to measurement of only 1 minute, versus 0.75 – 2 hours for the Gal8-YFP assay, depending on assay conditions. Further, this work demonstrates interaction between Gal8 and CALCOCO2 following treatment with endosome disrupting polymers, which supports our hypothesis that the ultimate fate of endosome disrupting polymers is the autophagosome or similar structures.

5.2 Future and Ongoing Work

5.2.1 Impact and Further Work Related to Aim 1 on Peptide Drug Delivery and Mechanistic Endocytosis Studies

Since Chapter 2 was published in 2016,[1] I have contributed to additional research in the Duvall lab which broadly support the mechanism we propose in Chapter 2. The most directly related work, by lead author Dr. Brian Evans, details the use of PPAA as a generalizable delivery reagent for a broad class of cationic peptides, proteins, and nanoparticles, while upcoming work by Dr. Eric Dailing describes a series of polymers synthesized to investigate the structure-function relationships between cell membrane interaction and charge/hydrophobe density. To support these efforts, we have tested several assays to measure peptide drug delivery in a high throughput manner. One assay, alluded to in Chapter 4, is based on cells which stably encode GFP_{1-10}, while GFP_{11}, a 16 amino acid peptide, is used as a model drug cargo. In our hands, this system was frustrating as it required measurement of signal using tedious flow cytometry assays to assess peptide drug delivery and produced underwhelming responsivity. My latest efforts have focused on establishing and validating plasmids, cell lines, and assay conditions based on a split NanoLuc assay[2] that we designed to have a stably expressed large fragment ("LgBiT") in the cytosol, and a small 11 amino acid high affinity fragment ("HiBiT"). Upon successful delivery of HiBiT peptide to the cytosol, a high-affinity interaction yields LgBiT-HiBiT complex, which catalyzes the production of bright luminescence from the substrate. Work is ongoing to validate this system, although we have promising initial results.

We have also continued to characterize the phenotype switching effects of vascular smooth muscle cells under MK2i inhibition, with promising results, and will be completing rabbit studies this summer using optimized, lyophilized polyplexes we had developed with Alvin Mukalel as

lead author.[3]

5.2.2 Impact and Further Work Related to Aim 2 on Development of Gal8-YFP Assays

Our work to validate Gal8-YFP recruitment has been well received by the drug delivery community. We have shared our cells or plasmids with at least 7 different labs in the United States and Europe. At least one lab has established a related system based on Gal8-GFP, and we plan to deposit a Gal8-mCherry construct with AddGene this summer for groups whose biosafety certifications preclude work with γ-retroviruses. The Gal8-YFP assay has already been used to support two published papers[3,4] in addition to Chapters 2 and 3, and at least four additional manuscripts in review or revision.

5.2.3 Further Work Related to Aim 3 on Development of Split Luciferase Endosomal Disruption Assays

The response ratios we observed with the G8G8 and G8C2 systems produced statistically significant results, but failed to outperform Gal8-YFP based assays *in vitro*. However, the high cell density present in tumors presented unique challenges for Gal8-YFP tracking *in vivo*, whereas increased cell numbers will only improve signal quality in the case of our somewhat dim split luciferase systems.

As to the *in vitro* component of this project, we have already begun plasmid design and cell line generation for this iteration of this program, although the next phase has several significant risks not present in the first phase, including outstanding questions about the non-homogenous localization of each NLuc and CLuc component throughout the endolysosomal system, whether the original NLuc394/CLuc398 interaction affinity is appropriate, and overall system brightness.

One particularly exciting question we consider as we embark upon the next phase is whether there are ways to quantitatively assess endosomal escape to specific subpopulations of endosomes, the disruption of which are reported to have differential effects in inflammasome activation, with tantalizing evidence that early endosome disruption produces minimal activation of the inflammasome, but disruption of lysosomes induces it strongly.[5–7]

5.3 Research Contributions

5.3.1 First Author Publications

1. **Kilchrist KV**, Dimobi SC, Jackson MA, Evans BC, Werfel TA, Dailing EA, Bedingfield SK, Kelly IB, Duvall CL. "Gal8 Tracking Enables Visualization of Carrier-mediated Endosome Disruption and Prediction of Biologic Cargo Intracellular Bioavailability." ACS Nano 2019. doi: 10.1021/acsnano.8b05482
2. **Kilchrist KV**, Evans BC, Brophy CM, Duvall CL. "Mechanism of Enhanced Cellular Uptake and Cytosolic Retention of MK2 Inhibitory Peptide Nano-polyplexes." Cellular and Molecular Bioengineering 2016. doi: 10.1007/s12195-016-0446-7

5.3.2 Co-authored Publications

3. Garland KM, Sevimli S, **Kilchrist KV**, Duvall CL, Cook RS, Wilson JT. "Microparticle Depots for Controlled and Sustained Release of Endosomolytic Nanoparticles." Cellular and Molecular Bioengineering 2019. doi: 10.1007/s12195-019-00571-6
4. Mignemi NA, McClatchey PM, **Kilchrist KV**, Williams IM, Millis B, Syring KE, Duvall CL, Wasserman DH, McGuinness OP. "Rapid changes in the microvascular circulation

of skeletal muscle impair insulin delivery during sepsis." AJP-Endocrinology and Metabolism 2019. doi: 10.1152/ajpendo.00501.2018

5. Mukalel AJ, Evans BC, **Kilchrist KV**, Dailing EA, Burdette B, Cheung-Flynn J, Brophy CM, Duvall CL. "Excipients for the lyoprotection of MAPKAP kinase 2 inhibitory peptide nano-polyplexes." J Control Release. 2018. doi: 10.1016/j.jconrel.2018.04.045
6. Werfel TA, Wang S, Jackson MA, Kavanaugh TE, Joly MM, Lee L, Hicks DJ, Sanchez V, Gonzalez-Ericsson PI, **Kilchrist KV**, Dimobi SC, Sarett SM, Brantley-Sieders D, Cook RS, Duvall CL. "Selective mTORC2 inhibitor therapeutically blocks breast cancer cell growth and survival." Cancer Res. 2018. doi: 10.1158/0008-5472.CAN-17-2388.
7. Sarett SM, Werfel TA, Lee L, Jackson MA, **Kilchrist KV**, Brantley-Sieders D, Duvall CL. "Lipophilic siRNA targets albumin in situ and promotes bioavailability, tumor penetration, and carrier-free gene silencing." Proc Natl Acad Sci U S A. 2017;114(32):E6490-E6497. doi: 10.1073/pnas.1621240114.
8. Jackson MA, Werfel TA, Curvino EJ, Yu F, Kavanaugh TE, Sarett SM, Dockery MD, **Kilchrist KV**, Jackson AN, Giorgio TD, Duvall CL. "Zwitterionic Nanocarrier Surface Chemistry Improves siRNA Tumor Delivery and Silencing Activity Relative to Polyethylene Glycol." ACS Nano. 2017 doi: 10.1021/acsnano.7b01110.
9. Beavers KR, Werfel TA, Shen T, Kavanaugh TE, **Kilchrist KV**, Mares JW, Fain JS, Wiese CB, Vickers KC, Weiss SM, Duvall CL. "Porous Silicon and Polymer Nanocomposites for Delivery of Peptide Nucleic Acids as Anti-MicroRNA Therapies." Adv Mater. 2016. doi: 10.1002/adma.201601646.
10. Werfel TA, Swain C, Nelson CE, **Kilchrist KV**, Evans BC, Miteva M, Duvall CL. "Hydrolytic charge-reversal of PEGylated polyplexes enhances intracellular un-

packaging and activity of siRNA." J Biomed Mater Res A. 2016. doi: 10.1002/jbm.a.35629.

11. Evans BC, Hocking KM, **Kilchrist KV**, Wise ES, Brophy CM, Duvall CL. "Endosomolytic Nano-Polyplex Platform Technology for Cytosolic Peptide Delivery To Inhibit Pathological Vasoconstriction." ACS Nano. 2015 doi: 10.1021/acsnano.5b00491.
12. Evans BC, Hocking KM, Osgood MJ, Voskrensky I, Dmowska J, **Kilchrist KV**, Brophy CM, Duvall CL. "Nano-polyplex MK2 Inhibitory Peptide Delivery Inhibits Vascular Graft Intimal Hyperplasia." Science Translational Medicine. 2015. doi: 10.1126/scitranslmed.aaa4549
13. Sarett SM, **Kilchrist KV**, Miteva M, Duvall CL. "Conjugation of Palmitic Acid Improves Potency and Longevity of siRNA Delivered via Endosomolytic Polymer Nanoparticles." J Biomed Mater Res A. 2015. doi: 10.1002/jbm.a.35413.
14. Miteva M, Kirkbride KC, **Kilchrist KV**, Werfel TA, Li H, Nelson CE, Gupta MK, Giorgio TD, Duvall CL. "Tuning PEGylation of mixed micelles to overcome intracellular and systemic siRNA delivery barriers." Biomaterials. 2015 doi: 10.1016/j.biomaterials.2014.10.036

5.4 References

(1) Kilchrist, K. V.; Evans, B. C.; Brophy, C. M.; Duvall, C. L. Mechanism of Enhanced Cellular Uptake and Cytosolic Retention of MK2 Inhibitory Peptide Nano-Polyplexes. *Cell. Mol. Bioeng.* **2016**, *9* (3), 368–381.

(2) Dixon, A. S.; Schwinn, M. K.; Hall, M. P.; Zimmerman, K.; Otto, P.; Lubben, T. H.; Butler, B. L.; Binkowski, B. F.; Machleidt, T.; Kirkland, T. A.; Wood, M. G.; Eggers, C. T.; Encell, L. P.; Wood, K. V. NanoLuc Complementation Reporter Optimized for Accurate Measurement of Protein Interactions in Cells. *ACS Chem. Biol.* **2016**, *11* (2), 400–408.

(3) Mukalel, A. J.; Evans, B. C.; Kilchrist, K. V.; Dailing, E. A.; Burdette, B.; Cheung-Flynn, J.; Brophy, C. M.; Duvall, C. L. Excipients for the Lyoprotection of MAPKAP Kinase 2 Inhibitory Peptide Nano-Polyplexes. *Journal of Controlled Release*. 2018.

(4) Werfel, T. A.; Wang, S.; Jackson, M. A.; Kavanaugh, T. E.; Joly, M. M.; Lee, L. H.; Hicks, D. J.; Sanchez, V.; Ericsson, P. G.; Kilchrist, K. V.; Dimobi, S. C.; Sarett, S. M.; Brantley-Sieders, D. M.; Cook, R. S.; Duvall, C. L. Selective MTORC2 Inhibitor Therapeutically Blocks Breast Cancer Cell Growth and Survival. *Cancer Res.* **2018**, *78* (7), 1845–1858.

(5) Baljon, J. J.; Dandy, A.; Wang-Bishop, L.; Wehbe, M.; Jacobson, M. E.; Wilson, J. T. The Efficiency of Cytosolic Drug Delivery Using PH-Responsive Endosomolytic Polymers Does Not Correlate with Activation of the NLRP3 Inflammasome. *Biomater. Sci.* **2019**.

(6) Katsnelson, M. A.; Lozada-Soto, K. M.; Russo, H. M.; Miller, B. A.; Dubyak, G. R. NLRP3 Inflammasome Signaling Is Activated by Low-Level Lysosome Disruption but Inhibited by Extensive Lysosome Disruption: Roles for K + Efflux and Ca 2+ Influx . *Am. J. Physiol. Physiol.* **2016**.

(7) Davis, M. J.; Swanson, J. A. Technical Advance: Caspase-1 Activation and IL-1β Release Correlate with the Degree of Lysosome Damage, as Illustrated by a Novel Imaging Method to Quantify Phagolysosome Damage. *J. Leukoc. Biol.* **2010**.